

AD-A075 833

TEXAS UNIV AT AUSTIN APPLIED RESEARCH LABS
LABORATORY AND FIELD STUDIES OF SEDIMENT ACOUSTICS.(U)

F/G 20/1

UNCLASSIFIED

ARL-TR-79-26

N00014-76-C-0117

NL

1 OF 2

AD
A075833



ARL-TR-79-26

Copy No. 58

LABORATORY AND FIELD STUDIES OF SEDIMENT ACOUSTICS

Annual Report under Contract N00014-76-C-0117

Donald J. Shirley
David W. Bell
Jens M. Hovem

LEVEL

APPLIED RESEARCH LABORATORIES
THE UNIVERSITY OF TEXAS AT AUSTIN
POST OFFICE BOX 8029, AUSTIN, TEXAS 78712

12 June 1979

Annual Report

1 January - 31 December 1978

APPROVED FOR PUBLIC RELEASE;
DISTRIBUTION UNLIMITED

Prepared for:

OFFICE OF NAVAL RESEARCH
DEPARTMENT OF THE NAVY
ARLINGTON, VA 22217

DDC
RECEIVED
OCT 26 1979
E

AD A075833

DDC FILE COPY



79 10 26 01

UNCLASSIFIED

SECURITY CLASSIFICATION OF THIS PAGE (When Data Entered)

REPORT DOCUMENTATION PAGE		READ INSTRUCTIONS BEFORE COMPLETING FORM
1. REPORT NUMBER	2. GOVT ACCESSION NO.	3. RECIPIENT'S CATALOG NUMBER
4. TITLE (and Subtitle)		5. TYPE OF REPORT & PERIOD COVERED
LABORATORY AND FIELD STUDIES OF SEDIMENT ACOUSTICS		annual report 1 January - 31 December '78
7. AUTHOR(s)		6. PERFORMING ORG. REPORT NUMBER
Donald J. Shirley, David W. Bell, and Jens M. Hovem		ARL-TR-79-26
9. PERFORMING ORGANIZATION NAME AND ADDRESS		8. CONTRACT OR GRANT NUMBER(s)
Applied Research Laboratories The University of Texas at Austin Post Office Box 8029, Austin, Texas 78712		N00014-76-C-0117
11. CONTROLLING OFFICE NAME AND ADDRESS		10. PROGRAM ELEMENT, PROJECT, TASK AREA & WORK UNIT NUMBERS
Office of Naval Research Department of the Navy Arlington, VA 22217		921371
14. MONITORING AGENCY NAME & ADDRESS (if different from Controlling Office)		12. REPORT DATE
		12 June 1979
		13. NUMBER OF PAGES
		141
		15. SECURITY CLASS. (of this report)
		UNCLASSIFIED
		15a. DECLASSIFICATION DOWNGRADING SCHEDULE
		N/A
16. DISTRIBUTION STATEMENT (of this Report)		
Approved for public release; distribution unlimited.		
17. DISTRIBUTION STATEMENT (of the abstract entered in Block 20, if different from Report)		
18. SUPPLEMENTARY NOTES		
19. KEY WORDS (Continue on reverse side if necessary and identify by block number)		
in situ compressional wave acoustics nonlinear sediments shear wave		
20. ABSTRACT (Continue on reverse side if necessary and identify by block number)		
(U) During the period 1 January - 31 December 1978, work under Contract N00014-76-C-0017 consisted of three parts: (1) redesign and updating of the ARL:UT profilometer system used to measure in situ sound velocities of ocean bottom sediments, (2) development of transducers to measure shear wave and acoustic impedance parameters of sediments, and (3) laboratory measurements to develop and confirm theoretical models for acoustic propagation in sediments. Data obtained for the three parts of the program are reported.		

DD FORM 1 JAN 73 1473

EDITION OF 1 NOV 65 IS OBSOLETE

UNCLASSIFIED

SECURITY CLASSIFICATION OF THIS PAGE (When Data Entered)

404 434

JOB

TABLE OF CONTENTS

	<u>Page</u>
LIST OF TABLES	v
LIST OF FIGURES	vii
I. INTRODUCTION	1
II. FIELD MEASUREMENTS	5
A. Revised Profilometer Design	6
B. Shear Wave Transducer Design	7
C. Acoustic Impedance Measurements	10
III. ACCELEROMETER SHEAR STRENGTH MEASUREMENTS	19
IV. LABORATORY MEASUREMENTS	29
A. Introduction	29
B. Sediment Physical Properties	30
C. Sediment Acoustic Properties	36
1. Experimental Procedure	36
2. Data Reduction	44
3. Wave Velocities	44
4. Attenuation	44
D. Empirical Relationships	58
E. Theoretical Considerations	62
F. Conclusions	74
V. DETERMINATION OF THE NONLINEARITY PARAMETER OF SATURATED SEDIMENTS BY IMPEDANCE MEASUREMENT	77
REFERENCES	85
APPENDIX A BIBLIOGRAPHY, ONR CODE 480 PROGRAM DOCUMENTATION	89
APPENDIX B DESCRIPTION OF NEW DESIGN FOR RECORDER	95
APPENDIX C EXPLANATION OF FUNCTION OF PROFILOMETER CIRCUITS	101
APPENDIX D CALIBRATION AND SETUP OF PROFILOMETER	129

Accession For NTIS GRA&I DEC TAB Unannounced Justification	By	Distribution/ Availability Codes	Avail and/or special
			Dist. <i>A</i>

LIST OF TABLES

<u>Table</u>	<u>Title</u>	<u>Page</u>
I	Parameter Values for Transducers	14
II	Sediment Physical Properties	32
III	Sediment Acoustic Properties	45

LIST OF FIGURES

<u>Figure</u>	<u>Title</u>	<u>Page</u>
1	Schematic Drawing of Composite Profilometer Transducer	8
2	Schematic Drawing of Modified Composite Profilometer Transducer	9
3	Cross Section of Acoustic Impedance Transducer	12
4	Admittance Diagram for Acoustic Loads of Air, Water, and Sand	15
5	Transducer Electrical Impedance as a Function of Acoustic Impedance of the Medium	16
6	Acceleration Plot for Core 3	21
7	Velocity Plot for Core 3	22
8	Plot of Bottom Penetration for Core 3	23
9	Plot of Hydrodynamic Drag Coefficient as a Function of Corer Velocity	24
10	Shear Strength for Three Cores Plotted As a Function of Depth	26
11	Sediment Grain Size Distributions	31
12	Constant Head Permeameter	34
13	Determination of Sediment Permeability	35
14	Determination of Kozeny-Carman Constant Relating Permeability to Grain Size	37
15	Transducer Mounts	39
16	Shear Wave Signal Quality--Ottawa Sand	40
17	Multicycle Shear Wave Pulse	43
18	Determination of Compressional Wave Velocity in Saturated Sediments	46
19	Determination of Shear Wave Velocity in Saturated Sediments	47
20	Determination of Shear Wave Velocity in Dry Sediments	48
21	Determination of Compressional Wave Attenuation	49
22	Determination of Shear Wave Attenuation Factor-- $k = \Delta a / \Delta f$	51
23	Shear Wave Attenuation versus Frequency, Dry PC Sand	53

LIST OF FIGURES (Cont'd)

<u>Figure</u>	<u>Title</u>	<u>Page</u>
24	Shear Wave Attenuation versus Frequency, Saturated PC Sand	55
25	Shear Wave Attenuation versus Frequency, Dry MH Beads	56
26	Shear Wave Attenuation versus Frequency, Saturated MH Beads	57
27	Variation of Compressional Wave Attenuation with Grain Size and Porosity	60
28	Relative Contributions of Theoretical Frame Loss and Viscous Dissipation to Shear Wave Attenuation	68
29	Shear Wave Attenuation Compared with Predicted Viscous Loss - MH Beads	72
30	Shear Wave Attenuation Compared with Predicted Viscous Loss - PC Sand	73
31	Relative Amplitude of the Second Harmonic Signal as a Function of Transmitted Intensity	79
32	Transducer Arrangement for Nonlinear Impedance Measurement	81
33	Amplitude of the Nonlinearly Generated 2nd Harmonic Component as a Function of the Distance from the Transducer	82
34	Profilometer Tape Transport	98
35	Profilometer System Block Diagram	104
36	Pulse Generator Schematic	107
37	Input Preamplifier Schematic	109
38	Filter Schematic	110
39	Phase Shifter Schematic	112
40	Pulse Amplitude Detector Schematic	113
41	Time Delay Detector Schematic	115
42	Time Delay-To-Voltage Converter Schematic	117
43	Accelerometer Schematic	120
44	FM Record Schematic	122
45	Recorder Control Schematic	124
46	Power Supply Schematic	126
47	Profilometer Layout	132
48	Profilometer Timing Diagram	134

I. INTRODUCTION

If the compressional wave velocity (c_p) and the shear wave velocity (c_s) of a marine sediment can be measured concurrently with a measurement of either bulk density (ρ) or acoustic impedance (ρc), the elastic parameters of the sediment can be completely characterized. Acoustic measurements are made on sediment samples that have been removed from the bottom and brought to the surface through the process of geophysical coring (using a gravity corer, a piston corer, or a box corer). Sample disturbance and temperature and pressure changes tend to degrade the reliability of such measurements.

Early attempts at in situ measurements of acoustic properties used special devices to be either lowered from the surface or planted by submersible. Although the data quality improved, the complications of specialized equipment cost more and reduced the number of measurements which could be made.

With the above considerations, the best acoustic measuring program for ocean bottom sediments seemed to be one which would obtain data in situ to minimize as much as possible the adverse effects of sample disturbance and temperature and pressure changes and which would obtain data by the addition of equipment to some routine operation such as geophysical coring.

For the past several years Applied Research Laboratories, The University of Texas at Austin (ARL:UT), has had a program funded by Office of Naval Research (ONR) for developing the capability of measuring compressional wave, shear wave, and acoustic impedance of marine sediments in situ. Laboratory measurements of acoustic parameters and physical properties to augment and support the in situ measurements have developed from the program.

Considerations of data reliability and cost have been the primary impetus for the development of the ARL:UT profilometer system. The system at present is designed to measure compressional wave velocity in situ. The measurement is made by attaching the self-contained instrumentation to existing coring equipment. Recording and measuring circuits are contained in a cylindrical aluminum pressure case attached to the top weighted end of the corer. Transducers are attached to the cutter at the bottom of the core barrel and are connected to the pressure case by electrical cables on the outside of the core barrel. The unit is operated during normal coring operations, and adds little time or effort to the procedure.

The profilometer system has developed in stages up to the present time and certain aspects are still under development. In 1971, the feasibility of such measurements was demonstrated using laboratory equipment and a small mud tank.¹ Once feasibility was demonstrated, equipment was built to allow field measurements on a piston corer and on a hand corer in shallow water using cables to the surface.² In 1974 the profilometer was redesigned so that the recording system was contained in a pressure case to eliminate the problems associated with the cables to the surface.³ With the success of the compressional wave measurements, it was decided in 1975 to investigate the possibility of adding shear wave and acoustic impedance measurements to the system.⁴ Since that time, design of transducers has progressed to the point that field tests have been made.⁵ During development of the in situ measurement capability, an extensive program of acoustic laboratory measurements in real as well as artificial sediments was also in progress using the new transducers developed for in situ work.⁶ Developmental work on the measurement of acoustic impedance has produced a transducer design suitable for integration into the profilometer system for in situ measurement of this parameter.⁷

The work during 1978 was divided into three major parts, which are described in this report:

- (1) Use of the profilometer equipment in the field to make compressional wave measurements in situ and to test shear wave transducer design. A small part of the task was also directed at examining a method for calculating sediment shear strength from in situ deceleration profiles for the corer.
- (2) Continued design and development of in situ shear wave and acoustic impedance transducers to maximize sensitivity and ruggedness.
- (3) Theoretical and experimental laboratory work to develop models for acoustic propagation in sediments.

During a field trip, the profilometer recording unit was lost, thus requiring the construction of a new unit. The necessary reconstruction allowed modification of the profilometer design to incorporate newer electronic devices and to expand functional capabilities. Appendixes B and C describe the new recorder and electronic designs, respectively. Setup and calibration of the new profilometer recorder are covered in Appendix D.

A bibliography of publications under the sediment acoustic program is included as Appendix A. During the past several years, eleven technical reports have been published, eleven papers have been presented at meetings, four papers have been published in journals, three papers have been included in books, and two invention disclosures have been submitted for patents. Of these, one publication, one letter to the editor, and one technical report were issued during 1978.^{5,6,8}

II. FIELD MEASUREMENTS

Field tests were conducted aboard ship in the deep ocean environment to record compressional wave data and to evaluate designs for transducers and circuits to make shear wave measurements in situ.

During the period 2 June - 22 June 1978, ARL:UT personnel together with University of Rhode Island personnel made a field trip aboard R/V ENDEAVOR to the Atlantic Ocean near 36°N, 62°W. The purpose of this trip was to record in situ compressional wave velocity profiles by using the profilometer attached to a modified large piston corer (LPC). Newly designed shear wave transducers were also to be tested during this trip.

The first sampling was made without the profilometer attached to the corer so that operation and timing of the coring system could be observed. For the second test the profilometer, including the new shear wave transducers, was attached. During retrieval of the second corer, the coring cable parted, causing the loss of both the corer and profilometer. As a result, no data were obtained and the new shear wave transducer design remained untested.

As a result of this loss of the only remaining profilometer recorder, two new recording units were built (for use in 1979). The system was redesigned to incorporate improved electronic circuitry to reduce power consumption and to extend the capability of the profilometer to concurrently measure compressional wave, shear wave, and acoustic impedance parameters.

It was decided to reduce power consumption rather than increase battery size to handle the expanded measurement capability since the latter would necessitate an increase in the size of the pressure case. By redesigning the electronics to incorporate BIFET linear circuit

technology and by replacing the TTL logic with CMOS logic, the power consumption of the profilometer configured to measure compressional wave parameters only was reduced from 0.7 A to 0.15 A at 12 V. Thus a threefold increase in the circuit capacity of the profilometer will leave the power drain at the same level as in the previous design.

Another advantage of combining CMOS digital and BIFET linear circuits is that both can operate from the same single supply voltage, thereby reducing the complexity of the power supply and control circuitry.

Design details of the tape recorder are given in Appendix B. Operation and design of the new profilometer circuits are explained in detail in this appendix, while operation, setup, and calibration of the system are explained in Appendix D.

A. Revised Profilometer Design

The new profilometer design incorporates space for additional circuits to measure shear wave and acoustic impedance parameters. Space has been left in the printed circuit card cage for the addition of these additional circuit cards when appropriate transducers are built. An important consequence of the additional circuitry is the almost three-fold increase in power drain from the battery supply. Also, since additional data will be recorded, an increase in bandwidth of the tape recording system is needed. The two requirements of the increased power and bandwidth have resulted in the following changes in the profilometer circuitry.

- (1) Design of a different recording system incorporating a digital cartridge type tape recorder operating at 7 ips, 4-channel FM.
- (2) Redesign of all electronic circuits to reduce power consumption by the use of CMOS digital components and MOS-FET analog components.
- (3) Elimination of the triple voltage switching supply since single supply operation is possible with the MOS-FET digital and analog circuits.

- (4) As in the old design, the electronic circuits are switched on at the surface during deployment of the corer. The tape recorder, however, is switched on only when the corer is triggered, thus allowing a smaller length of tape to be used.

The size of the pressure case has not been changed. Its external size is 15.9 cm diam by 71.1 cm long and it weighs 29.5 kg in air. The case is constructed of anodized aluminum with screw-on end caps. Pressure capability of the case is 703 kg/cm^2 (10,000 psi).

B. Shear Wave Transducer Design

A design for an in situ shear wave transducer was described in an earlier report.⁵ In this design, an array of five bender elements was formed with a small compressional wave element bonded to the front of the shear wave array. Transducer units constructed using this design were lost during the tests on R/V ENDEAVOR. A new set of shear wave transducers has been built with essentially the same design as before but with some modification to improve their durability. Figure 1 shows the original design while Fig. 2 shows the modified design. The major difference between the two designs is that the shear wave bender elements have been shortened to enable the pressure compensating chamber to be placed at the back of the housing to make a more monolithic structure less subject to abuse. The shortened length of the benders has the effect of raising the resonance frequency of the system but does not affect its sensitivity appreciably.

An absolute measurement of frequency response and sensitivity for shear wave transducers is difficult because there are no media available which have shear wave parameters that are constant with frequency. Comparisons can be made between two types of shear wave transducers that are propagating over the same path with equal drive voltages on each projector. Comparisons were made between transducers mounted in a corer cutter (path length 7 cm) with water saturated beach sand as the medium. A 10 V pulse was used to drive the projector. Pulse length

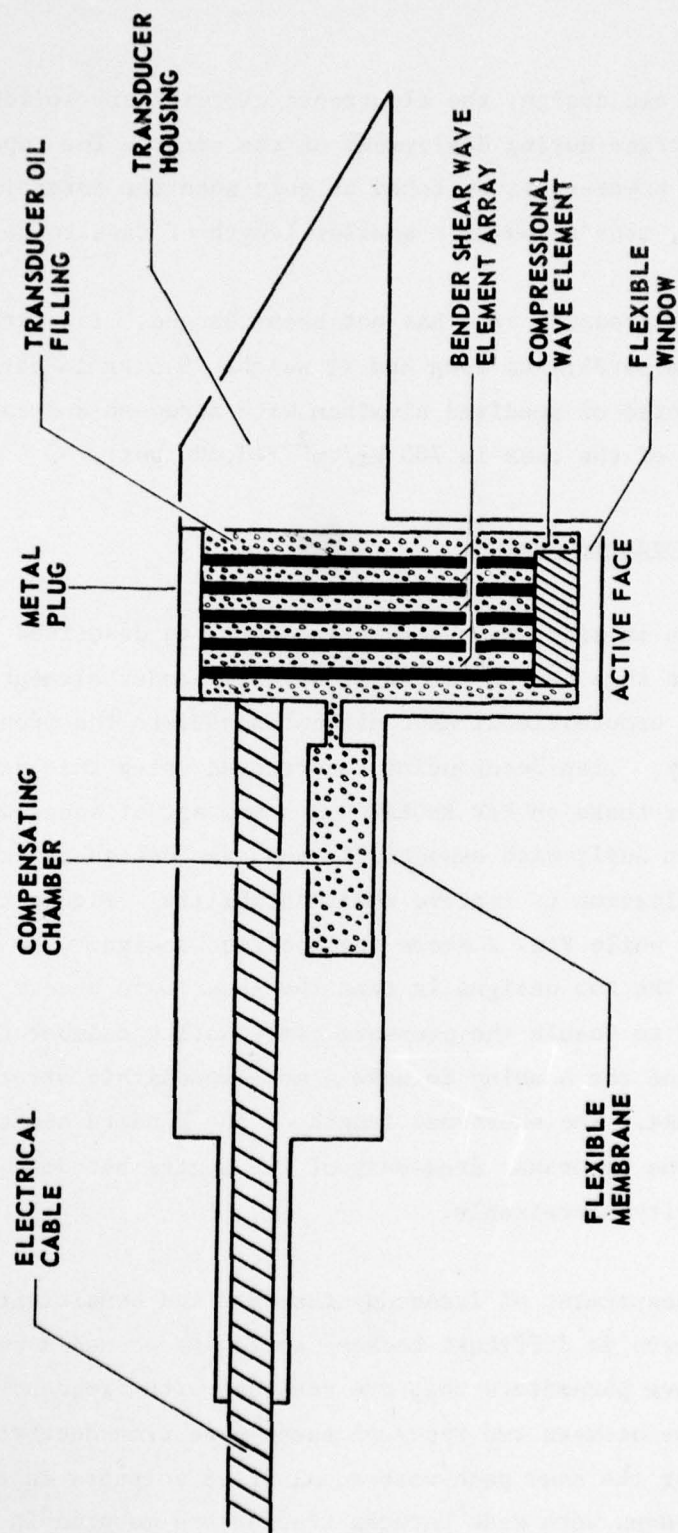


FIGURE 1
SCHEMATIC DRAWING OF COMPOSITE PROFILOMETER TRANSDUCER

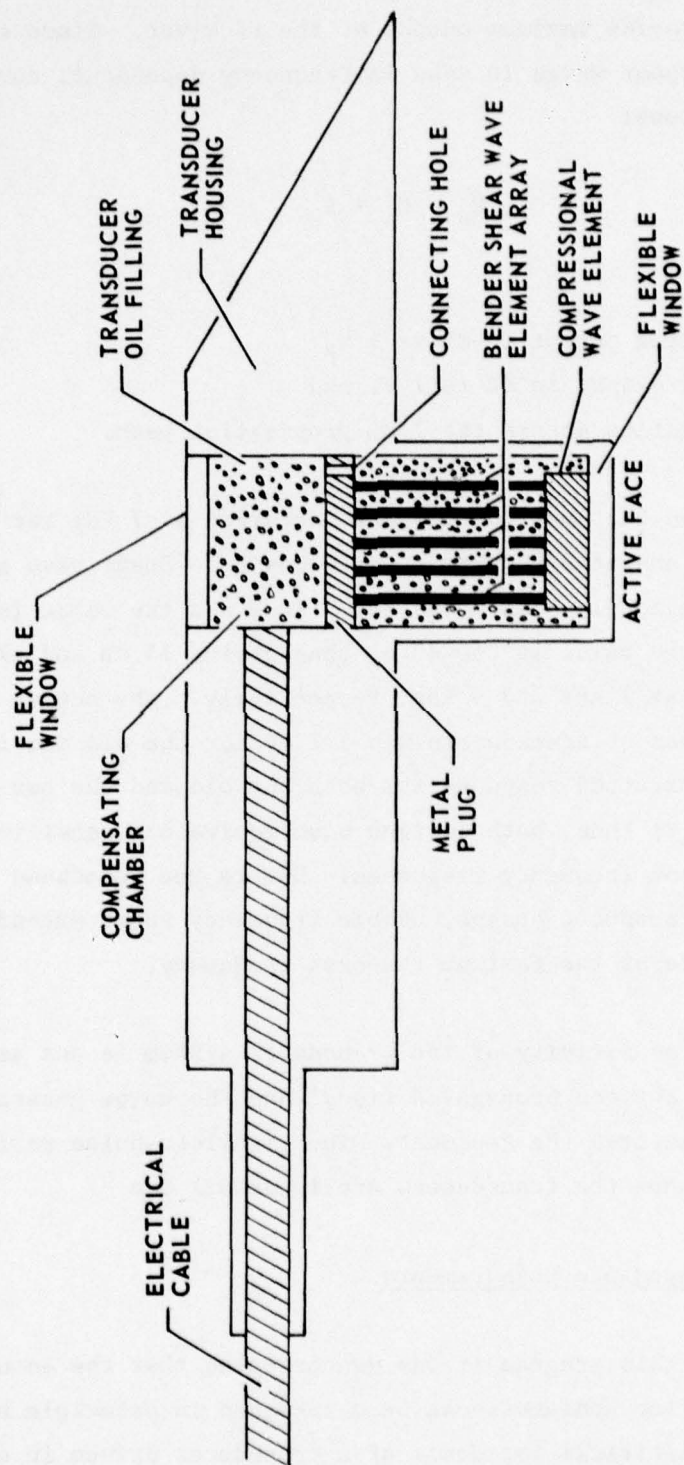


FIGURE 2
SCHEMATIC DRAWING OF MODIFIED COMPOSITE PROFILOMETER TRANSDUCER

was varied to provide maximum output at the receiver. Since the attenuation of shear waves in sand is frequency dependent, correction was made as follows:

$$E_c = E_A + A \quad , \quad (1)$$

where

E_c = corrected output in dB re 1 V,

E_A = actual output in dB re 1 V, and

A = attenuation across the 7 cm propagation path.

It was found that maximum response occurred at 7 kHz for the old type transducer and at 9 kHz for the new design. Shear wave attenuation for sand has previously been measured.⁵ At 7 kHz the value is 200 dB/m while at 9 kHz the value is 250 dB/m, thus giving 14 dB and 17.5 dB as values for A at 7 kHz and 9 kHz, respectively. The actual output from the two types of transducers was 2.2 mV for the old and 1.5 mV for the new. The corrected response for both the old and the new designs was -39 dB re 1 V; thus, both designs have equivalent sensitivities but slightly different frequency responses. Due to the broadband characteristic of this transducer design, usable frequency range extends about 5 kHz either side of the maximum response frequency.

The actual sensitivity of the transducer system is not as important as is the ratio between propagated signal and the noise generated by the corer as it penetrates the sediment. The signal-to-noise ratio can be evaluated only when the transducers are in actual use.

C. Acoustic Impedance Measurements

Earlier in this program it was demonstrated that the acoustic impedance of marine sediments can be determined in principle by measuring the electrical impedance of a transducer driven in contact with the sediment.⁷ Work during the past year has focused on developing new

transducers capable of stable operation at great depths with a minimum change in operating characteristics.

For best accuracy the transducer should give a relatively large change in electrical impedance for a given change in acoustic impedance. This requires a transducer with low electrical and mechanical losses. The mechanical losses which are the most significant are mainly caused by internal friction of the transducer and losses in the mounting. Unfortunately, it has been found that the piezoelectric ceramic materials with the lowest losses also show the greatest changes in piezoelectric parameter values with ambient pressure.

The new transducers are designed in such a way that the piezoelectric ceramic is kept at atmospheric pressure and is mounted such that the mechanical losses are minimized. The principal features of the new transducer are shown in Fig. 3. The transducer is an air backed, half-wavelength resonator composed of a quarter-wavelength piezoelectric disk and a quarter-wavelength steel radiating head. The whole resonator is mounted in a hole and supported by a flange on the steel head and is fixed by a threaded ring. The electronics are placed in a small compartment next to the transducer.

The dimensions of the transducer are determined from the following considerations: The diameter D must be large compared with the wavelength λ to ensure a real radiation impedance. The criterion used is $D > 3\lambda$. To give a sufficient resolution when mounted on a corer, the transducer diameter should be as small as possible. A diameter $D = 15$ mm was selected, thereby fixing the minimum operating frequency at 300 kHz.

The thickness of the piezoelectric disk and the radiating head is given by the selected operating frequency and the sound speeds. The thickness of the flange affects both the strength of the transducer and its efficiency. It is difficult to estimate how the transducer will be affected when the flange is clamped, and some experimenting will be

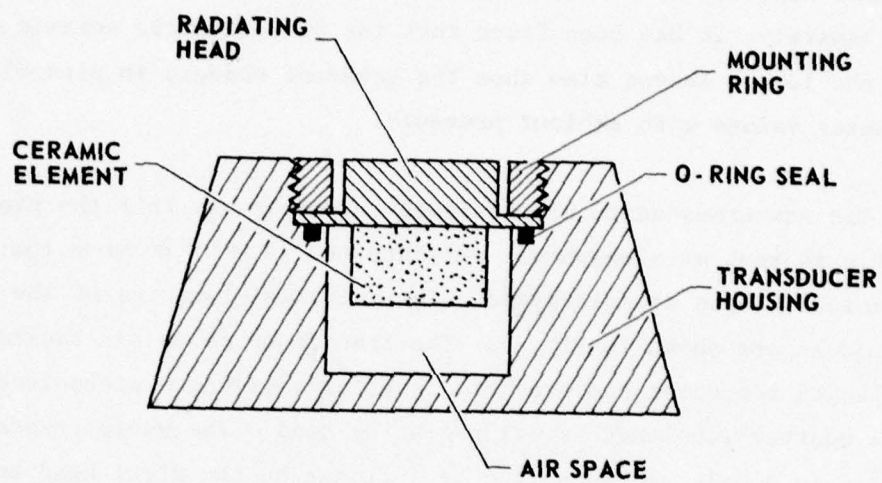


FIGURE 3
CROSS SECTION OF ACOUSTIC IMPEDANCE TRANSDUCER

necessary. However, the effect of the flange should be small so long as the ratio $t/T < 0.1-0.15$, which corresponds to a phase angle of $10^\circ-15^\circ$ across the flange. Here t is the thickness of the flange and T is the thickness of the transducer.

The shear stress along the diameter of the hole, D_h , is approximately

$$\sigma_s = \frac{\pi D_h^2}{4 \pi D_h t} w = \frac{D_h}{4t} w, \quad (2)$$

where w is the ambient pressure and is equal to $7 \times 10^7 \text{ N/m}^2$ for deep ocean depths (7000 m).

Table I gives the main parameter values for a transducer, A, which has been developed and tested as well as parameter values for alternative designs, B and C.

The material used in transducer A is 316 stainless steel with an estimated shear yield strength of $2.0 \times 10^9 \text{ N/m}^2$, which conservatively means that this transducer can be used down to about 2000 m depth. To obtain full ocean depth with transducer A and the other transducers, the head should be made of tool-steel with a shear strength of about $1.3 \times 10^{10} \text{ N/m}^2$.

Figure 4 shows admittance diagrams for the 450 kHz transducer radiating into air, water, and sand. The diagrams are reasonably close to circles; the small deviations are probably due to the excitation of other modes. The acoustic impedance, which is inversely proportional to the size of the circle, can be determined by measuring voltage and current at the resonance frequency.²

Figure 5 shows electrical impedance values calculated from admittance diagrams plotted as a function of the acoustic impedance of

TABLE I
PARAMETER VALUES FOR TRANSDUCERS

Transducer	Frequency (kHz)	Diameter D_h (m)	Head Thickness T (m)	Flange Thickness t (m)	Shear Stress at 7000 m (N/m^2)
A	450	1.9×10^{-2}	4.8×10^{-3}	1.3×10^{-3}	2.5×10^9
B	400	1.9×10^{-2}	5.6×10^{-3}	0.6×10^{-3}	5.3×10^9
C	300	1.9×10^{-2}	7.4×10^{-3}	0.75×10^{-3}	4.3×10^9

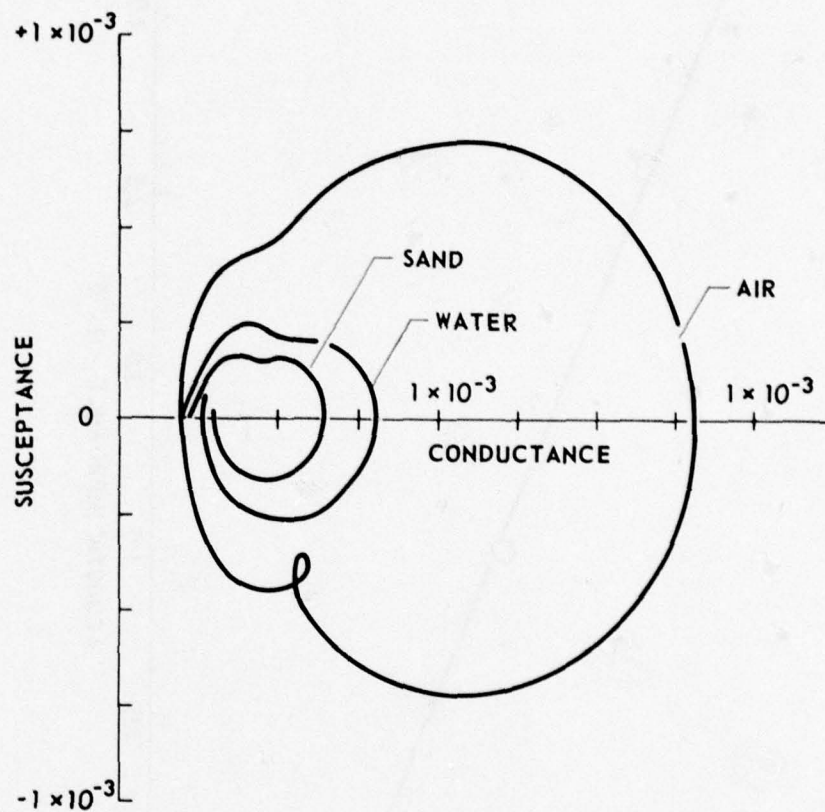


FIGURE 4
ADMITTANCE DIAGRAM FOR ACOUSTIC LOADS
OF AIR, WATER, AND SAND

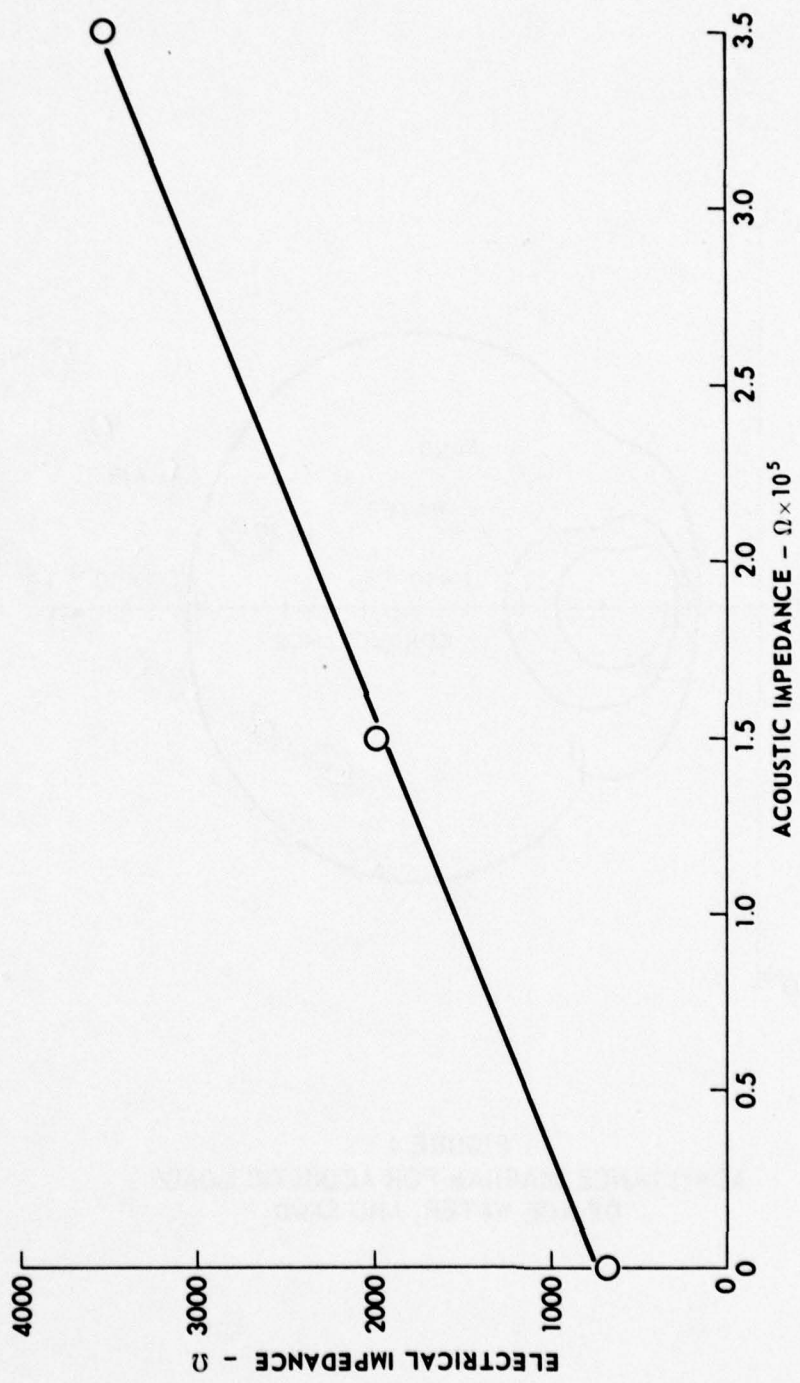


FIGURE 5
TRANSDUCER ELECTRICAL IMPEDANCE AS A FUNCTION
OF ACOUSTIC IMPEDANCE OF THE MEDIUM

ARL:UT
AS-79-942
DJS- GA
5-11-79

the medium measured by other means. The values reasonably fit a straight line.

This transducer is currently being tested in liquids with differing sound velocities and densities.

III. ACCELEROMETER SHEAR STRENGTH MEASUREMENTS

Shear strength is an important measure of the physical properties of an ocean sediment, although there is no one universally recognized method of making the measurement. For obvious reasons, an in situ measurement of shear strength is more desirable than one made in the laboratory on samples retrieved from the ocean bottom. Many methods have been proposed and used, including penetrometer attachments for corers,⁹ penetrometers and vane shear devices mounted on submersibles,¹⁰⁻¹³ vane shear devices mounted on bottom platforms,¹⁴ and accelerometers mounted on corers.¹⁵ This last method is the topic of this section since one of the data channels obtained in the use of the acoustic profilometer is a record of the acceleration during penetration of the corer into the ocean bottom. The acceleration history during penetration is used to develop a depth axis to plot the sound velocity profile, but there are indications that the data can also be used to obtain a measurement of the static shear strength of the sediment.

The equation of motion of a piston corer which is penetrating along the z axis into the ocean bottom is

$$M\ddot{z} = Mg - F - C(\dot{z})^2, \quad (3)$$

where

M = mass of corer,

g = acceleration due to gravity,

C = hydrodynamic drag coefficient, and

F = force due to the shearing of the sediment by the core barrel.

The hydrodynamic drag coefficient in the above equation is due to the drag of the water on the corer. This drag is proportional to the square of the velocity of the corer and, in the absence of penetration

into the bottom, would bring the corer to a terminal velocity where the acceleration on the corer due to gravity is just balanced by the force due to the drag. The drag coefficient can be determined empirically from the change in the acceleration profile before the corer enters the sediment.

Figure 6 shows a typical acceleration profile obtained when the profilometer equipment was used on a Ewing type piston corer. This profile was obtained on a drop near the coast of South America and is typical of many that were recorded in the same area on R/V VEMA during a field trip with the profilometer in June 1974. Penetration of the sediment occurred about 0.9 sec after the corer was tripped (indicated by the arrow). Figures 7 and 8 are the velocity and depth profiles calculated from the acceleration by a first and second integration, respectively. Integration constants are provided by the fact that final acceleration and velocity of the corer are both zero.

The period between tripping and initial penetration can be used to calculate the hydrodynamic drag coefficient of the corer by setting the second term in Eq. (3) to zero and using the acceleration and velocity values during this period to calculate the drag coefficient. Figure 9 shows a plot of drag coefficient for core 3 and for two other cores (core 7 and core 8) taken in the same general area. The coefficient will, in general, not be a constant except at the higher velocities. The difference between the plot for core 7 and that for cores 3 and 8 is due to a thermal measuring instrument package mounted on the corer for core 3 and core 8 but not for core 7.

Once the drag coefficient has been calculated, the resisting force F due to the shearing resistance of the sediment can be calculated from Eq. (3). In general, F is a function of the shear strength S of the sediment and the depth of penetration, i.e.,

$$F = S\pi Dz \quad , \quad (4)$$

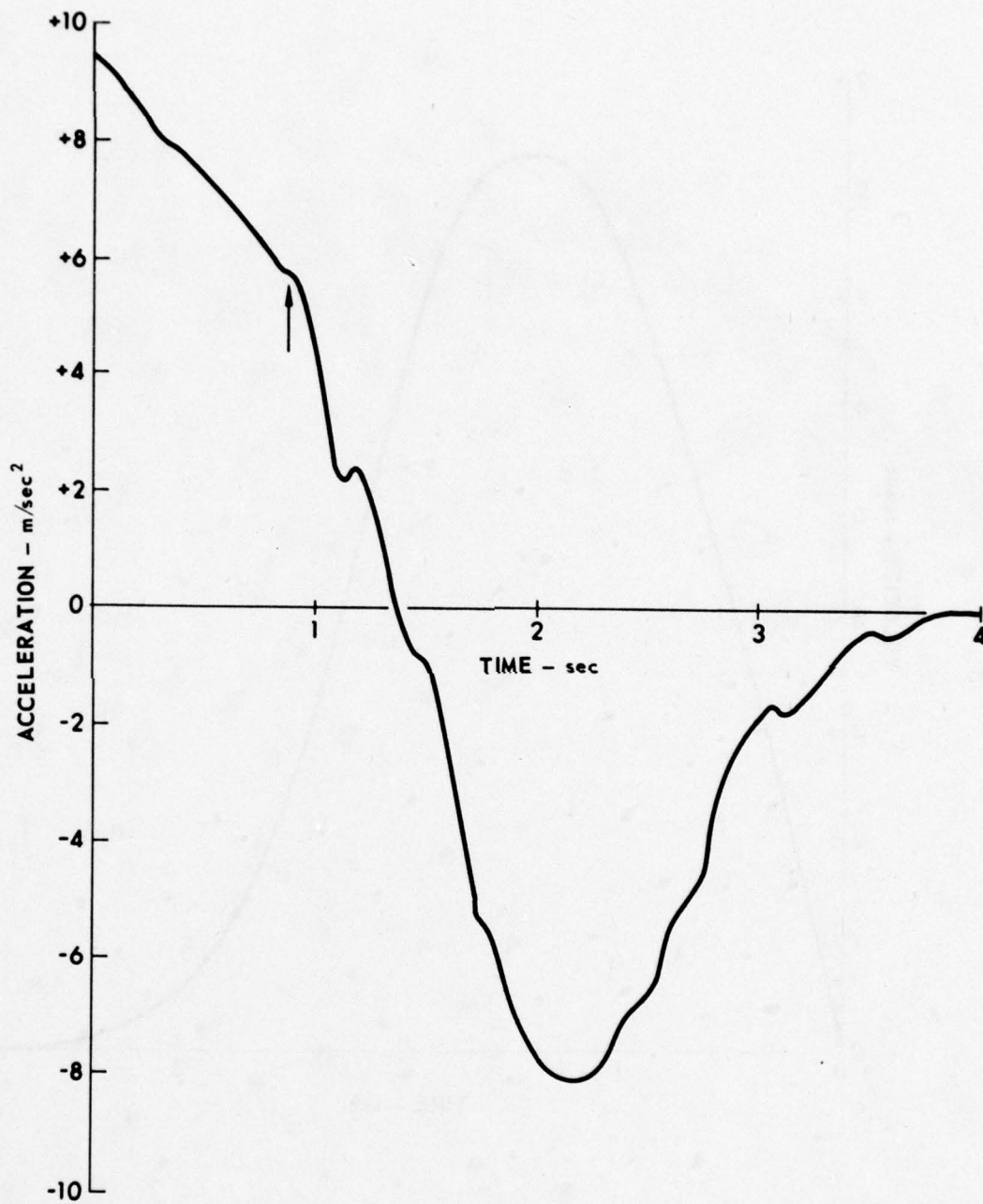


FIGURE 6
ACCELERATION PLOT FOR CORE 3

ARL:UT
AS-79-943
DJS - GA
5-11-79

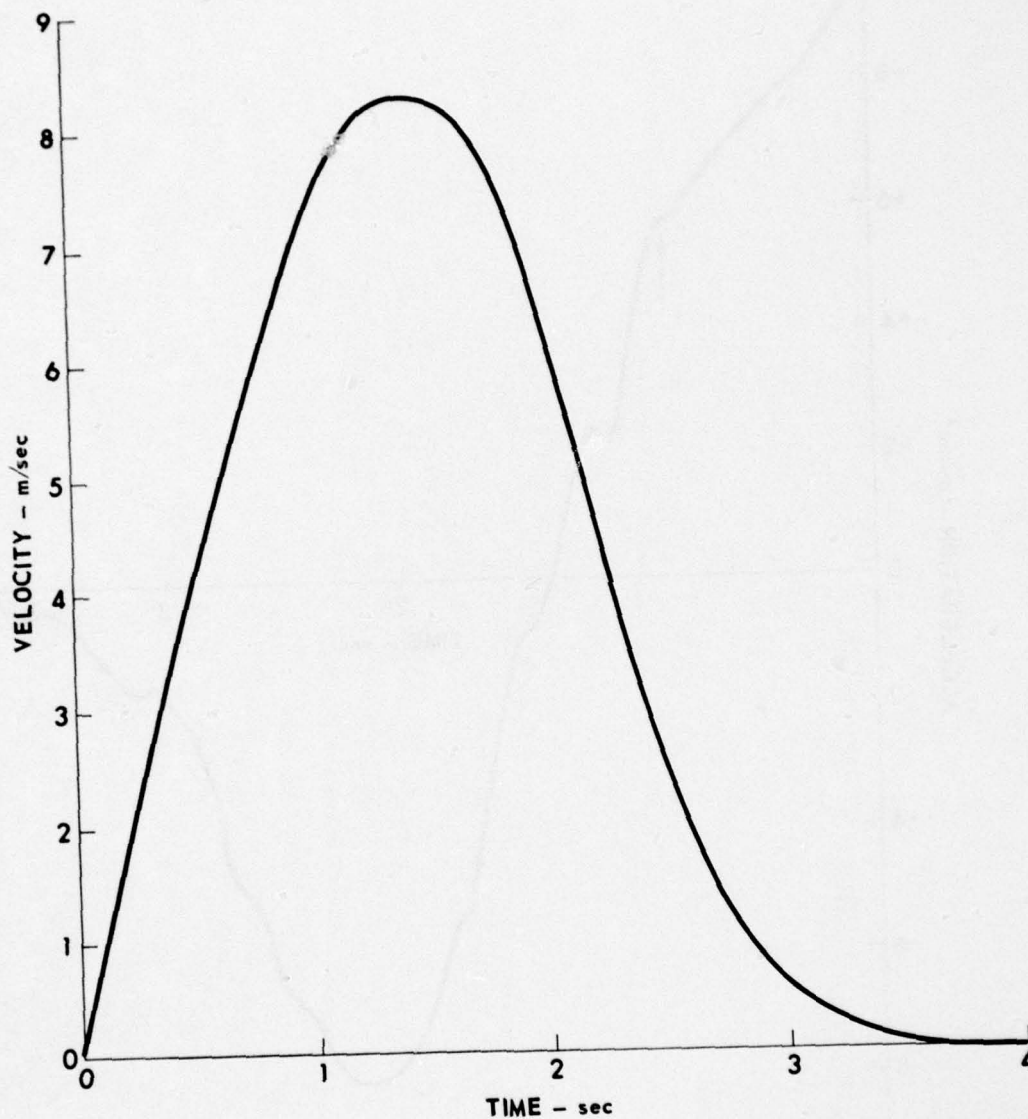


FIGURE 7
VELOCITY PLOT FOR CORE 3

ARL:UT
AS-79-944
DJS - GA
5-11-79

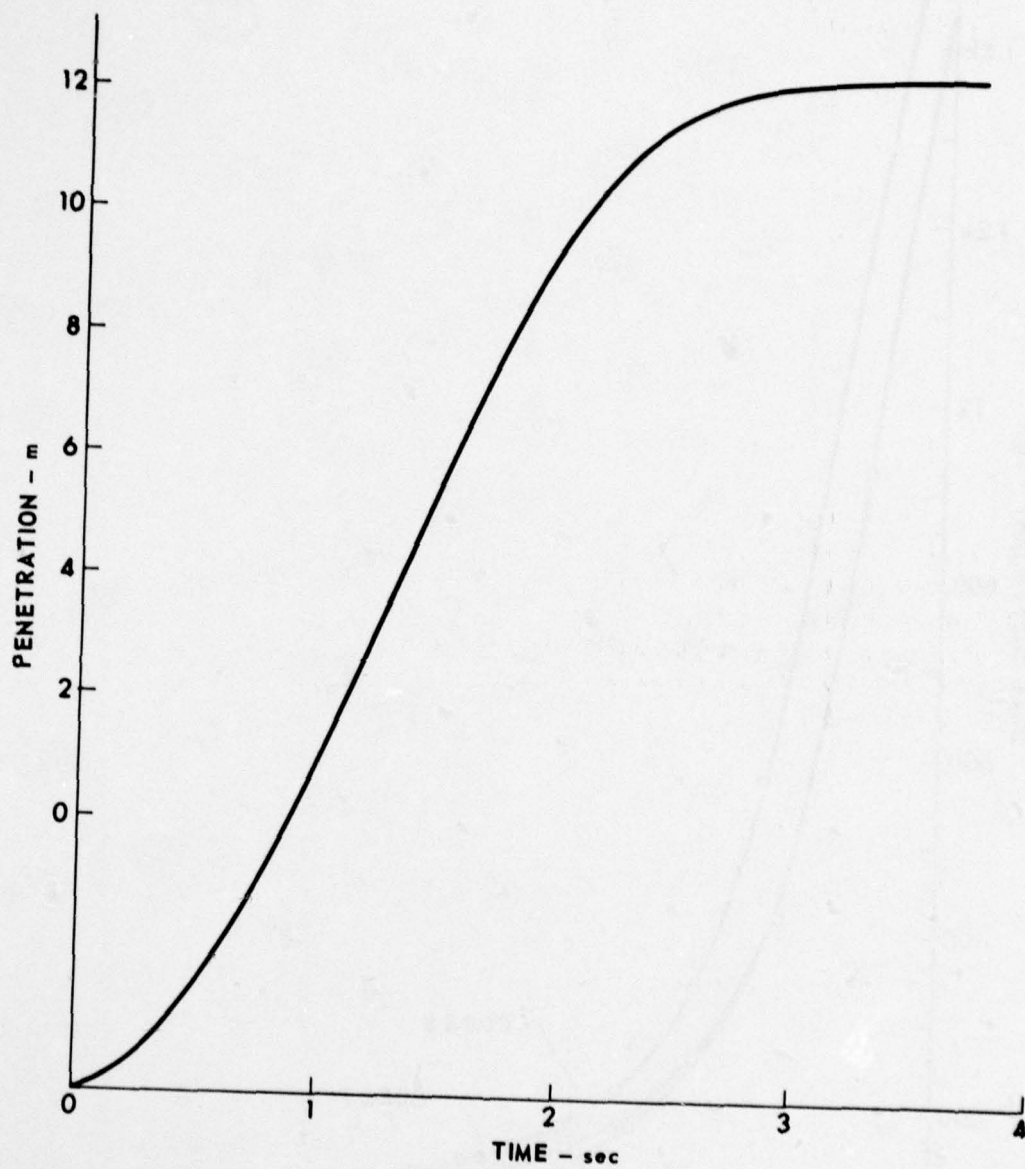


FIGURE 8
PLOT OF BOTTOM PENETRATION FOR CORE 3

ARL:UT
AS-79-945
DJS- GA
5-11-79

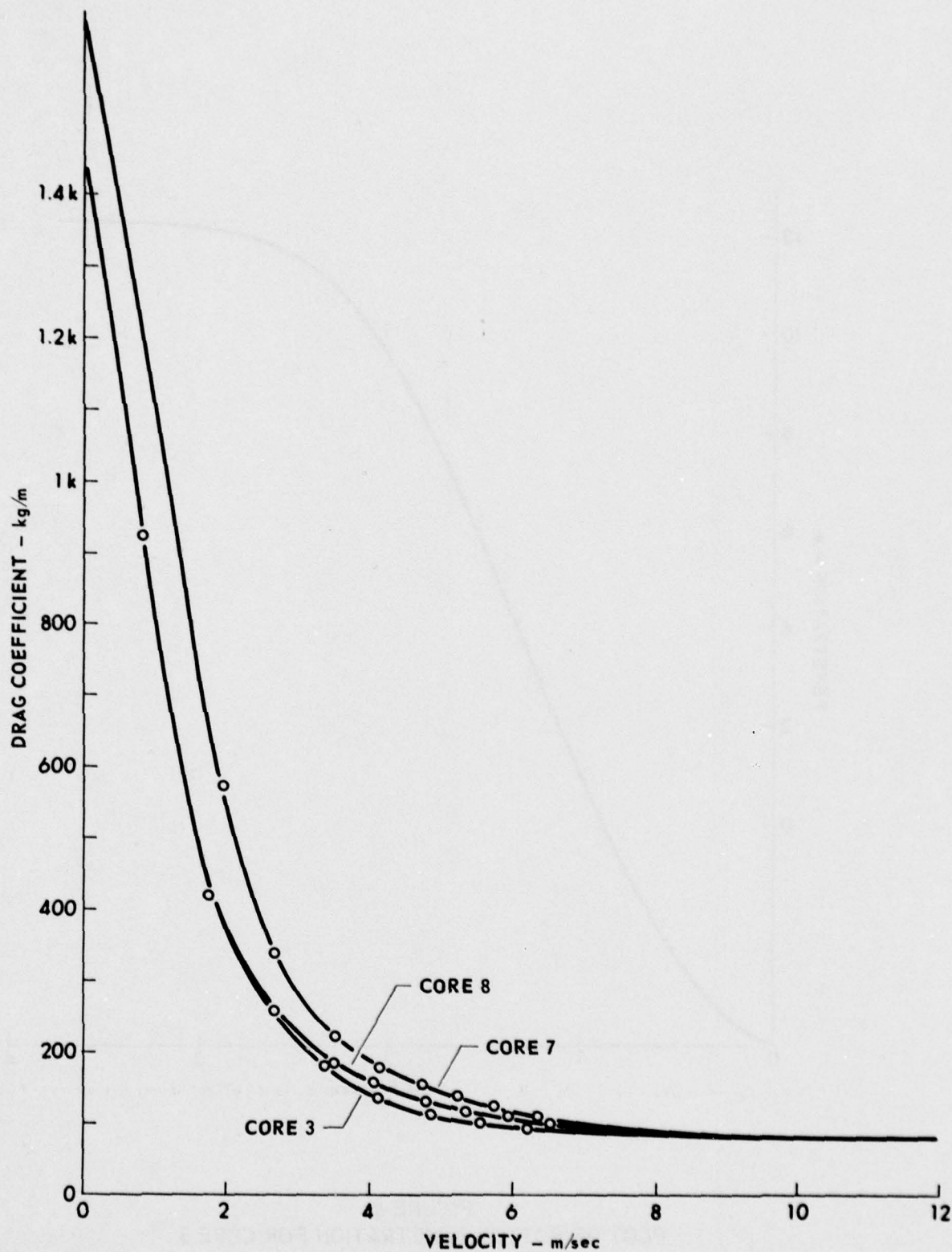


FIGURE 9
PLOT OF HYDRODYNAMIC DRAG COEFFICIENT
AS A FUNCTION OF CORER VELOCITY

ARL:UT
AS-79-946
DJS: GA
5-11-79

where

S = shear strength,

D = outside diameter of the core pipe, and

z = depth of penetration at any instant of time.

To make calculation tractable, some simplifying assumptions must be made: (1) The action of the piston inside the core barrel will be such as to negate any resistance of the sediment moving inside the core barrel. (2) The shear strength of the sediment is not a function of depth. (3) Shear resistance of the sediment on the core barrel is not dependent upon penetration velocity.

For the three cores under consideration, the core barrel was filled with sediment upon retrieval, thus assumption (1) is probably valid. The relative validity of assumption (2) is not really known. The three cores were selected for examination because of the uniformity of the sediment within the core below the first few centimeters. Most in situ shear strength measurements indicate that there is a large gradient in the measured shear strengths of ocean bottom sediments, at least to the 1 to 2 m penetration possible with such devices.

Assumption (3) is not valid since measurements with rotating vanes show that there is variation of measured shear strength with vane rotation rate. However, the dependence of measured shear strength with penetration rate is not a known function; thus, correction cannot be made at this time.

Figure 10 shows the calculated shear strengths of the three cores plotted as a function of depth. The stippled area bracketed by the dashed lines indicates the area of measured values found in the literature for in situ and laboratory measurements with rotating vanes. The first part of the curve for each core lies well within the expected values of shear strength. After about the first 3 m the curves show only a small increase with depth. Cores 3 and 8 are listed on the core descriptions as consisting of a firm moist clay while core 7 is listed

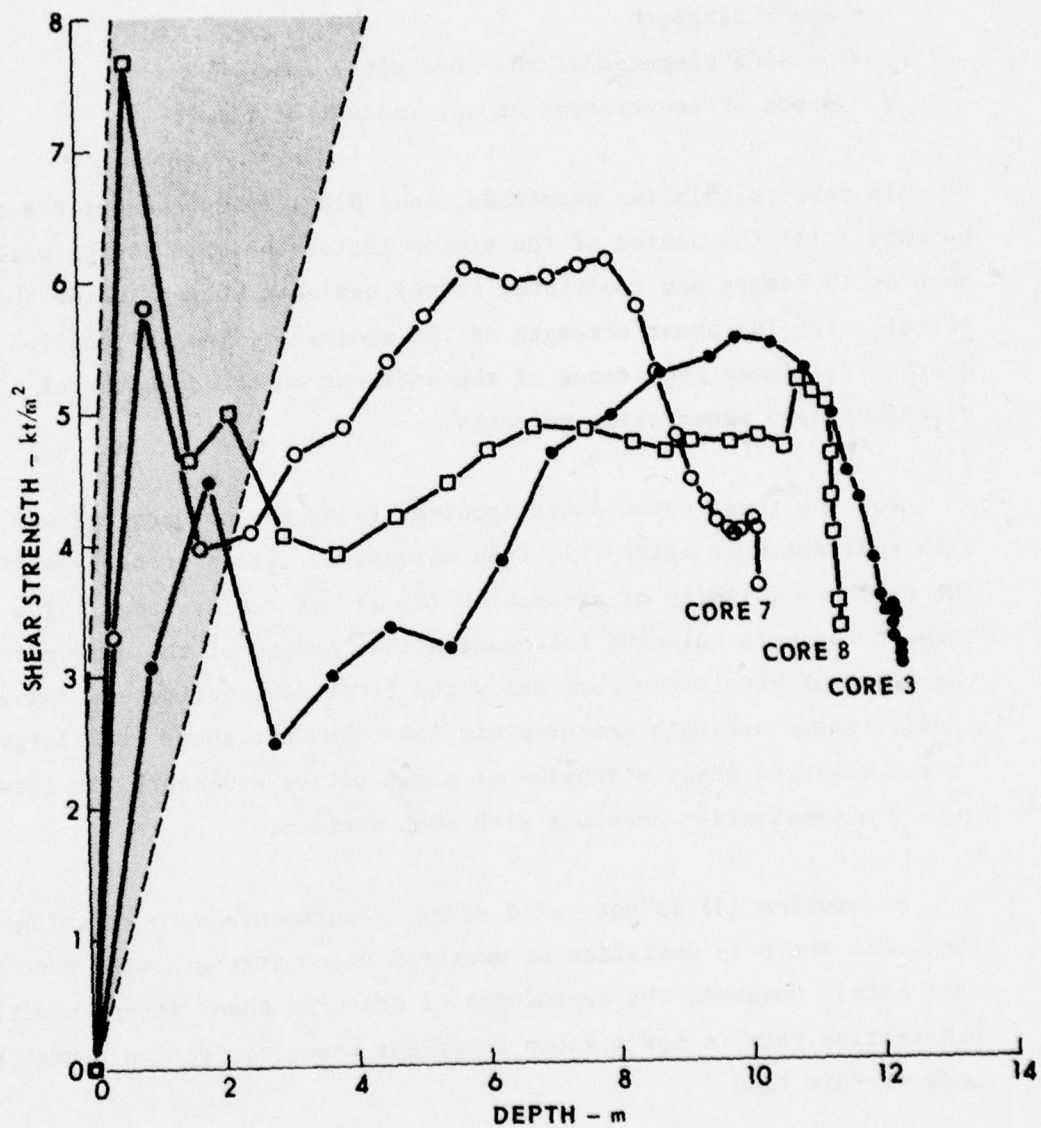


FIGURE 10
SHEAR STRENGTH FOR THREE CORES
PLOTTED AS A FUNCTION OF DEPTH

ARL:UT
AS-79-947
DJS - GA
5-11-79

as a sandy clay. The shear strength shown for core 7 is somewhat higher as would be expected. The last 1 to 2 m of the profiles show a decided droop from the otherwise increasing trend. The droop occurs when the velocity of the corer starts to fall quickly toward zero, indicating that the measurement is indeed velocity dependent. However, the three curves show different dependencies, which would indicate that there are other variables involved.

The gradient in shear strength measured with the corer accelerometer is much less than that measured by other methods. The discrepancy can be due to several causes:

- (1) Most other shear strength measurements are made by rotating vane devices in which shearing action is between two layers of soil. In the accelerometer method, the shearing action is between a layer of soil and the core barrel, which has an unknown roughness.
- (2) It is possible that the corer will strike the bottom in a nonvertical direction, thus introducing error into the accelerometer record.
- (3) It is assumed that the corer has a constant diameter the length of the pipe; however, the cutter at the bottom end is somewhat larger in diameter. This would tend to reduce the shear resistance on the remainder of the core barrel by an unknown amount. Also, because the core pipe usually has at least one joint at the middle which is slightly larger in diameter, another unknown factor is added to the resistance once the joint penetrates the sediment.

The above considerations reduce the value of the shear strength measurements as they now stand. However, an independent measurement of the in situ shear strength of a cored sediment would enable corrections to be made to the data and thus upgrade their value. Such an independent measurement could be made by instrumenting the corer with a small cone penetrometer such as that developed by Stoll.⁹

Further investigation into the effect of penetration rate is also required to upgrade the data.

IV. LABORATORY MEASUREMENTS

A. Introduction

Accurate values of the acoustic parameters of marine sediments are required to successfully model and interpret acoustic interactions with the ocean bottom. Although direct in situ measurement offers the most reliable determination of these parameters, it is not always the most practical or feasible. Therefore, theoretical and empirical relationships are used to supplement what data are available. These data are often of a physical nature, such as grain size or mineral composition, rather than of an acoustical nature. Sufficient acoustic measurements are necessary to adequately evaluate the various physical characteristics. These measurements are most easily made in the laboratory, where control over physical parameters is possible. Part of the ONR funded sediment program at ARL:UT has been the accumulation of such laboratory measurements. Particular emphasis has been placed on shear wave velocity and attenuation since these are not generally available for unconsolidated sediments.

To monitor the relationship between an acoustic parameter, such as wave velocity, and a physical characteristic, such as grain size, several sediments are required; ideally they should be identical except for the property of interest. Using artificial sediments is the easiest way to assure such uniformity. Four sizes of glass beads to simulate sand were chosen for the investigations discussed here. Additional studies have been made in three natural sands to assess the effect of grain shape as well as provide values more representative of natural sediments. Sands rather than silts or clays were chosen because of divergent theoretical predictions for the latter. The differences depend on the magnitude of relative grain and pore fluid movement caused by the acoustic disturbance.

Theoretical predictions for shear wave propagation will be discussed in detail in a later section.

B. Sediment Physical Properties

The grain size distributions of the sediments as determined by sieve analysis are shown in Fig. 11. The beads are commercial glass shot abrasives. They are referred to by the last letters of the manufacturer's designations with the following nominal sizes in microns - L, 74-44; MH, 210-105; XHX, 420-210; XPX, 710-350. The beads are spherical with not more than 15% irregularly shaped particles and with less than 1% angular grains. The density of the glass itself is given as 2.5 g/cc with a sound velocity of 5300 m/sec at room temperature and a modulus of elasticity of 10^3 N/m.

The densities and porosities of the bulk beads as measured in the laboratory are given in Table II. The density and porosity of a regular packing of identical spheres should not change with grain diameter. The expected value of porosity for a random packing of like spheres is 0.38.¹⁶ The fluctuation of the measured values about the ideal porosity reflects variations in grain size and shape; however, to first order, the porosities are the same. The densities and porosities were determined by adding a known volume of water to a weighed volume of beads packed by vibration. The standard deviations of four separate measurements are given in Table II.

The properties of the natural sands are also shown in Fig. 11 and Table II. The Panama City, or PC, sand is a mature, medium white quartz beach sand from Panama City, Florida. The Ottawa Sand is a supermature, medium to coarse quartz sand sold as a standard for field tests of soil density. Textural maturity reflects the sorting and angularity of the grains. The Ottawa grains are fairly well rounded; the PC grains are more angular. The red sand is a submature, coarse, riverbed sand of

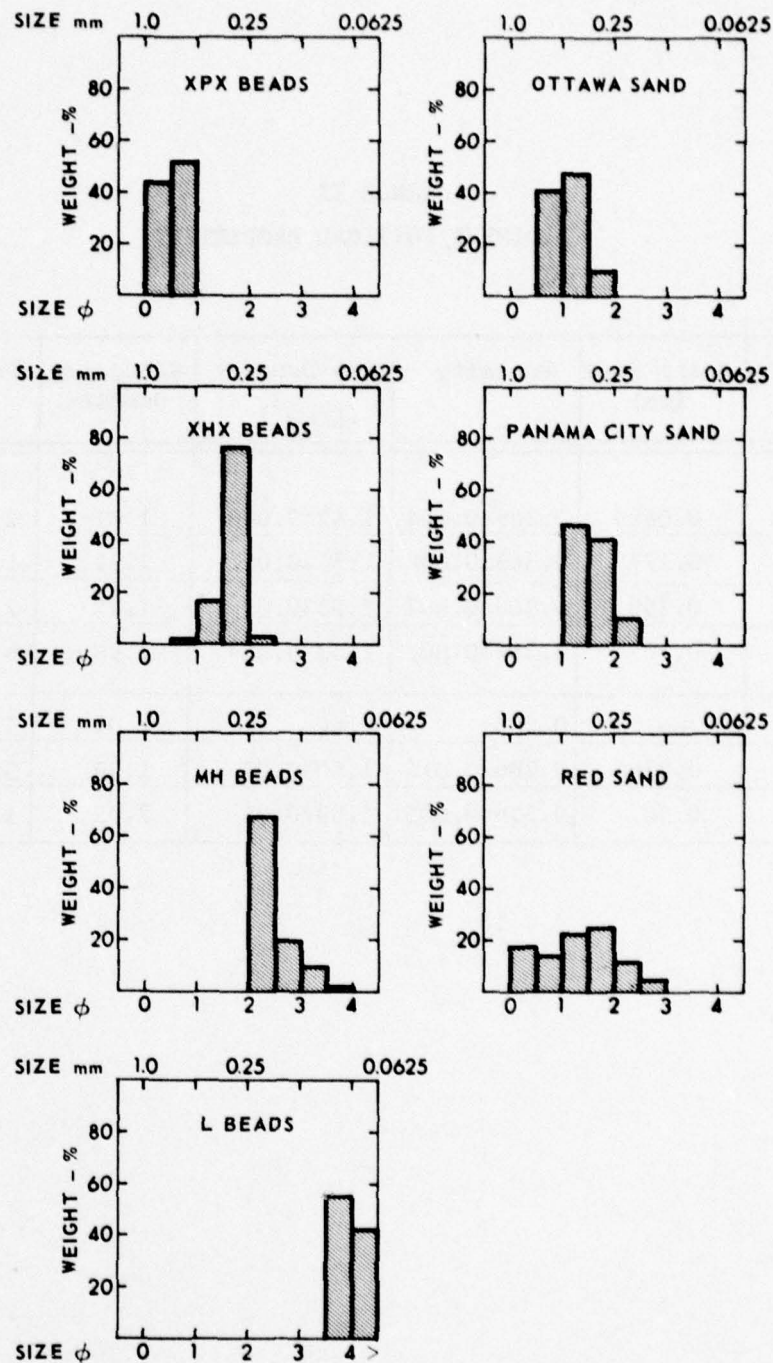


FIGURE 11
SEDIMENT GRAIN SIZE DISTRIBUTIONS

ARL:UT
AS-79-204
DWB-GA
2-7-79

TABLE II
SEDIMENT PHYSICAL PROPERTIES

Sediment	Grain Size (mm)	Porosity	Dry Density (g/cm ³)	Saturated Density	Permeability (cm ²)
L	0.0625	0.389±0.004	1.42±0.008	1.81	2.58×10 ⁻⁸
MH	0.177	0.365±0.008	1.55±0.02	1.92	1.70×10 ⁻⁷
XHX	0.250	0.369±0.007	1.55±0.01	1.92	7.76×10 ⁻⁷
XPX	0.707	0.373±0.006	1.53±0.009	1.90	4.63×10 ⁻⁶
Red	--	0.383	1.64	2.02	5.71×10 ⁻⁷
PC	0.354	0.386±0.014	1.60±0.03	1.99	3.79×10 ⁻⁷
Ott	0.50	0.356±0.005	1.69±0.01	2.05	1.39×10 ⁻⁶

mixed quartz and feldspar grains. Values for the density and bulk modulus of pure quartz are 2.65 g/cm^3 and $3.8 \times 10^{11} \text{ dyn/cm}^2$.

Table II also lists the permeability of the sediments. This is a natural parameter to consider with regard to the possible displacement under acoustic stress of the pore fluid relative to the frame. A constant head permeameter was constructed according to ASTM standards (ASTM D2434-68) to obtain these values. Figure 12 is a scale drawing of the apparatus. A differential pressure gauge was used to measure the pressure drop h due to the flow resistance of the sediment. The coefficient of permeability k is related to the quantity of water Q that flows in time t by

$$k = \frac{QL}{thA} \quad , \quad (5)$$

where L is the sample length and A the cross sectional area. Figure 13 is a sample plot of flow rate Q/At versus the pressure gradient h/L . The slope of the line is the permeability k in centimeters per second at the temperature T of the experiment. The ratio of the viscosity of water at T to that at 20°C was used to reduce the measurements to a standard temperature/viscosity reference. The influence of fluid viscosity and density can be removed from the permeability constant k by defining an absolute permeability

$$K = \frac{k\eta}{\rho g} \quad , \quad (6)$$

where η is the fluid viscosity, ρ is the density, and g is the acceleration due to gravity. For water at 20°C , $K(\text{cm}^2) = 1.2 \times 10^{-5} k(\text{cm/sec})$. Measured values of the absolute permeability in cm^2 are given in Table II.

The permeability measurements vary as the square of the mean grain size diameter in agreement with the Kozeny-Carman equation for uniform spheres.

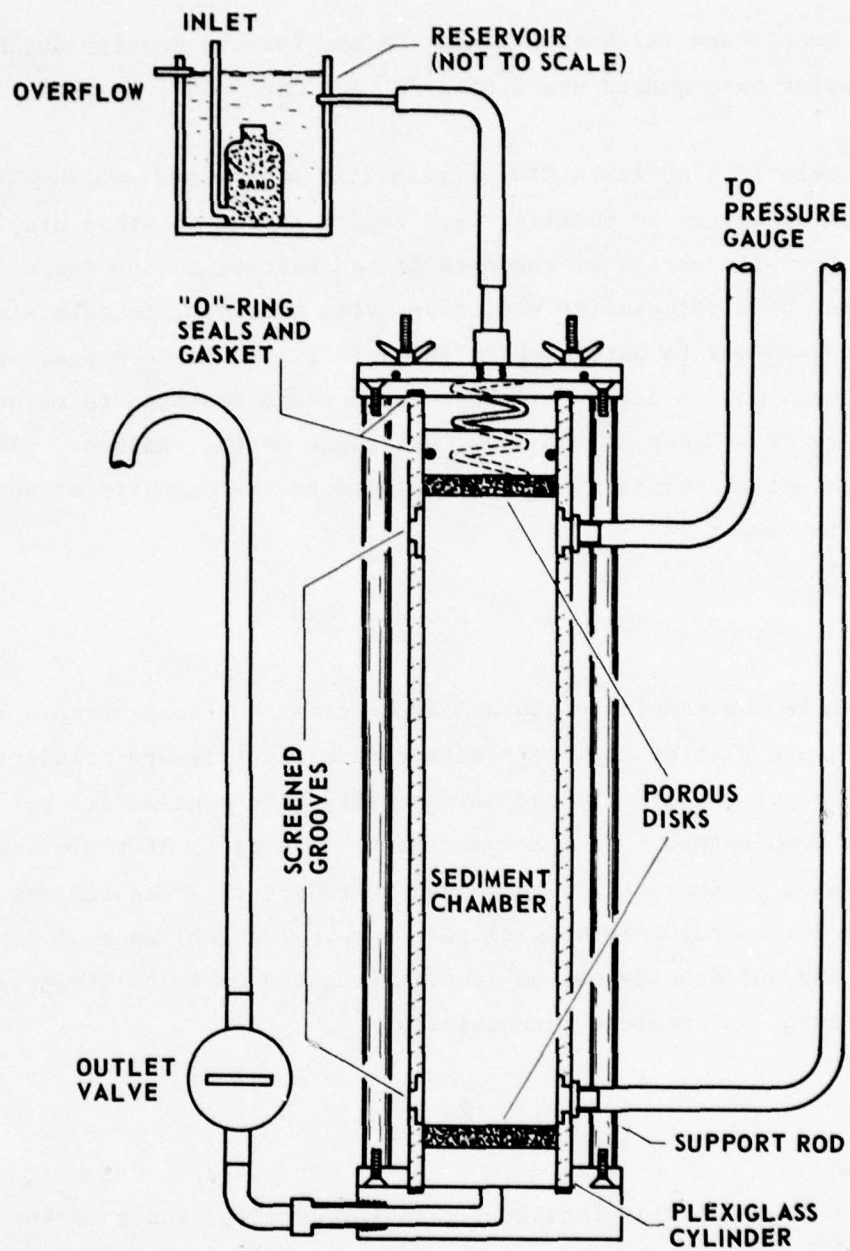


FIGURE 12
CONSTANT HEAD PERMEAMETER

ARL:UT
AS-79-205
DWB-GA
2-7-79

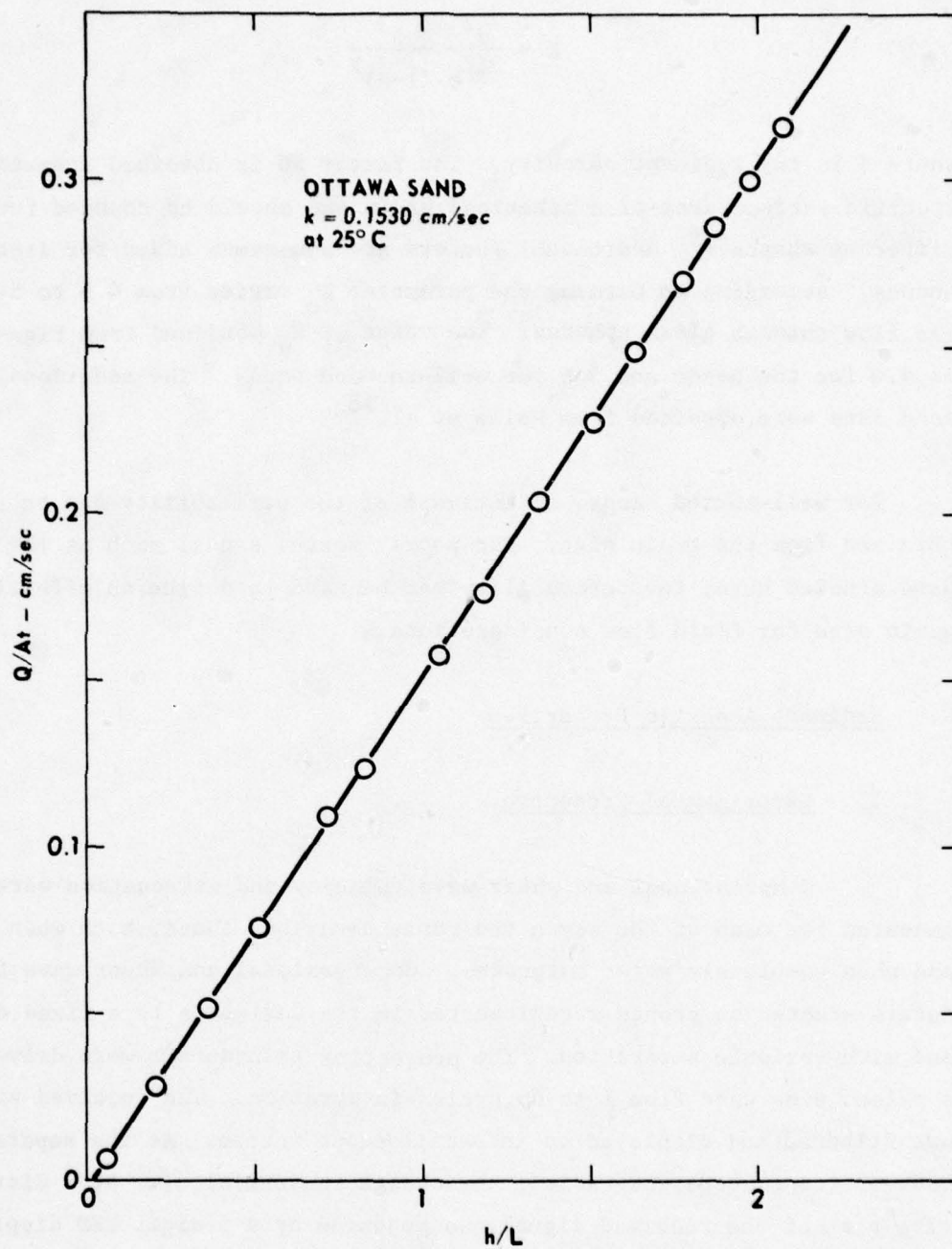


FIGURE 13
DETERMINATION OF SEDIMENT PERMEABILITY

ARL:UT
AS-79-206
DWB-GA
2-7-79

$$K = \frac{d^2}{36K_o} \frac{\beta^3}{(1-\beta)^2} \quad , \quad (7)$$

where β is the sediment porosity. The factor 36 is obtained from the specific surface area of a spherical grain and should be changed for different shapes.¹⁶ Additional factors are sometimes added for irregular shapes. According to Carman, the parameter K_o varies from 4.5 to 5.1 for gas flow through glass spheres. The value of K_o obtained from Fig. 14 is 4.0 for the beads and 5.6 for well-rounded sands. The additional sand data were obtained from Nolle et al.¹⁸

For well-sorted sands, an estimate of the permeability can be obtained from the grain size. For poorly sorted sands, such as the red sand studied here, the permeability can be used to define an effective grain size for fluid flow considerations.

C. Sediment Acoustic Properties

1. Experimental Procedure

Compressional and shear wave velocity and attenuation were measured for each of the seven sediments described above, both when dry and when completely water saturated. Compressional and shear wave transducers mounted on probes were inserted in the sediments to a fixed depth and with variable separation. The projecting transducers were driven by a pulsed sine wave from 1 to 40 cycles in duration. The received signal was filtered and displayed on an oscilloscope screen. As the separation between transducers was varied, the change in arrival time of a distinctive peak of the received signal, as measured by a 5-digit LED display function of the oscilloscope, was used to calculate wave velocity. Attenuation was calculated from the decay of signal amplitude with separation, as measured peak to peak on the oscilloscope screen for the shorter signals, or rms with a sampling voltmeter for the longer signals. The filter was adjusted for a constant Q of 10 to ensure that the cycle

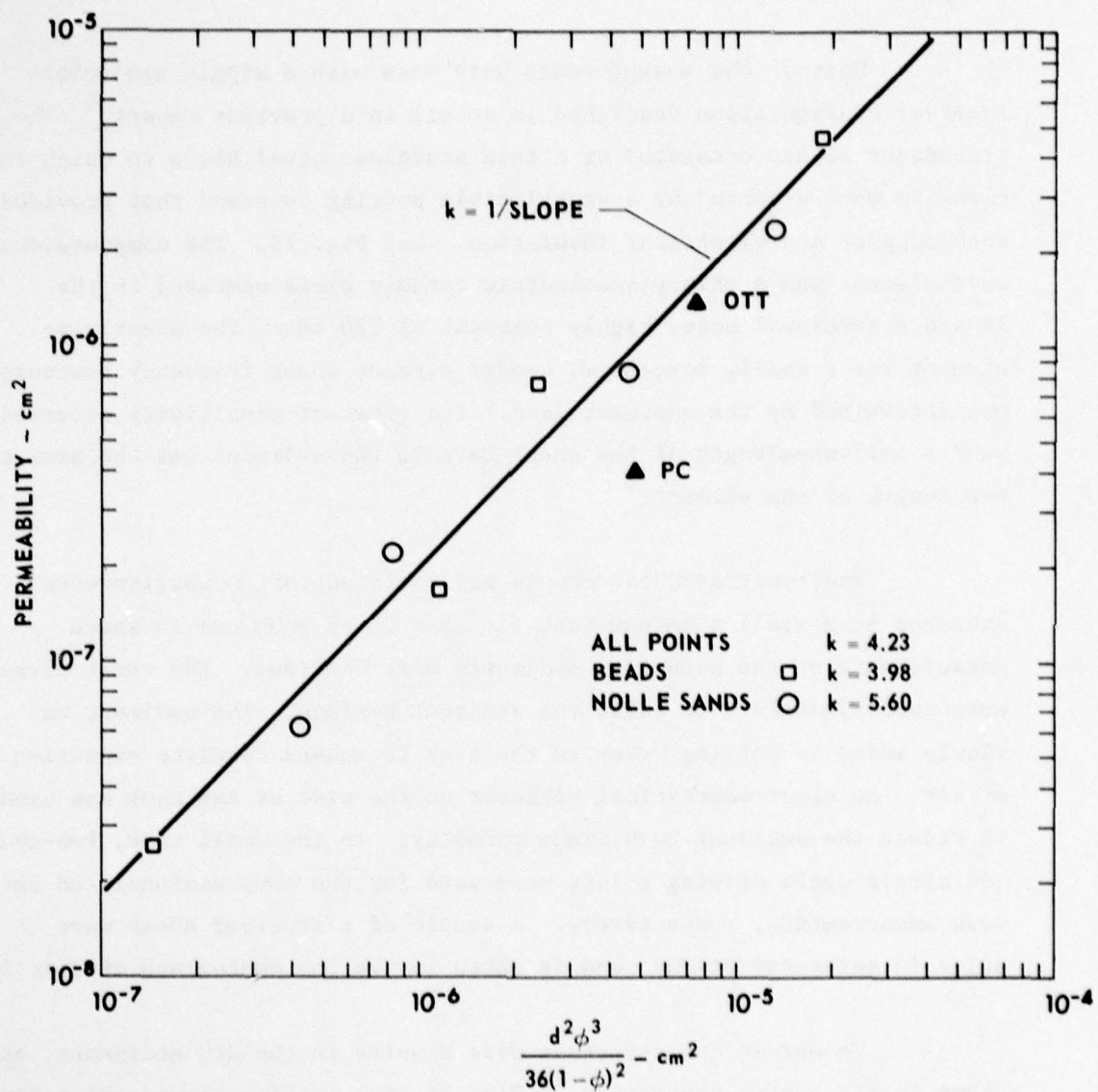


FIGURE 14
DETERMINATION OF KOZENY-CARMAN CONSTANT
RELATING PERMEABILITY TO GRAIN SIZE

ARL:UT
AS-79-207
DWB-GA
2-7-79

frequency of the driving pulse was representative of the received signal frequency.

Most of the measurements were made with a single projector-receiver configuration described in detail in a previous report.⁵ The transducer mounts consisted of a thin stainless steel blade to which the elements were attached by a semiflexible potting compound that provided both support and electrical insulation. See Fig. 15. The compressional wave element was a thin piezoelectric ceramic plate operated in the length extensional mode, highly resonant at 120 kHz. The shear wave element was a small, broadband, bender element whose frequency response was determined by the sediment load. Its greatest sensitivity occurred when a half-wavelength of the shear wave in the sediment was the same as the length of the element.⁸

The two transducer mounts and their support mechanism were attached to a small aluminum tank (16 cm x 20 cm x 30 cm) in which measurements on the saturated sediments were obtained. The shear elements were approximately 9 cm below the sediment surface. The sediment was slowly added to boiling water in the tank to ensure complete expulsion of air. An electromechanical vibrator on the side of the tank was used to reduce the sediment to minimum porosity. In the small tank, two-cycle and single cycle driving pulses were used for the compressional and shear wave measurements, respectively. A sample of a received shear wave pulse in saturated Ottawa sand is shown in the top photograph of Fig. 16.

To obtain quality shear wave results in the dry sediments, as shown in the bottom photograph of Fig. 16, two modifications were made. First, the transducer mounts were coated with conducting paint to eliminate electrical feedover that was obscuring the beginning of the received pulse. Second, a larger tank was constructed to offer better discrimination between the direct arrival and reflected events. This was a wood box lined with porous foam with inside dimensions of 75 cm x 36 cm x 24 cm; it also had a vibrator attached. The transducers were carefully placed at the same depth in both tanks.

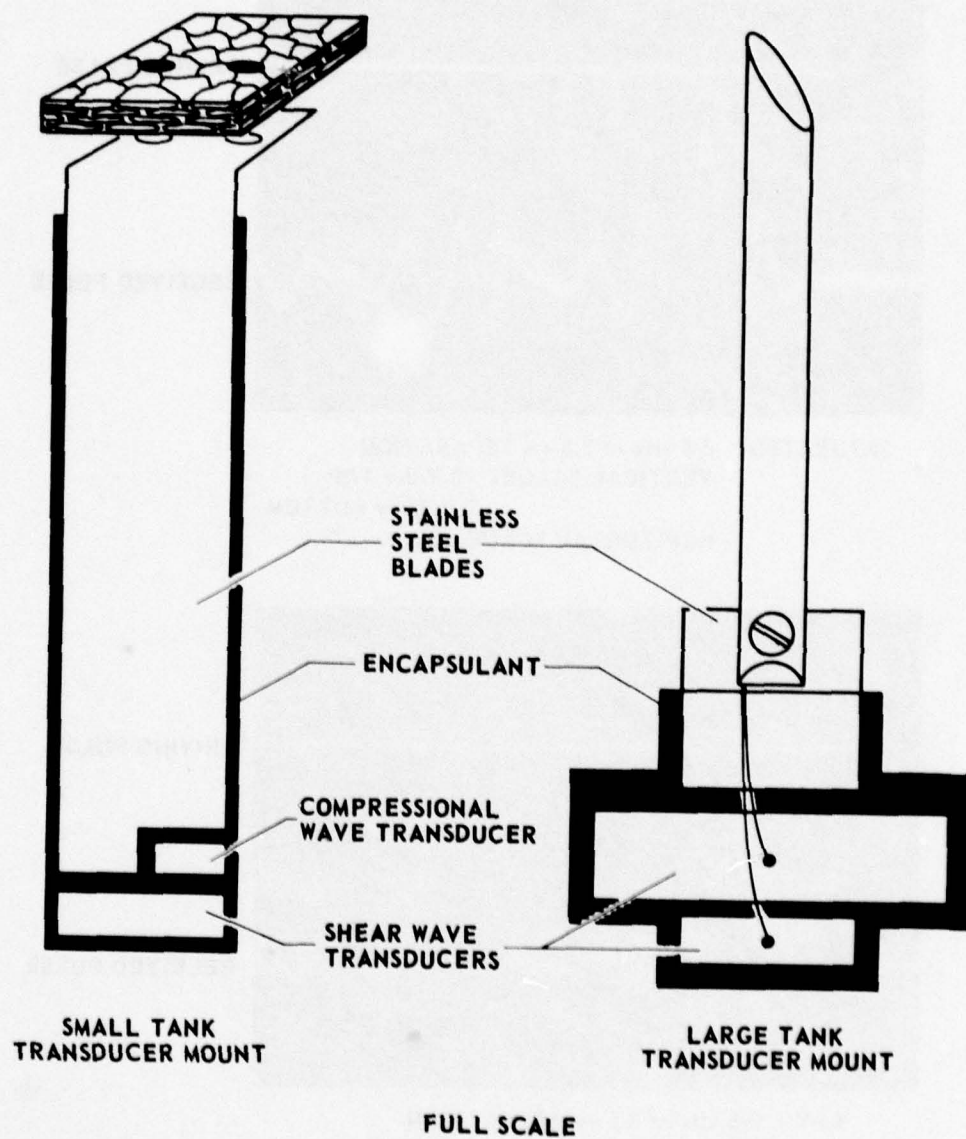
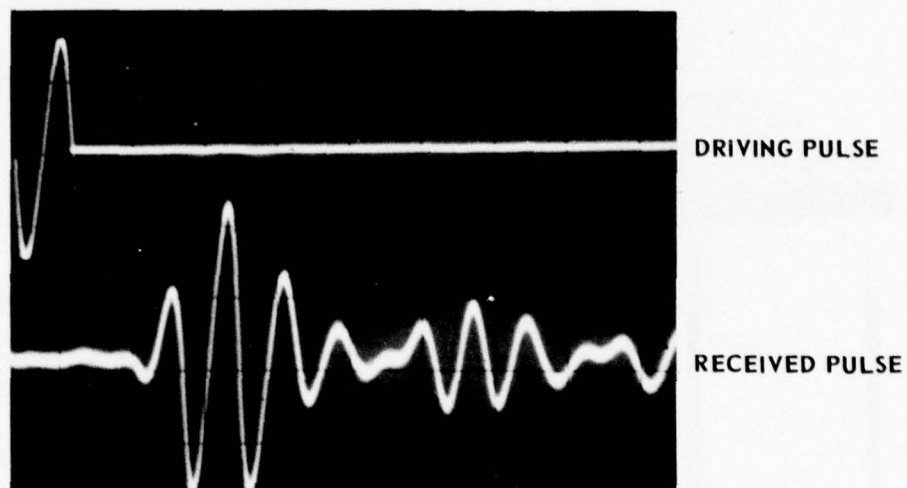
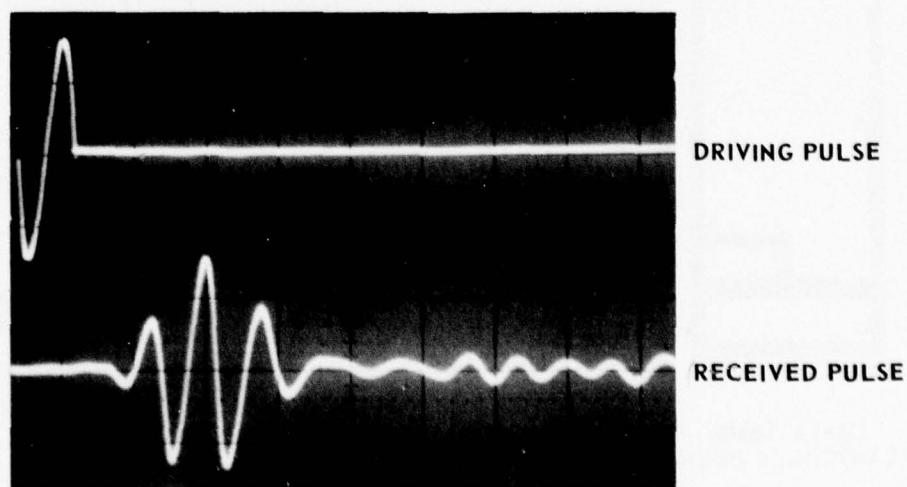


FIGURE 15
TRANSDUCER MOUNTS

ARL:UT
AS-79-208
DWB-GA
2-7-79



SATURATED 2.5 kHz at 3.5 cm SEPARATION
 VERTICAL SCALE: 10 V/div TOP
 0.2 V/div BOTTOM
 HORIZONTAL SCALE: 0.5 msec/div



DRY 2.5 kHz at 3.5 cm SEPARATION
 VERTICAL SCALE: 10 V/div TOP
 0.5 V/div BOTTOM
 HORIZONTAL SCALE: 0.5 msec/div

FIGURE 16
 SHEAR WAVE SIGNAL QUALITY - OTTAWA SAND

Each time the transducers were moved in either the dry or saturated materials, the sediment was vibrated to ensure uniform packing. However, this disturbance had a marked influence on the received shear pulse. Measurements made immediately after vibration showed longer delay times and larger amplitudes than measurements made after the sediment had been allowed to settle. The decay in transit time was approximately exponential and reached steady values more quickly if vibration was slowly decreased rather than abruptly stopped at high amplitudes. Readings were made with a uniform settling time of 1 1/2 h, after 15 min of low amplitude vibration. The transducers were active the last 15 min of the waiting period.

Relatively small physical disturbances of the tank during measurement, such as tapping the side of the tank with a finger, would cause the transit time to increase noticeably. Larger disturbances would completely distort the wave shape. The dry glass beads were particularly sensitive to such external vibrations.

The small compressional wave transducers used in the saturated sediments did not couple sufficiently well with the dry material for a compressional wave to be observed. To obtain estimates of the compressional wave velocity and attenuation in the dry sediments, a small press was constructed from an aluminum cylinder 15 cm in diameter and 30 cm high. A projector and two receivers with surface area of approximately 1 cm² each were mounted on short rods at the bottom of the press such that the propagation path was across the diameter of the cylinder. The two receivers were 4.26 cm and 4.97 cm from the projector, as determined by calibration in three different liquids with known sound velocity. The relative amplitude difference between the received signals in the fluids was also measured. Additionally, a pressure sensitive transducer was calibrated and fixed to the bottom of the cylinder. A good quality signal was obtained for all of the sediments with only a small amount of external frame pressure. It was hoped that results for velocity and attenuation could be extrapolated to zero excess pressure. However, the

sensitivity was such that only order of magnitude estimates could be obtained in that manner. Thus, values are reported only for those sediments in which a signal was detected without compression. Although the received signals were of poor quality, the results were repeatable to within less than 10%. A filtered pulse was used with a frequency of approximately 20 kHz.

To measure the variation of shear wave velocity and attenuation with frequency, a wider frequency band was desired than that obtained from the bender elements described above. A bender element twice as large operating at half the frequency was found to extend the usable bandwidth to both higher and lower frequencies. Three probes, as shown in Fig. 15, were constructed with both large and small bender elements. The probes were mounted in a line with the receivers on each side of the projector. All separations were adjustable and the probes were held rigidly at the desired locations. The mounting rods allowed the probes to be inserted just beyond the center of a new, much larger, aluminum tank (46 x 71 x 56 cm). The tank was designed to be its own vacuum chamber; however, it was necessary to boil the glass beads to obtain complete deaeration. The tank was vibrated by an eccentrically loaded electric motor mounted on the tank stand. Readings were made after a 24 h settling period.

The larger tank was constructed so that a longer driving pulse could be used to give a better definition of frequency. This was not possible in the unlined tank primarily due to reflection from the bottom. Therefore, the larger tank was lined with a 3 cm layer of porous foam with randomly spaced foam pyramids 6 cm in height. A typical transmission is shown in Fig. 17. Noise interference was still present to a noticeable extent for the large shear elements, and both elements showed some pulse distortion at short wavelengths. Therefore, most of the data were obtained from short pulses with the longer pulses serving as a means of quality estimation.

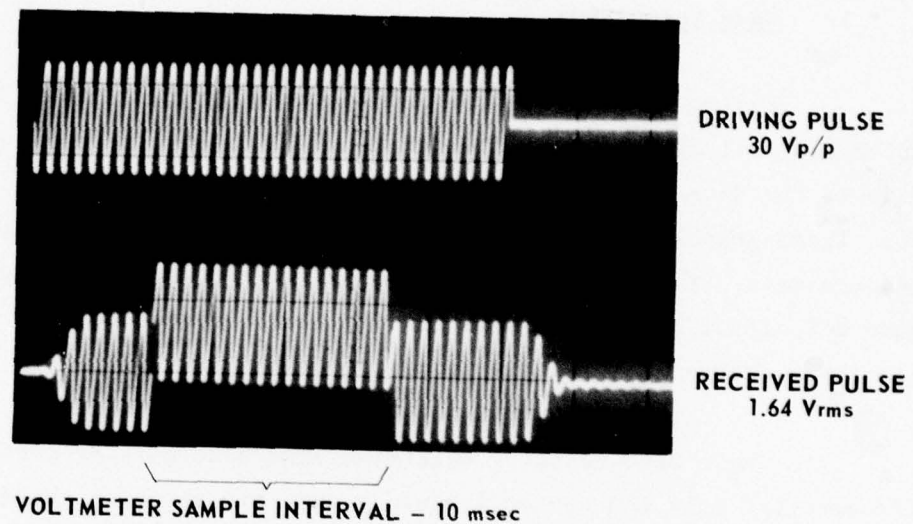


FIGURE 17
MULTICYCLE SHEAR WAVE PULSE
SMALL ELEMENTS IN LARGE TANK
SATURATED MH BEADS
1.5 kHz 9 cm SEPARATION

2. Data Reduction

The acoustic properties of the sediments are compiled in Table III. Small tank results refer to either the small aluminum tank or the wooden box. Large tank results were obtained in the larger aluminum tank. In both cases, the dry compressional wave values were obtained in the press apparatus as described above.

3. Wave Velocities :

Except for the compressional wave velocities in the dry materials, all of the velocities given in Table III are least squares fits to the data at various separations, as shown in Figs. 18, 19, and 20. These graphs are included to demonstrate the relative quality of the measurements. The correlations are excellent for the compressional wave velocities but are less so for the shear waves in the dry materials. Not shown are points widely divergent from the mean.

Shear wave velocity determinations were made at several frequencies; only the center frequency data are shown in the figures. Velocities at the different frequencies differed by less than 5 m/sec, which is within the confidence limits obtained from the least squares fits for the dry measurements.

4. Attenuation

Compressional wave attenuations for the saturated sediments were attained by a least squares fit of amplitude versus separation after correction for spreading loss. The correction was determined by measuring the amplitude decay in water. The above least squares fit method is illustrated in Fig. 21.

The same procedure, with the assumption of center to center spherical spreading, was applied to the shear wave measurements;

TABLE III
SEDIMENT ACOUSTIC PROPERTIES

SMALL TANK

Sediment	Saturated				Dry			
	c_p	δ_p	c_s	δ_s	c_p	δ_p	c_s	δ_s
Beads								
L	1850	0.096	63	0.87	98	0.34	95	2.0
MH	1810	0.054	65	0.37	95	1.2	84	1.1
XHX	1830	0.040	82	0.32	110	1.4	122	2.8
XPX	1820	0.035	53	0.31	--	--	76	1.3
Sands								
Red	1710	0.045	55	1.2	--	--	73	0.59
PC	1740	0.015	105	0.34	220	0.58	220	0.4
Ott	1800	0.055	47	2.0	--	--	66	1.2

LARGE TANK

MH	1850	0.079	100	0.48	95	1.2	124	0.14
PC	--	--	145	0.72	220	0.58	185	0.14

c in meters per second $\delta = \frac{\alpha c}{8.686 f}$

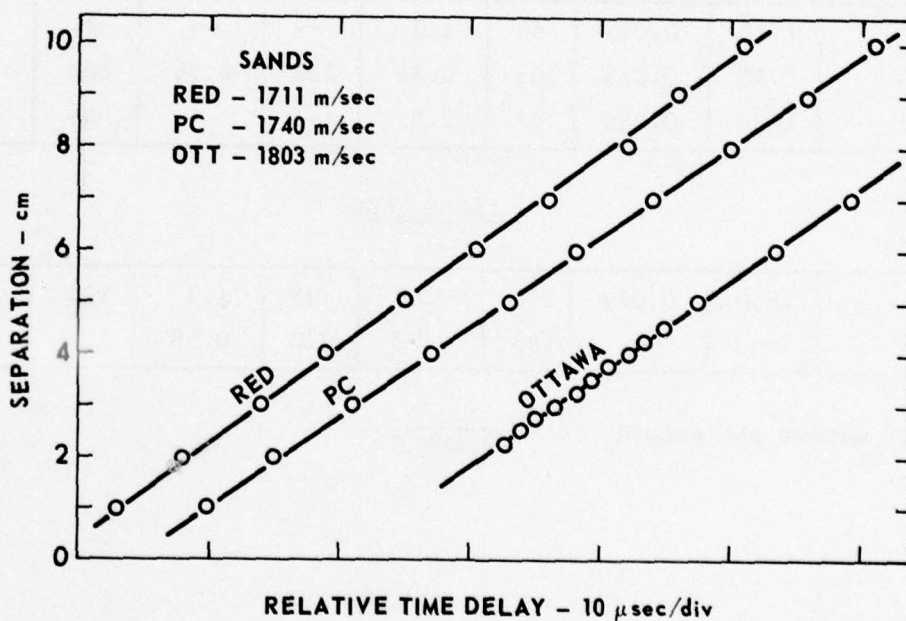
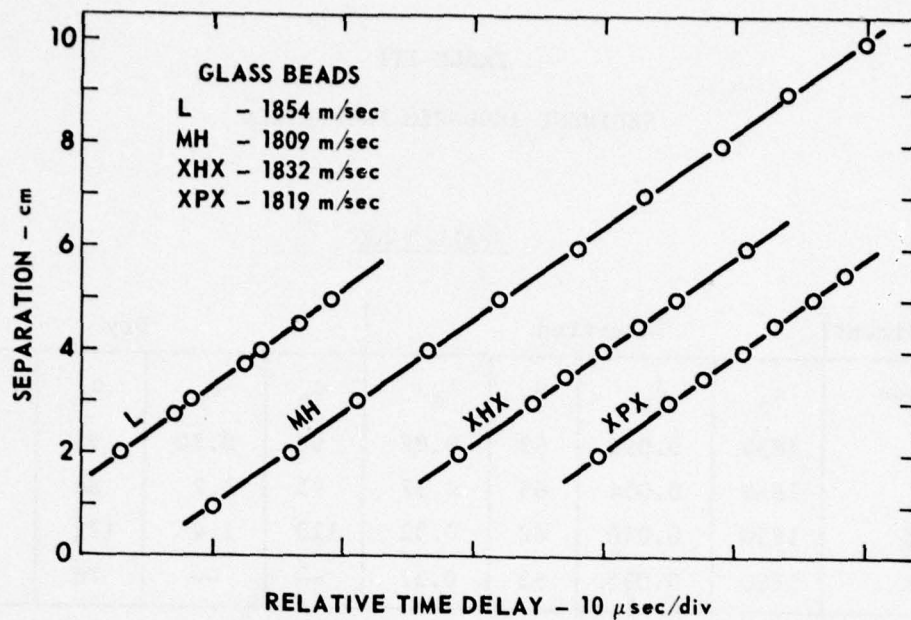
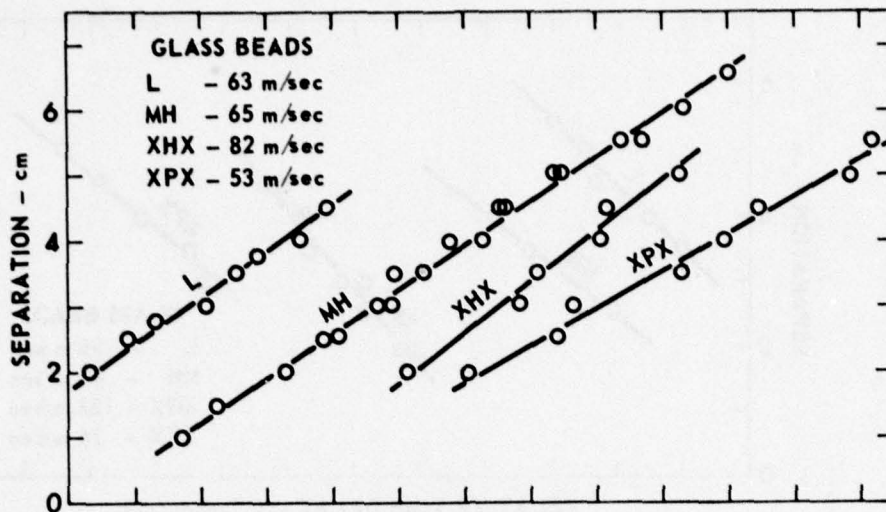
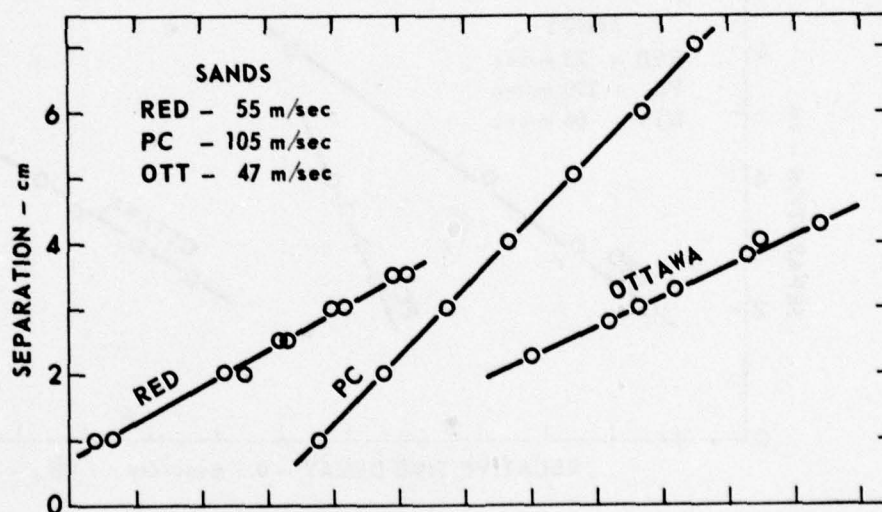


FIGURE 18
DETERMINATION OF COMPRESSIONAL WAVE VELOCITY IN SATURATED SEDIMENTS



RELATIVE TIME DELAY - 0.1 msec/div



RELATIVE TIME DELAY - 0.1 msec/div

FIGURE 19
DETERMINATION OF SHEAR WAVE VELOCITY
IN SATURATED SEDIMENTS

ARL:UT
 AS-79-210
 DWB-GA
 2-7-79

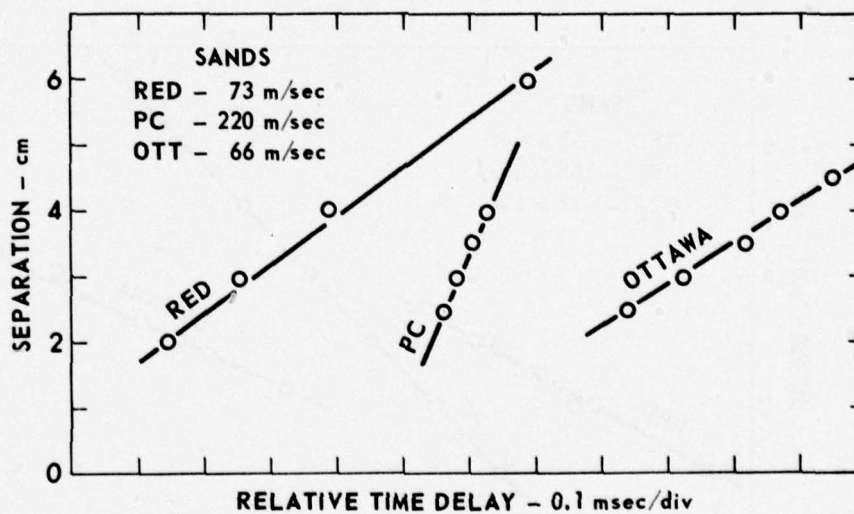
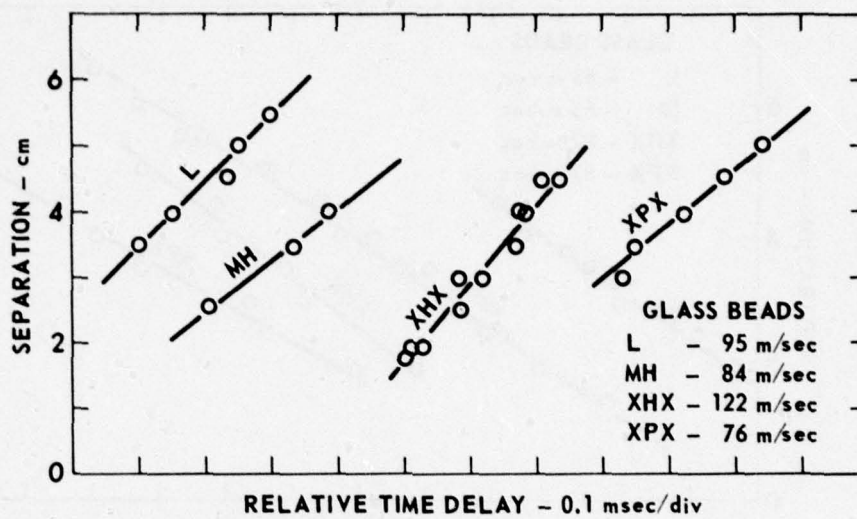


FIGURE 20
DETERMINATION OF SHEAR WAVE VELOCITY IN DRY SEDIMENTS

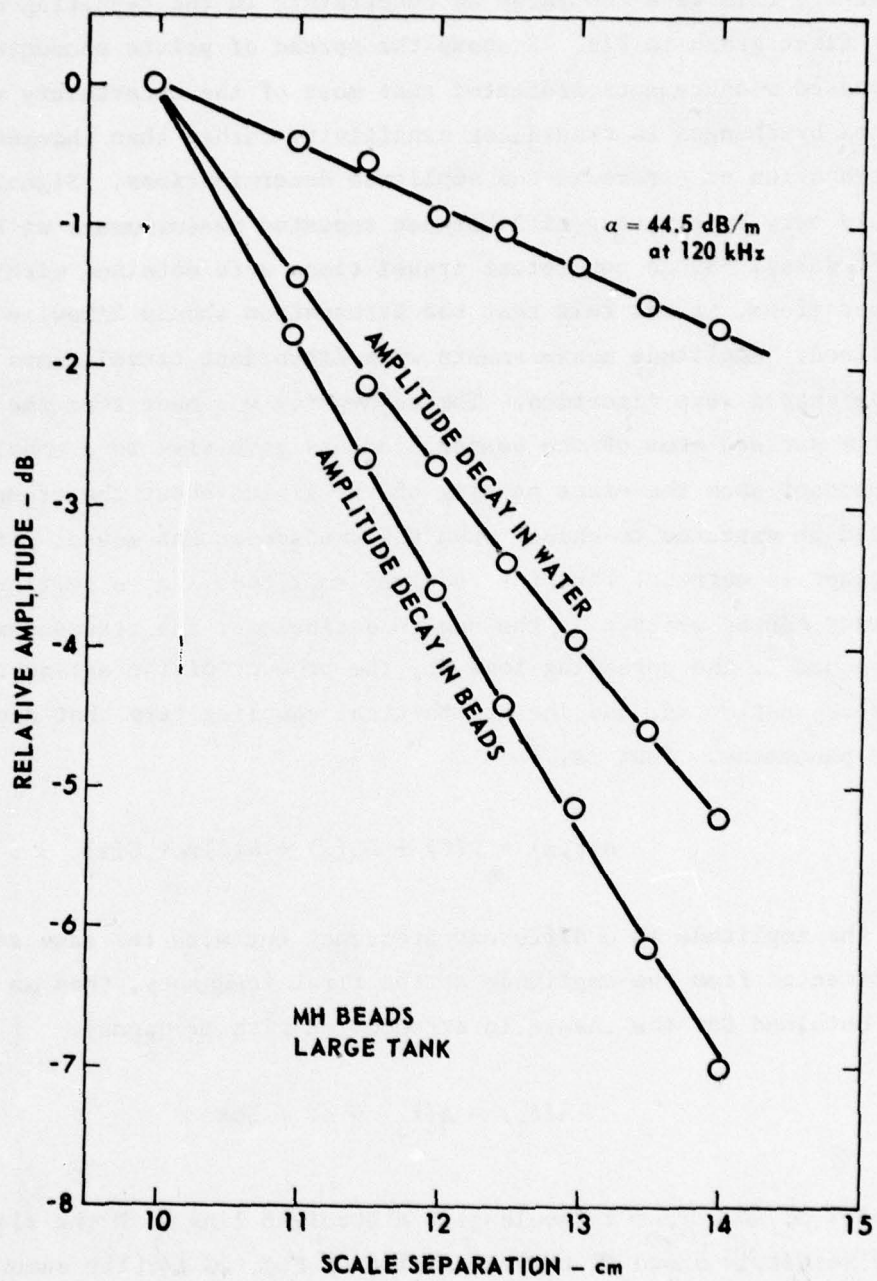


FIGURE 21
DETERMINATION OF COMPRESSIONAL WAVE ATTENUATION

ARL:UT
AS-79-211
DWB-GA
2-7-79

however, this gave too large an uncertainty in the resulting calculation. The first graph in Fig. 22 shows the spread of points encountered. Repeated measurements indicated that most of the uncertainty was introduced by changes in transducer sensitivity rather than changes in attenuation or errors in the amplitude determinations. Signal amplitudes could vary by a factor of 2 between repeated measurements with the same time delay. Since consistent travel times were obtained with increased separations, it was felt that the attenuation should likewise be well defined. Amplitude measurements with discordant travel times or distorted wave shapes were discarded. The assumption was made that the relatively large surface area of the bender elements gave rise to a coupling factor dependent upon the exact packing of the grains about the transducer that could be expected to change when the transducer was moved. If this concept is correct, then the received amplitude A at a particular frequency can be written as the sum in decibels of the transducer frequency response T , the spreading loss SL , the product of the attenuation and the separation αx , and the hypothetical coupling term that depends on the placement. That is,

$$A(f,x) = T(f) + SL(x) + \alpha(f)x + C(x) \quad . \quad (8)$$

If the amplitude at a different frequency but with the same separation is subtracted from the amplitude at the first frequency, then an expression is obtained for the change in attenuation with frequency.

$$A(f_1) - A(f_2) = \Delta T + \Delta \alpha x \quad . \quad (9)$$

A plot of ΔA versus x should give a straight line with the slope $\Delta \alpha$. The result is shown in the right plot of Fig. 22 for the same data as plotted on the left. This supports the assumption of a change in amplitude with separation that is independent of frequency and has the further advantage of eliminating some of the uncertainty in the spreading loss term.

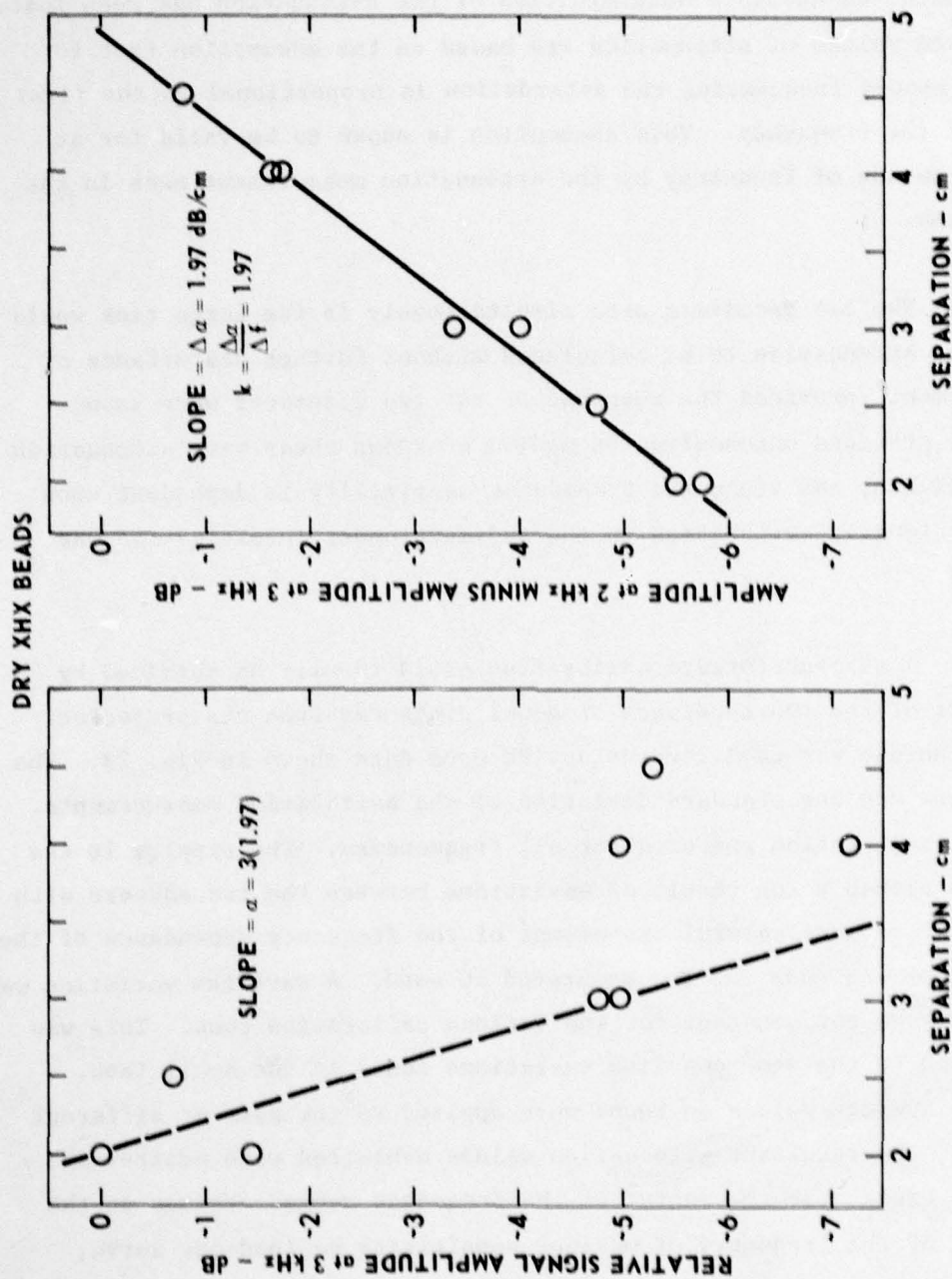


FIGURE 22
 DETERMINATION OF SHEAR WAVE ATTENUATION FACTOR - $k = \frac{\Delta a}{\Delta f}$

ARL:UT
 AS-79-212
 DWB-GA
 2-7-79

Although the above analysis yields a less equivocal interpretation of the data, an absolute determination of the attenuation has been lost. The quoted values of attenuation are based on the assumption that for closely spaced frequencies the attenuation is proportional to the first power of the frequency. This assumption is shown to be valid for at least a decade of frequency by the attenuation measurement made in the large tank.

The two receivers used simultaneously in the large tank would allow the attenuation to be calculated without further disturbance of the sediment, provided the response of the two receivers were known. Since no standard unconsolidated medium of known shear wave attenuation was available, and since the transducer sensitivity is dependent upon the wave length, calibration in the sediment under investigation was required.

A straightforward calibration could ideally be obtained by placement of the two receivers at equal distances from the projector. This technique was used for the dry PC sand data shown in Fig. 23. The error bars are one standard deviation of the calibration measurements. A single calibration was used for all frequencies. The ripples in the data are probably the result of variations between the transducers with frequency. A more careful assessment of the frequency dependence of the calibration was made for the saturated PC sand. A wavelike variation was found but was not constant for the various calibration runs. This was attributed to the same coupling variations found in the small tank. When the average values so found were applied to the data at different spacings, the resultant attenuation values exhibited wide scatter and a definite break near the center of the frequency range. Values on the low side of the frequency of maximum sensitivity defined one curve; values on the high side defined another. In an effort to extract the best possible results from the data, a method to determine the change of attenuation with frequency, similar to that applied to the single receiver data in the small tank, was applied.

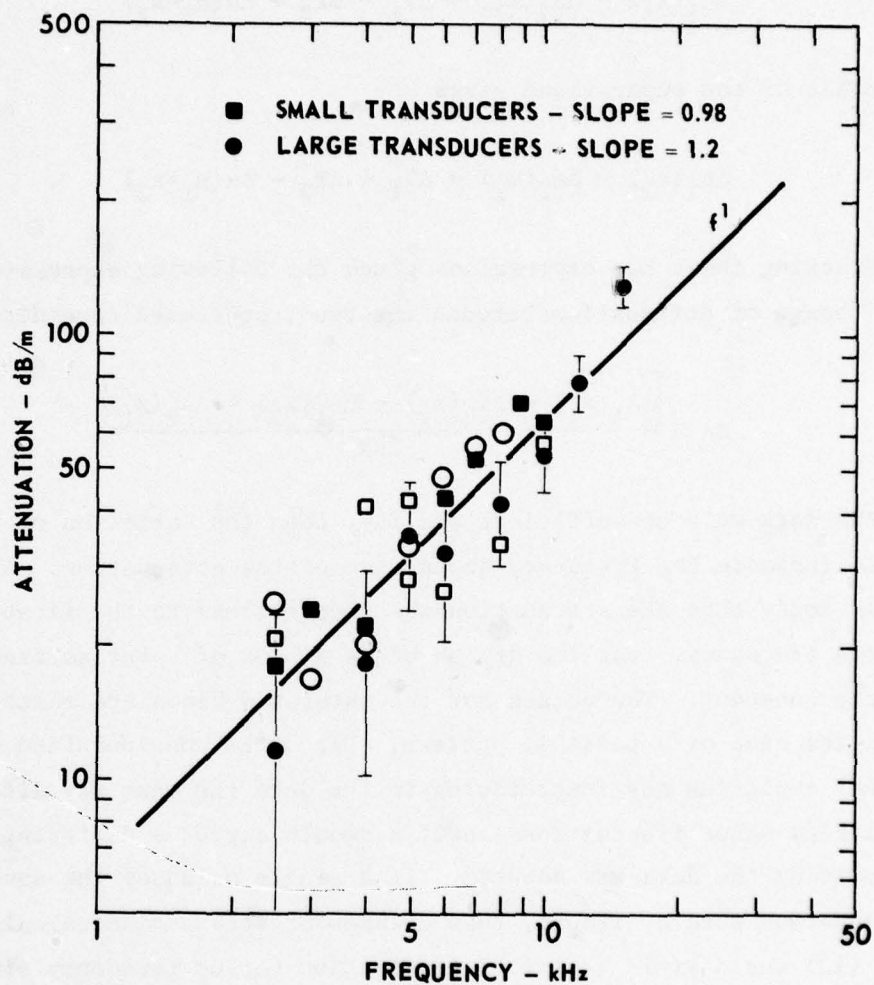


FIGURE 23
SHEAR WAVE ATTENUATION versus FREQUENCY
DRY PC SAND

ARL:UT
AS-79-213
DWB-GA
2-7-79

With the amplitude of a single transducer expressed by Eq. (9), the combination of two receivers gives

$$\Delta A_1(x_1) - \Delta A_2(x_2) = \Delta T_1 - \Delta T_2 + \Delta \alpha(x_1 - x_2) \quad . \quad (10)$$

Reversal of the separations gives

$$\Delta A_1(x_2) - \Delta A_2(x_1) = \Delta T_1 - \Delta T_2 - \Delta \alpha(x_1 - x_2) \quad . \quad (11)$$

Subtracting these two expressions gives the following expression for the change of attenuation between the two frequencies considered.

$$\Delta \alpha = \frac{[\Delta A_1(x_1) - \Delta A_2(x_2) - \Delta A_1(x_2) + \Delta A_2(x_1)]}{2\Delta x} \quad . \quad (12)$$

If the data were of sufficient quality, then the variation of $k = \Delta \alpha / \Delta f$ would indicate the frequency dependence of the attenuation. A constant k would imply that the attenuation was proportional to the first power of the frequency. For the dry MH beads a plot of k versus frequency is fairly constant. The values for the saturated beads are scattered but give the hint of a possible pattern. Since the consideration of k in this manner amplifies any inaccuracies in the data the same way differentiation amplifies minor fluctuations about a smooth curve, a different means of presenting the data was adopted. If a single value of the absolute attenuation were available, then changes of attenuation calculated from Eq. (12) would yield a plot of attenuation versus frequency similar to Fig. 23. A reference value of attenuation was chosen from the equation $\alpha = kf$ for a frequency pair whose calculated value of k matched the average k of all such pairs. The results are shown in Figs. 24, 25, and 26. Each point on these graphs was determined from eight separate amplitude measurements in accordance with Eq. (12). Confidence limits for the curves are hard to assess, particularly in terms of absolute values. However, the results were repeatable for both sizes of transducers and should therefore represent a fair picture of the true variation of attenuation with frequency.

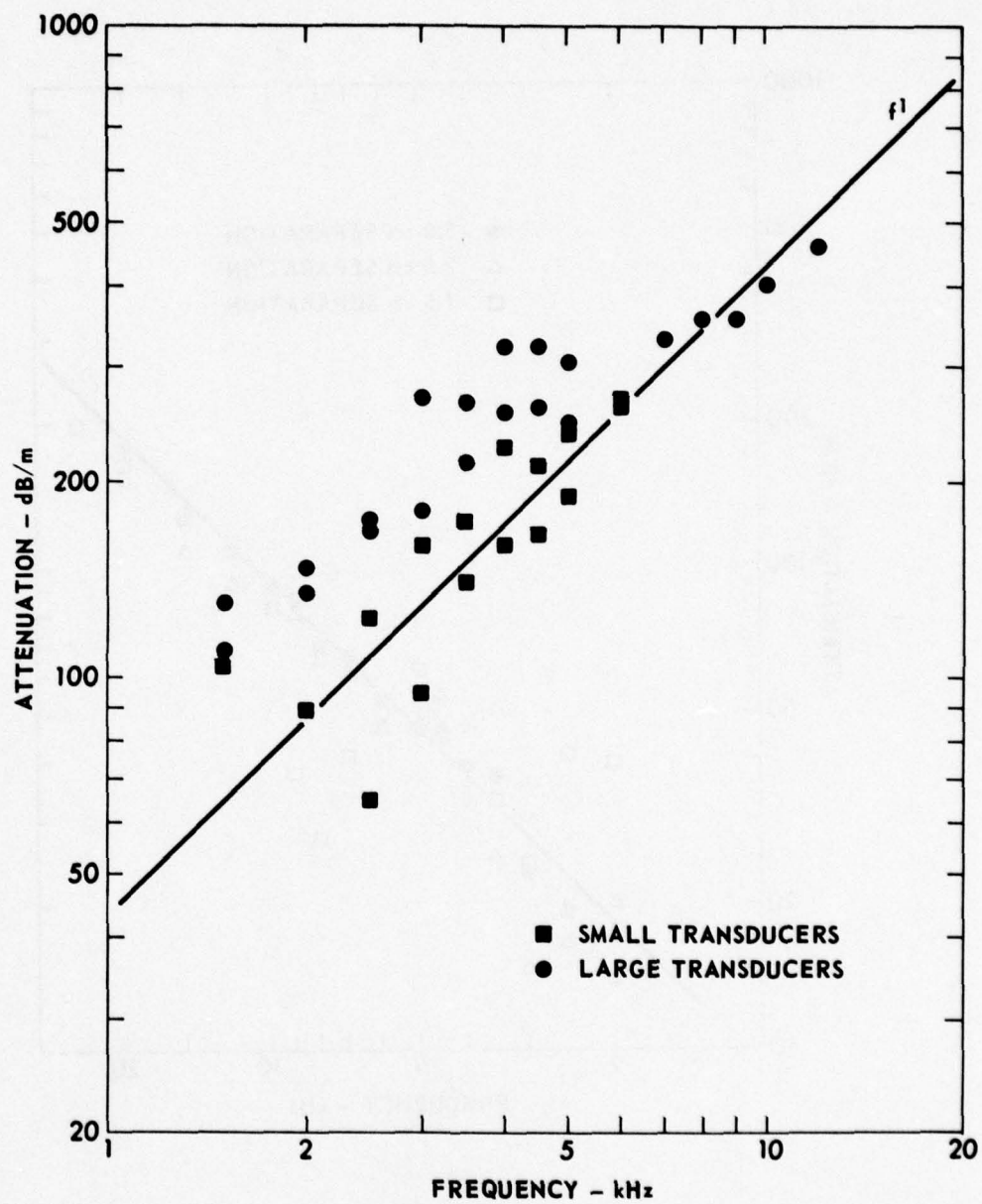


FIGURE 24
SHEAR WAVE ATTENUATION versus FREQUENCY
SATURATED PC SAND

ARL:UT
AS-79-272
DWB-GA
2-20-79

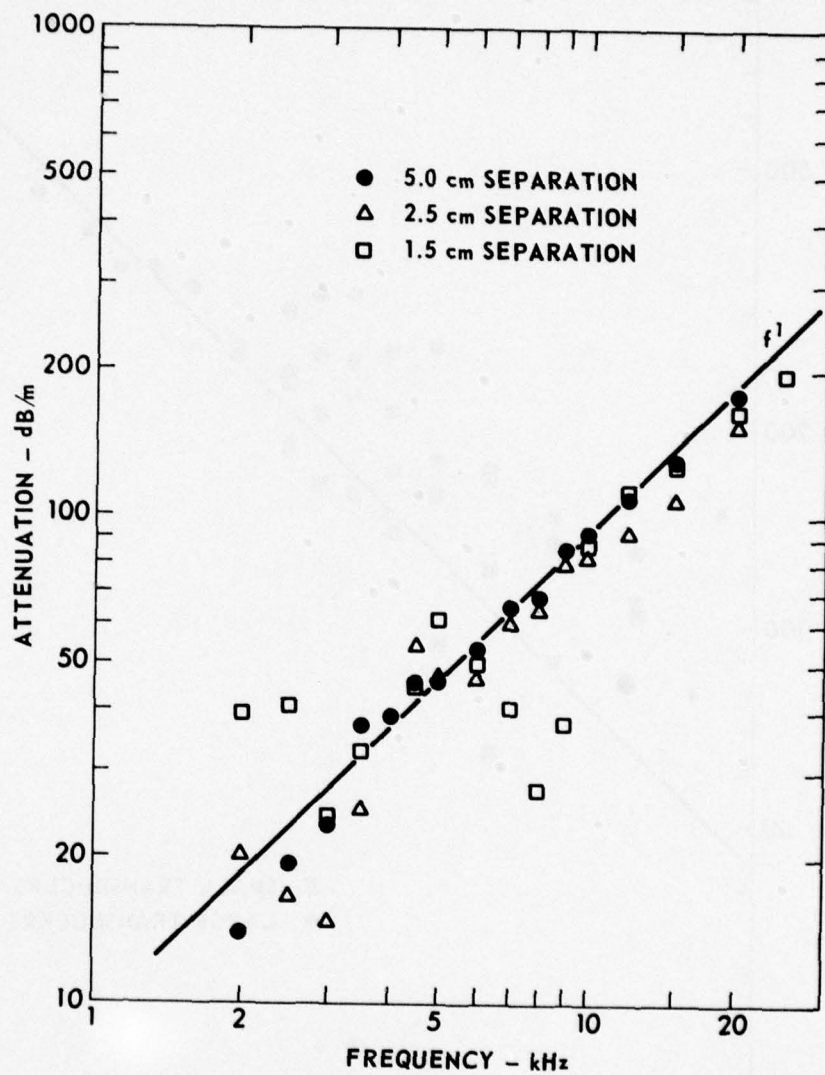


FIGURE 25
SHEAR WAVE ATTENUATION versus FREQUENCY
DRY MH BEADS

ARL:UT
AS-79-214
DWB-GA
2-7-79

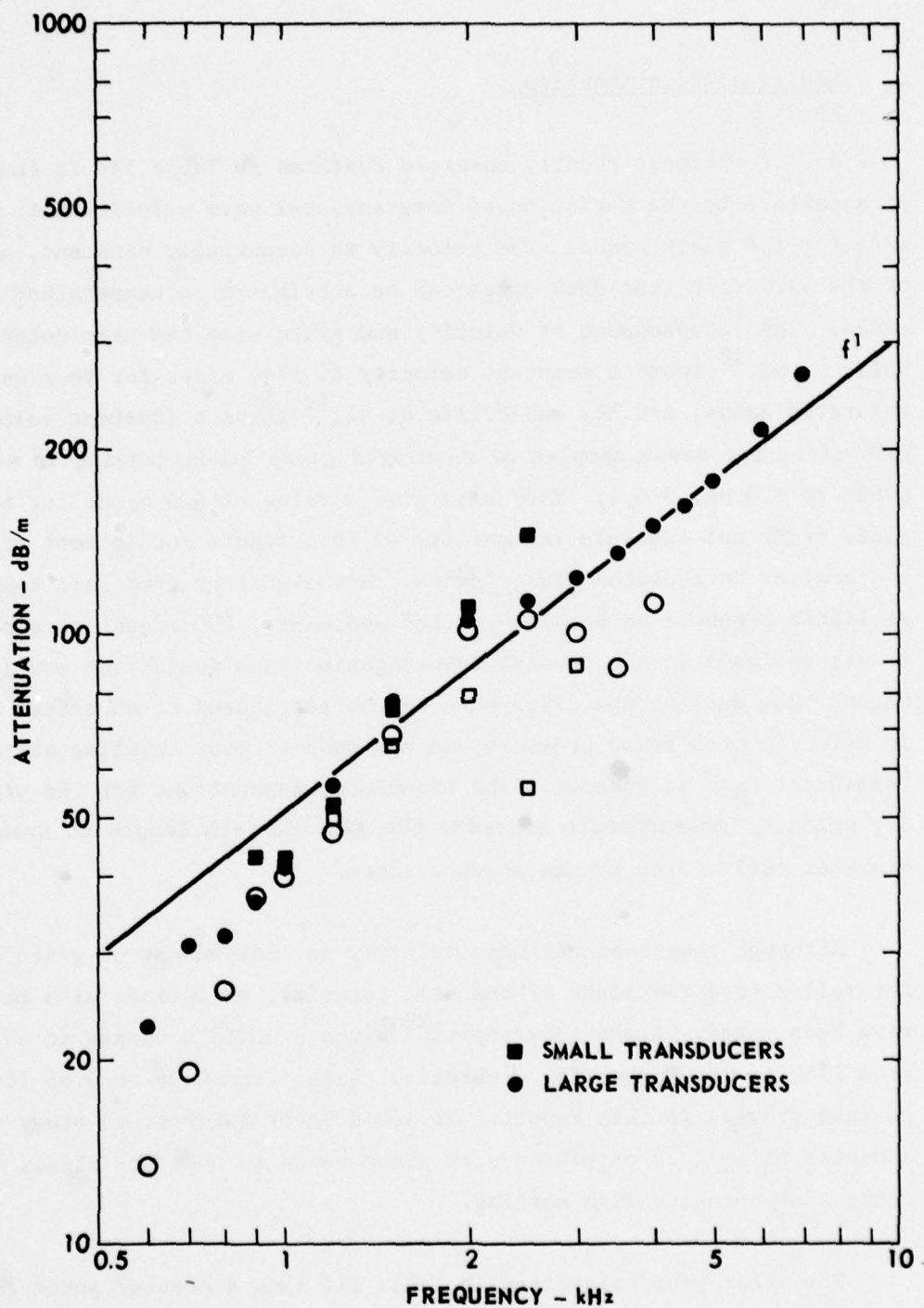


FIGURE 26
SHEAR WAVE ATTENUATION versus FREQUENCY
SATURATED MH BEADS

ARL:UT
AS-79-273
DWB-GA
2-20-79

D. Empirical Relationships

One of the most readily observed features in Table III is the lack of a pattern to the variation of compressional wave velocity with grain size for the glass beads. The velocity is essentially constant, and some of the variation that does exist can be attributed to temperature differences. The independence of velocity and grain size has been noted before. Nolle et al.¹⁸ found a constant velocity of 1740 m/sec for four well-sorted, saturated sands, $\beta=0.36$, and Wyllie et al.¹⁹ found a constant velocity of 1850 m/sec for seven samples of saturated glass beads ranging in size from 0.028 to 6.0 mm, $\beta=0.4$. They also give a value of 400 m/sec for the dry glass beads but disclaim reliability of this figure due to poor arrivals and scatter in repeated measurements. Although they took care to apply as little pressure as possible to the sediments, 400 m/sec corresponds to values found in the present investigation when compaction was just begun. How much of the difference can be attributed to an actual change in velocity with frame pressure and how much to poor coupling at the transducer face is unknown. The transducer separations for the present dry velocity measurements exceeded the minimum path length to transducer diameter ratio noted by the above authors.

Although compressional wave velocity is independent of grain size for well-sorted sediments of the same porosity, variations with packing have been found. A previous report²⁰ gives a uniform change in velocity from 1750 to 1680 m/sec for a porosity change from 0.38 to 0.45 for the PC sand studied in this report. It would be of interest to study the acoustic parameters of mixtures of glass beads to note the effect of changes of porosity with sorting.

The shear wave velocities in Table III show a greater percentage variation among the different bead samples than do the compressional wave velocities. However, the variations show no trends with either grain size or porosity. The dry sediment velocities follow the same pattern but at higher absolute values. An increase in shear wave velocity between brine and air saturated samples of Ottawa sand and glass beads

has been reported by Domenico²¹ for values of external confining pressure from $2.8 \times 10^6 \text{ N/m}^2$ to $3.5 \times 10^7 \text{ N/m}^2$. Hardin and Richart²² found the same result in a resonant column experiment with different grain size distributions of Ottawa sand and crushed quartz sand. They also found the shear wave velocity at a given confining pressure to be unaffected by grain size except through its effect on porosity.

It is difficult to compare the shear wave velocities in Table III with velocities observed by other investigators in similar materials because of the pronounced effect of pressure differences. Domenico²¹ and Hardin and Richart²² indicate that shear wave velocity is proportional to the $1/4$ power of differential pressure for both dry and saturated unconsolidated materials. Hamilton²³ found a similar variation with depth for 29 in situ measurements of shear wave velocities in sands to 12 m. No attempt to confirm this dependence was attempted in the present report. The small and large tank results are listed separately so that measurements at different overburden pressures are distinct. Notice that an increase in depth from 9 to 20 cm gave a 50% increase in shear velocity for the PC sand and MH beads.

The compressional wave results for the saturated glass beads in Table III show an increase in energy loss for decreasing grain size. Values in the literature indicate that compressional wave attenuation in natural sediments increases with decreasing grain size, peaks at a mean grain size of approximately 54, and then decreases as grain size continues to decrease. Hamilton²⁴ presents a summary of attenuation data in the form of two curves, one versus grain size and one versus porosity. Both have the same general shape. However, since attenuation varies with grain size at constant porosity, as shown here, and also varies with porosity at constant grain size, as shown in a previous report,⁵ the two parameters should not be considered separately unless natural depositional processes are such that a specific porosity can be associated with a definite grain size. Figure 27 shows the present data

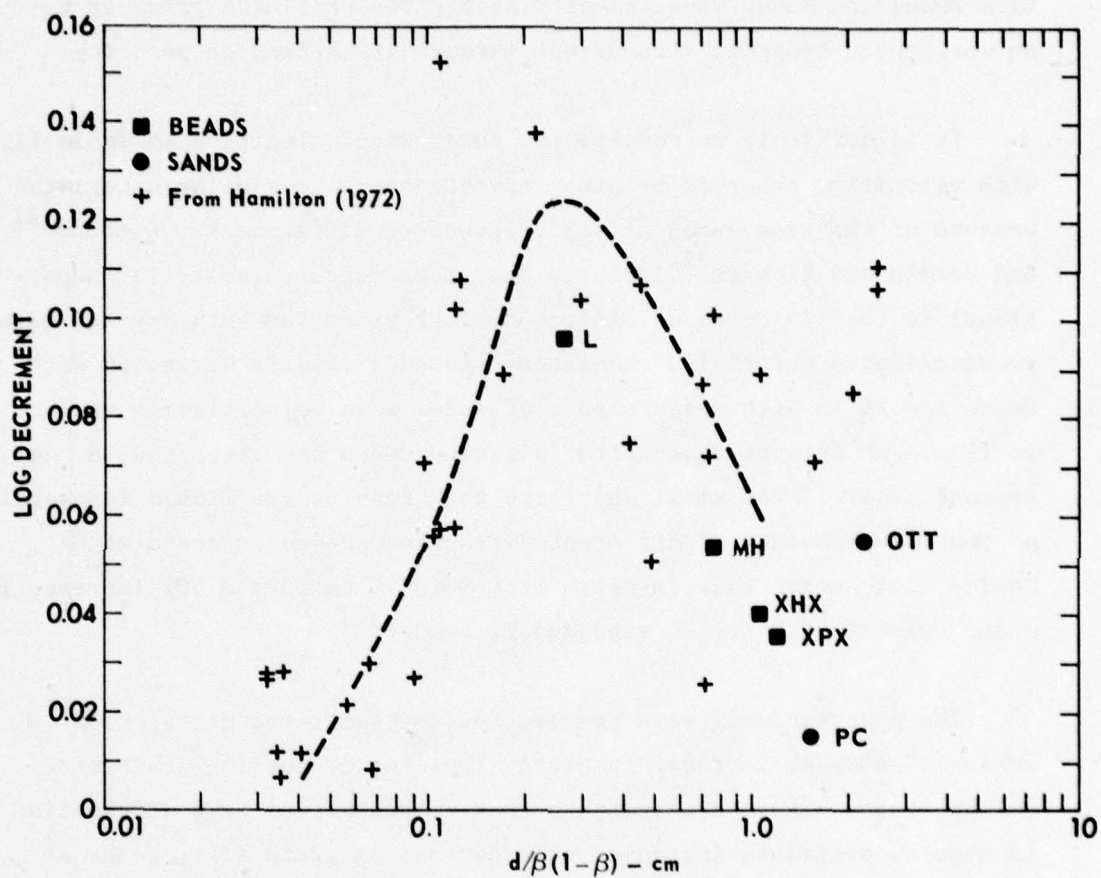


FIGURE 27
VARIATION OF COMPRESSIONAL WAVE ATTENUATION
WITH GRAIN SIZE AND POROSITY

ARL:UT
AS-79-215
DWB-GA
2-7-79

along with the values summarized by Hamilton. A theory that predicts the effect of grain size and porosity on the compressional wave attenuation must assume a definite mechanism for the energy loss. A satisfactory theory is lacking. Korvin²⁵ presents a theory based on perturbations caused by random inhomogeneities. His formulation includes the grain size and porosity as parameters and correctly predicts the behavior displayed in Fig. 27. Other predictions by his theory, however, are unsubstantiated for unconsolidated materials.

The values obtained for the compressional wave attenuations in the saturated sediments studied here compare well with values in the literature. The decrements given for the dry materials, however, are of doubtful significance. The problems associated with their determination were discussed earlier. Values in the literature are much smaller; however, these are obtained from resonant column experiments on jacketed materials subjected to confining pressures and are difficult to extrapolate to the present experimental conditions. Gardner et al.²⁶ report that decrements obtained from such experiments are approximately the same for both extensional and torsional vibrations.

A slight decrease in shear wave attenuation with increasing grain size is indicated by the data for the saturated glass beads. Decrements for all samples range from 0.3 to 2. Hamilton,²⁷ in a review of available shear wave data, found that decrements for natural water saturated sands and silts were mostly between 0.1 and 0.6. He further suggested that values for sand could be approximated by 0.30 ± 0.15 . Of the nine values in the present report, five fall within this range, while four are substantially larger. However, Hamilton was forced to draw conclusions from very sparse data, some of which included values at pressures or depths different from those encountered here.

Hall and Richart²⁸ found that saturated samples of Ottawa sand and glass beads had higher shear damping rates than the corresponding dry material. They measured damping by the amplitude decay of a vibrating

column of sediment packed in a rubber sleeve, and found that damping tends to decrease with an increase of confining pressure. Decrement values in the present study for the sands in the small tank and the sand and bead specimens in the large tank show an increase in damping with water saturation. The four bead samples in the small tank, however, show the reverse behavior.

There have been theoretical efforts to relate ratios of compressional and shear wave velocity to ratios of the corresponding decrements. The resulting equations are of the form²⁷

$$\frac{\delta_s}{\delta_p} = \frac{KV_p^2}{V_s^2} \quad , \quad (13)$$

with predicted values of K cited as 0.75 or 0.50. Hamilton notes that available data indicate values of K in the range 0.02 to 0.2. The data in Table III yield $K=0.012 \pm 0.005$ for the beads and $K=0.05 \pm 0.03$ for the sands. On this basis, Eq. (13) is not a particularly accurate means of estimating shear attenuation.

E. Theoretical Considerations

The displacement of a damped harmonic oscillation is given by

$$U = e^{i(\omega t - \bar{\ell}x)} \quad , \quad (14)$$

where

$$\text{Real}(\bar{\ell}) = \ell = \frac{1}{\lambda} = \frac{\omega}{v}$$

$$\text{Img}(\bar{\ell}) = \ell' = a \text{ (attenuation in nepers/unit distance).}$$

The elastic wave equation for shear waves, that is, displacements perpendicular to the direction of propagation, is

$$\frac{\mu \partial^2 U_y}{\partial x^2} = \rho \frac{\partial^2 U_y}{\partial t^2} \quad (15)$$

Substitution of Eq. (14) into Eq. (15) gives

$$\mu \bar{\lambda}^2 = \omega^2 \rho \quad , \quad (16)$$

which, in the absence of dissipation, yields the familiar expression for shear wave velocity in terms of the shear modulus and the density:

$$V^2 = \frac{\mu}{\rho} \quad (17)$$

However, if Eq. (16) is applied for $\lambda_1 \neq 0$, then either μ or ρ or both must be considered as complex operators. If μ is arbitrarily assigned an imaginary component, then Eq. (16) implies

$$\mu = \rho V^2 \frac{(1-r^2)}{(1+r^2)^2} \quad , \text{ and} \quad (18)$$

$$\mu' = \rho V^2 \frac{2r}{(1+r^2)^2} \quad , \text{ and} \quad (19)$$

$$\delta = \frac{2\pi a V}{\omega(1-r^2)} \quad , \quad (20)$$

where $r = aV/\omega$. When the damping is small, $r^2 \ll 1$, and Eqs. (18) and (20) reduce to

$$V^2 = \frac{\mu}{\rho} \quad , \text{ and} \quad (21)$$

$$\delta = \frac{aV}{f} \quad . \quad (22)$$

Equation (21), which is independent of frequency, corresponds to the elastic expression for the velocity. Equation (22) yields a constant log decrement when a varies as the first power of frequency.

Similar conclusions can be obtained for compressional waves.²⁷ That is, for small damping, velocity dispersion is negligible and attenuation varies as the first power of frequency. Since these conclusions are supported by the available compressional wave data,²⁴ Hamilton has suggested that the above viscoelastic model be adopted for shear waves.²⁷

The data presented here support Hamilton's supposition although, as shown later, this is not the only model consistent with these data. The factor $(1-r^2)/(1+r^2)^2$ is 0.998 and 0.98 for the dry and saturated MH beads, respectively, in the large tank and is 0.998 and 0.96 for the dry and saturated PC sand. Variations in the velocity measurements over a decade of frequency were less than 5 m/sec, which is within the expected experimental error. A first power variation of attenuation with frequency is a reasonable fit to the attenuation data shown in Figs. 23 through 26.

Although the adoption of a complex shear modulus in Eq. (16) appears to predict the correct frequency dependence of the velocity and attenuation, no procedure exists for calculating the real and imaginary parts of the rigidity apart from independent measurements of velocity and attenuation. Since no physical mechanism has been specified, it is impossible to predict the effect of physical parameters, such as grain size or porosity, without the accumulation of large quantities of data from which empirical relations can be derived.

Since marine sediments are grossly two-phase systems (fluid and grains), it is of interest to investigate the effect of fluid saturation. Gassman²⁹ derived expressions relating the elastic moduli of the bulk sediment to those of the sediment grains, the pore fluid, and the sediment frame. Since water has vanishing rigidity, Gassman concluded that

$$\mu(\text{bulk}) = \mu(\text{frame}) \quad . \quad (23)$$

For small damping, application of Eq. (19) to Eqs. (21) and (22) implies

$$V^2(\text{bulk}) = \frac{V^2(\text{frame})\rho(\text{frame})}{\rho(\text{bulk})} \quad , \quad (24)$$

and

$$\delta(\text{bulk}) = \frac{V(\text{bulk})}{V(\text{frame})} \delta(\text{frame}) \quad . \quad (25)$$

Equation (24) states that the bulk shear velocity is less than that of the frame in proportion to the square root of the ratio of the densities. Since dissipation has been introduced only through the imaginary part of the shear modulus, which, for the moment, is assumed equal for both the frame and the bulk sediment, the attenuation in each case is the same. This leads to Eq. (25) which states that the bulk log decrement is less than that of the frame.

To test the predictions of Eqs. (24) and (25), values of the frame velocity and decrement are required. It is often assumed in laboratory studies that values obtained from the dry sediment can be used to approximate the frame parameters.^{21,26,30} This is probably a reasonable assumption for consolidated sediments with a fixed frame, although the possibility still exists that addition of the fluid can alter the physical process responsible for frame dissipation. For example, if energy loss in the dry material is due to frictional forces at the grain boundaries, then fluid lubrication could change the grain-to-grain interaction.³¹ For unconsolidated materials, greater care must be exercised if the frame parameters are to be estimated by the dry sediment values. Experimental conditions must be such that the same packing is produced for both the dry and the saturated materials. That is, a specific porosity and stress state must be reproducible. This is not too difficult for the sand size particles investigated here. Control of compaction for dry silt and clay particles, however, would be extremely difficult. Additionally, since natural clays are cohesive, saturation affects the structure of the material. Thus, while the concept of a frame modulus as envisioned

by Gassman may still be applied to finer sediments, its value is difficult to obtain independent of its defining equation.

The shear wave velocities in Table III show a decrease with fluid saturation as predicted. However, in every case, the decrease is greater than that implied by the additional mass of the water. This may indicate a change in the frame values with saturation. The decrements for the dry materials divide into two groups. The glass beads in the small tank all gave higher attenuations when dry than when saturated. The beads in the large tank and all of the sands show an increase in attenuation with saturation. (The attenuation in the dry PC sand is slightly lower than that of the saturated sample even though the increase in velocity gives a larger log decrement.) The extreme sensitivity of the dry bead measurements in the small tank to very minor physical disturbances makes it unlikely that the measured values should be taken as the frame parameter values when the same beads are saturated. The angular sand grains are less subject to changes in the particle arrangement due to minor vibrations and are also less susceptible to static electric charges. Presumably, the increase in overburden pressure in the large tank imparts enough rigidity to the bead packing that the frame changes only slightly upon saturation. Data in the literature indicate an increase in attenuation with saturation.^{22,32}

If the attenuation increases with saturation, then an additional loss mechanism due to the fluid is implied. An obvious possibility is viscous drag caused by the relative movement of the frame and the pore fluid.

Equation (24) was obtained with the assumption that the entire mass of the fluid was perfectly coupled to the frame (Gassman's "closed system"). At acoustic frequencies, however, the possibility exists that a smaller portion of the fluid mass is coupled to the grains through viscous interaction. The $\rho(\text{bulk})$ in Eq. (24) should then be replaced by an "effective density" that depends on the frequency. If the coupling is less than perfect, then a smaller change between the frame and bulk

velocities is indicated than that predicted by Eq. (24). This has been observed by Domenico²¹ for pressurized sand and bead specimens.

Ament³³ obtained an equation for the effective density based on a simple consideration of viscous, incompressible flow. He found

$$\rho(\text{effective}) = \rho(\text{static}) + \frac{i\omega(K/\eta)(1-\beta)^2\beta\Delta^2}{\beta - i\omega(K/\eta)(1-\beta)(\rho_f + \beta\Delta)} \quad (26)$$

where K is the absolute permeability, η is the fluid viscosity, β is the porosity, and $\Delta = \rho_g - \rho_f$ is the difference between the grain and fluid densities.

The imaginary part of Eq. (26) will introduce an additional attenuation due to the relative movement that at first increases as the square of the frequency and then becomes almost constant (Fig. 28). In order for the permeability measured at steady flow rates to be appropriate, Ament states that the frequency should be less than approximately

$$\omega = \frac{2\eta}{\rho_f a^2} \quad (27)$$

where a is the pore "size". Since the frequencies used in the present study are above this limit, a frequency correction to the fluid flow is required.

Biot,³⁴ in a detailed study of relative frame-fluid movement caused by acoustic stress, obtained an expression similar to Eq. (27) for a frequency above which the assumption of Poiseuille flow is invalid. He derived a complex correction factor to the viscosity that allows consideration of higher frequencies. His result, in terms of zero order Kelvin functions, was

$$F(\kappa) = \frac{1}{4} \frac{\kappa T(\kappa)}{1 - \frac{2}{i\kappa} T(\kappa)} \quad (28)$$

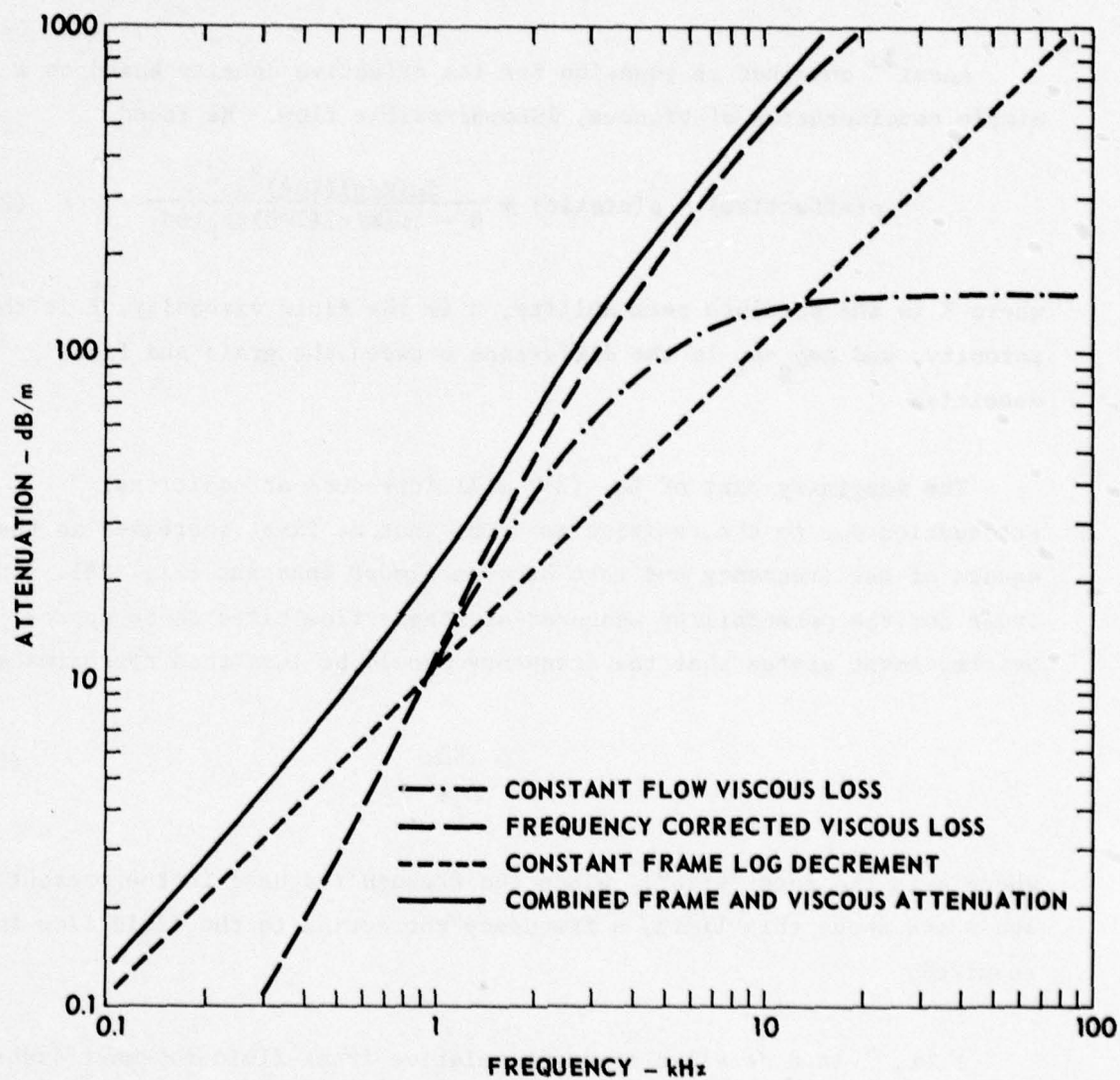


FIGURE 28
RELATIVE CONTRIBUTIONS OF THEORETICAL FRAME LOSS
AND VISCOUS DISSIPATION TO SHEAR WAVE ATTENUATION

ARL:UT
AS-79-268
DWB-GA
2-20-79

where

$$T(\kappa) = \frac{\text{ber}'(\kappa) + i\text{bei}'(\kappa)}{\text{ber}(\kappa) + i\text{bei}(\kappa)}, \quad (29)$$

and

$$\kappa = a(\omega \rho_f / \eta)^{1/2}. \quad (30)$$

The pore size a is, strictly speaking, the radius of a circular tube. However, Biot found that the analytic solution for flow between two infinite parallel plates gave essentially the same correction if a was adjusted by a scale factor. Thus a may be regarded as a pore size parameter that will vary with sinuosity and pore shape. Note, however, that a large variation in pore size is not allowed within a given sediment. The pore size parameter may be regarded as an empirical constant or, for well-sorted sediments, may be related³⁵ to the mean grain diameter through the Kozeny-Carman equation (Eq. (7)) by

$$a = \frac{d_m}{3} \frac{\beta}{(1-\beta)}. \quad (31)$$

Replacing the viscosity in Eq. (26) with $\eta F(\kappa)$ as defined in Eq. (28) results in a viscous loss term that increases as the square of the frequency at lower frequencies and as the square root of the frequency at high frequencies. (See Fig. 28.)

With both $\bar{\mu}$ and $\bar{\rho}$ regarded as complex, Eq. (16) gives

$$\ell^2 = \frac{\omega^2}{2} \frac{\rho\mu + \rho'\mu'}{\mu^2 + \mu'^2} \left[1 + \sqrt{1 + \left(\frac{\rho'\mu + \rho\mu'}{\rho\mu + \rho'\mu'} \right)^2} \right] \quad (32)$$

and

$$\ell'^2 = \frac{-\omega^2}{2} \frac{\rho\mu + \rho'\mu'}{\mu^2 + \mu'^2} \left[1 - \sqrt{1 + \left(\frac{\rho'\mu + \rho\mu'}{\rho\mu + \rho'\mu'} \right)^2} \right]. \quad (33)$$

If $\bar{\mu}$ is taken as an empirical complex constant determined by the frame, and $\bar{\rho}$ is Ament's effective density, i.e., Eq. (26) modified by Biot's frequency correction to the viscosity, then, with the appropriate choice of parameters, Eqs. (32) and (33) are equivalent to Stoll's^{36,37,38} application of Biot's theory for shear wave propagation in acoustic media. This is not unexpected since Geertsma and Smith³⁹ showed that Ament's equation can be derived from Biot's equations of motion. The only difference between Eqs. (32) and (33) and similar equations used by Stoll is the number of parameters which must be specified. Stoll's formulation includes not only the pore size parameter discussed above, but also an additional "structure constant."

The structure constant, in effect, adds an additional term to the effective density of Eq. (26) to account for the possibility of mass coupling between the frame and the fluid not due to viscous interaction, as would exist in isolated cavities oriented perpendicular to the pressure gradient.⁴⁰ Any significant contribution of this type would cause the intercept of Fig. 14 to deviate from the origin.⁴¹ For the highly permeable sediments considered in the present study, stagnant pockets of fluid can be neglected. This amounts to setting Stoll's structure constant to unity or Biot's mass coupling parameter, ρ_{12} , to zero. Slight variations of these parameters cause only minor changes in the shape of the resulting attenuation versus frequency curves.

Figure 28 illustrates the relative theoretical effects of the various alterations to the elastic solution of the shear wave equation of motion. The values are appropriate for the MH beads in the large tank. With $\bar{\rho}=\rho$ (dry), a constant log decrement for the frame, as implied by Fig. 24, yields a straight line with unity slope. With $\mu'=0$, the viscous loss for constant flow resistance obtained from Ament's effective density gives a constant attenuation at higher frequencies. Introduction of Biot's frequency correction to the viscosity causes the viscous loss at high frequencies to vary as the square root of the frequency. The total

predicted attenuation when all parameters in Eq. (33) are finite is the sum of the individual frame and viscous losses.

The transition region between the low frequency f^2 and the high frequency $f^{1/2}$ dependence of viscous attenuation on frequency depends critically on the physical permeability. Changes in the porosity of the pore size parameter independent of their influence on the permeability cause only minor changes in the overall shape of the curve. Stoll and Bryan³⁸ present a comprehensive series of curves illustrating the separate effects of the various parameters on predicted compressional wave attenuation. Curves obtained from Eq. (33) for shear waves are similar.

Figures 29 and 30 compare the attenuation predicted by Eq. (33) with the experimental data shown in earlier figures. The frame parameters are taken from the dry sediment measurements and the pore size parameter is obtained from Eq. (31). The predicted increase in attenuation due to viscous loss is in general agreement with the data for both the MH beads and the PC sand. The predicted dispersion in each case is less than the experimental error in the velocity measurements. However, the predicted velocities are slightly higher than those actually measured. Minor adjustments in the various input parameter values can result in better agreement.

There is insufficient data in this report, or in the literature, to assess the detailed influence of viscous loss on overall sediment attenuation. Figures 29 and 30 indicate, however, that additional measurements are needed before values of shear wave attenuation at a single frequency can be confidently extrapolated to frequencies several decades removed on the basis of a simple first power model.

The sediments in this report were specially chosen such that the expected viscous loss would be comparable to dissipation in the frame. This may seldom be the case in natural marine sediments. The frame loss is expected to dominate in low permeability sediments such as silts

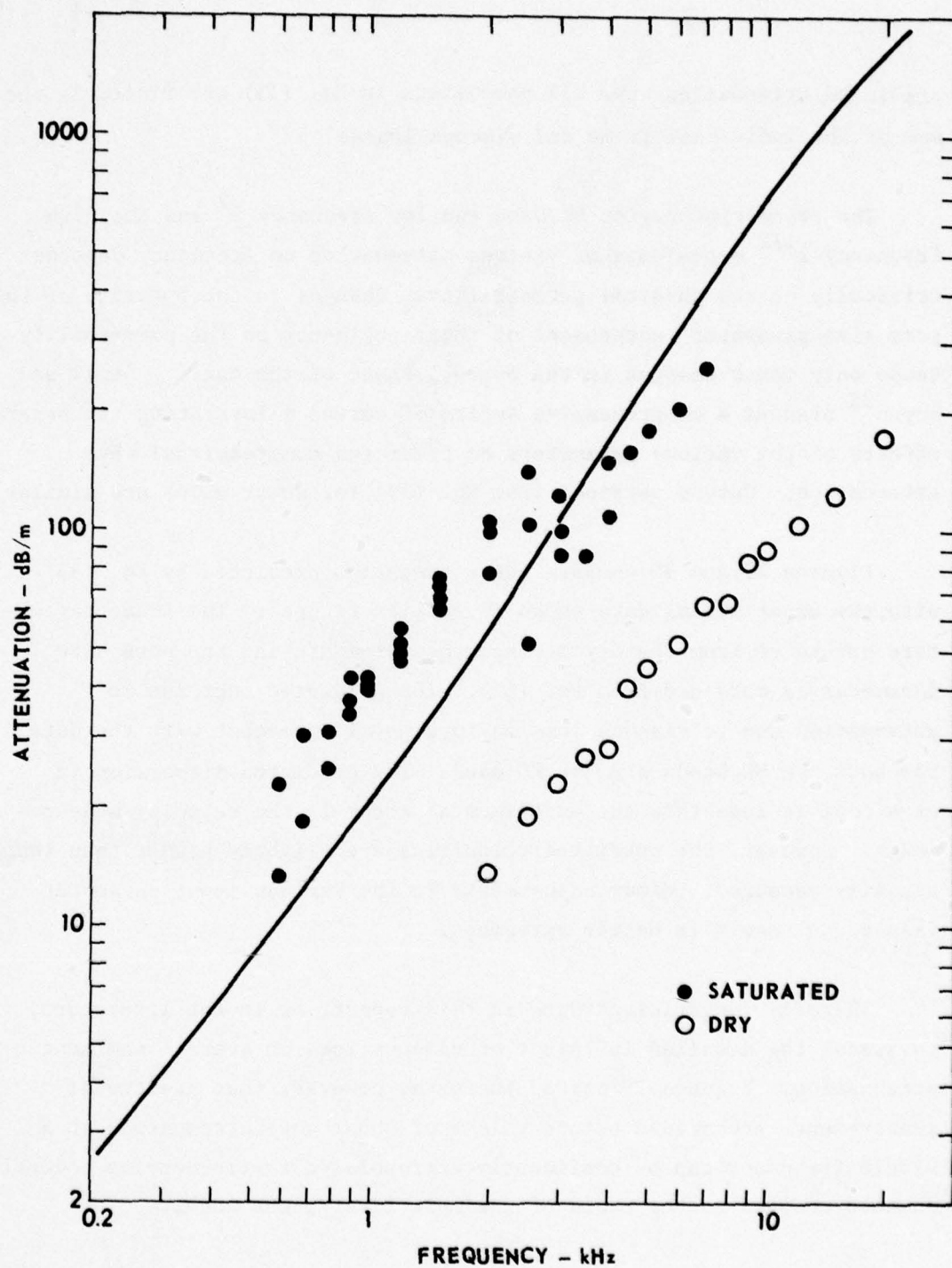


FIGURE 29
SHEAR WAVE ATTENUATION COMPARED WITH
PREDICTED VISCOUS LOSS - MH BEADS

ARL:UT
AS-79-269
DWB-GA
2-20-79

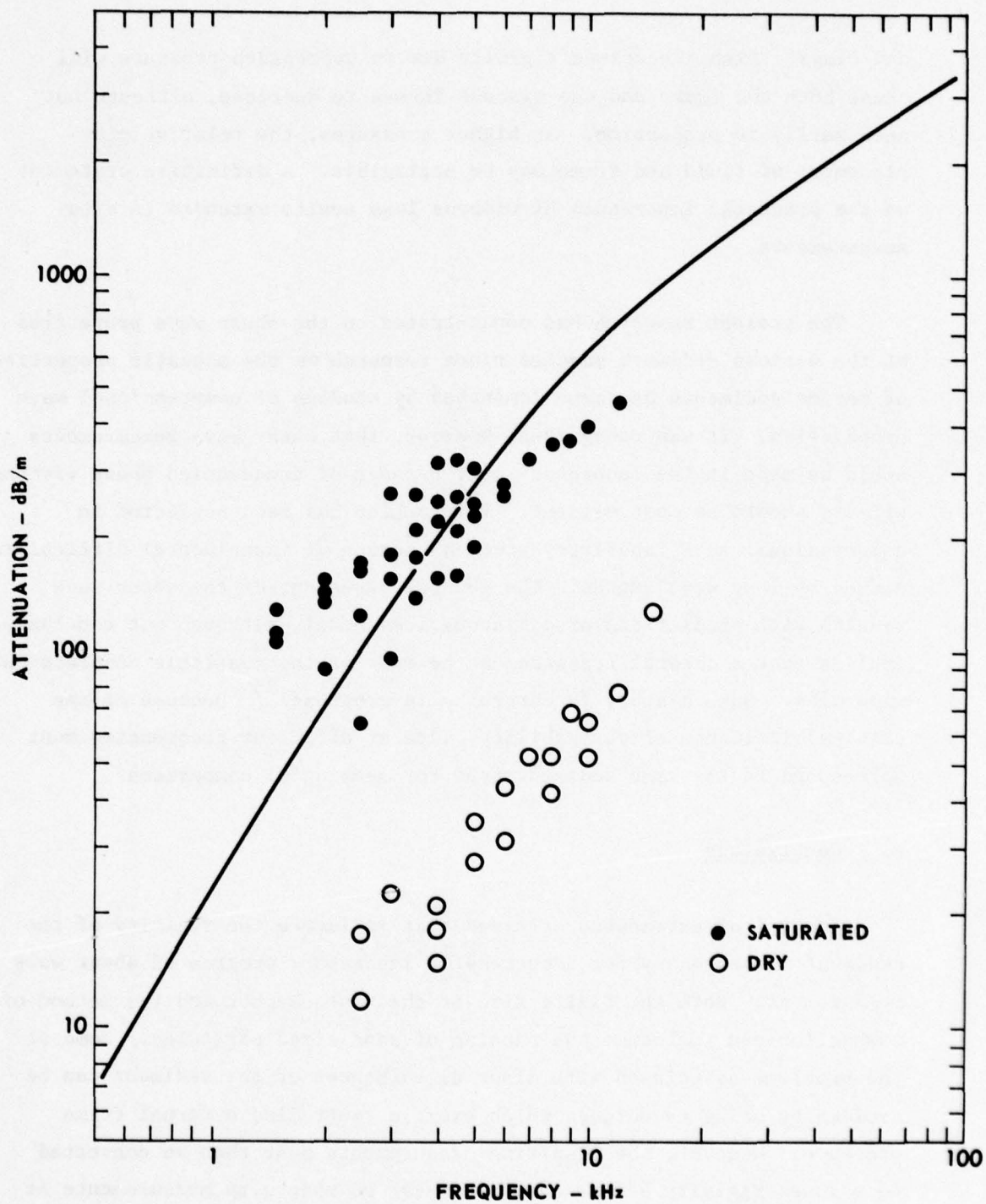


FIGURE 30
SHEAR WAVE ATTENUATION COMPARED WITH
PREDICTED VISCOUS LOSS - PC SAND

ARL:UT
AS-79-271
DWB-GA
2-20-79

and clays. Also, increased rigidity due to overburden pressure will cause both the frame and the viscous losses to decrease, although not necessarily in proportion. At higher pressures, the relative displacement of fluid and frame may be negligible. A definitive statement on the practical importance of viscous loss awaits extended in situ measurements.

The present research has concentrated on the shear wave properties of the various sediment samples since research on the acoustic properties of marine sediments has been dominated by studies of compressional wave propagation. It was recognized, however, that shear wave measurements could be made in the laboratory over a range of frequencies where viscous effects should be most evident. This region has been neglected in compressional wave laboratory studies because of experimental difficulties caused by long wavelengths. The general agreement of the shear wave results with predictions of a viscous loss model, although not conclusive, implies that a careful reassessment be made of the available compressional wave data. Such a study is currently in progress.³⁵ Because of the critical influence of permeability, data at different frequencies must correspond to the same sediment type for meaningful comparison.

F. Conclusions

Control of extraneous stresses that influence the rigidity of the sediment is necessary for a successful laboratory program of shear wave measurement. Both the finite size of the test chamber and the method of compaction can influence the packing of sand sized particles. Some of the problems associated with minor disturbances of the sediment can be avoided by using techniques which exert a controlled external frame pressure. However, the resulting measurements must then be converted to a lower rigidity before comparison can be made with measurements at surface pressures. The 150 liter sediment tank used in the present study represents a convenient size for laboratory measurements in sand. There is sufficient sediment mass to reduce the influence of minor

vibrations on the packing, and yet the mass is not too large to vibrate at amplitudes necessary to reach minimum porosity. The tank is also small enough to allow deaeration of the entire sediment at once. An irregular porous foam liner has been found to be an efficient absorber of shear wave energy. This allows interference from reflections to be minimized.

High quality shear wave signals can be generated and detected by bender elements in low rigidity unconsolidated sediments. The broadband characteristics of the transducers allow velocities and attenuations to be measured over more than a decade of frequency. Data in a natural sand and a sample of glass beads indicate that dispersion, if present, is less than approximately 5% between 0.5 and 20 kHz for both dry and saturated specimens. The shear wave velocity decreases with water saturation. The frequency dependence of the attenuation can be adequately approximated as proportional to the first power of the frequency over the range of the experiments. However, a theoretical model of viscous loss successfully predicts the observed order of magnitude change in attenuation between the dry and saturated samples. Since this theory predicts a variation in the log decrement with frequency, additional data are required before values of shear attenuation for highly permeable sediments can be confidently extrapolated over several decades. Continued refinement of the laboratory technique is recommended, as well as development of in situ capabilities.

V. DETERMINATION OF THE NONLINEARITY PARAMETER OF SATURATED SEDIMENTS BY IMPEDANCE MEASUREMENT

The nature and possible source of nonlinearity in saturated marine sediments has been the subject of a separate study.⁴² In conjunction with our work on developing techniques for measuring acoustic impedance, we have considered the possibility of determining the value of the nonlinearity parameter.

It is postulated that the relationship between the excess pressure p and the particle velocity u of a finite amplitude plane wave is given by

$$p = \rho_0 c_0 u + \frac{\beta}{2} \rho_0 u^2 \quad (34)$$

$$p = \rho_0 c_0 u \left(1 + \frac{\beta}{2} \epsilon_0 \right) , \quad (35)$$

where $\beta = 1 + B/2A$ is the nonlinearity parameter, ρ_0 is the density, c_0 is the small signal sound speed, and $\epsilon_0 = u/c_0$ is the acoustic Mach number at the source. This relationship indicates that the nonlinearity parameter of a fluid can be determined by measuring the radiation impedance of a piston transducer as a function of particle velocity or as a function of driving power.

In principle this could be accomplished by driving a piston transducer with a sinusoidal signal of (angular) frequency ω_1 . Due to the nonlinear relationship there will also be generated a second harmonic signal of frequency ω_2 and the particle velocity will be of the form

$$u(t) = u_1 \cos \omega_1 t + u_2 \cos \omega_2 t , \quad (36)$$

where the amplitude of the second harmonic u_2 is much smaller than the amplitude of the first harmonic u_1 . From Eq. (34) the sound pressure is

$$p(t) = \rho_0 c_0 [u_1 \cos \omega_1 t + u_2 \cos \omega_2 t] + \frac{\beta}{2} \rho_0 \left[\frac{\mu_1^2}{2} + \frac{\mu_1^2}{2} \cos \omega_2 t + \mu_2^2 \cos \omega_2 t + \dots + \right]; \quad (37)$$

however, since $\mu_1 \gg \mu_2$, one obtains for the first and second harmonic pressure amplitudes, respectively,

$$p_1 \approx \rho_0 c_0 \mu_1 \quad (38)$$

$$p_2 = \frac{\beta}{4} \rho_0 \mu_1^2 = \frac{\beta}{4} \epsilon_0 p_1 \quad (39)$$

This suggests that one could measure the second harmonic pressure amplitude during the transmission of the fundamental signal and determine β by the use of Eq. (39).

Before discussing the particular arrangement of doing this, it is necessary to consider the approximate value of the ratio (p_2/p_1) .

Let it be assumed that the transducer is transmitting an intensity of 10 W/cm^2 . In a sandy sediment this will result in an acoustic Mach number $\epsilon_0 \approx 1.3 \times 10^{-4}$. In water $\beta \approx 4$; in saturated marine sediments the value is likely to be somewhat higher⁴² and one may assume the value $\beta = 10$. From Eq. (39) one therefore finds that $(p_2/p_1) \approx 3.25 \times 10^{-4}$, or expressed in decibels, $(p_2/p_1) = -70 \text{ dB}$. For other source levels, the ratio (p_2/p_1) will be as given by Fig. 31. It is clear that for all practical source levels the amplitude of the second harmonic will be very low and difficult to measure with any accuracy.

As a practical matter the design of the transducer must also be given some consideration. In order to transmit at a rather high power level, the transducer must be resonant at the fundamental frequency ω_1 . For a normal design this will result in a low sensitivity at the second

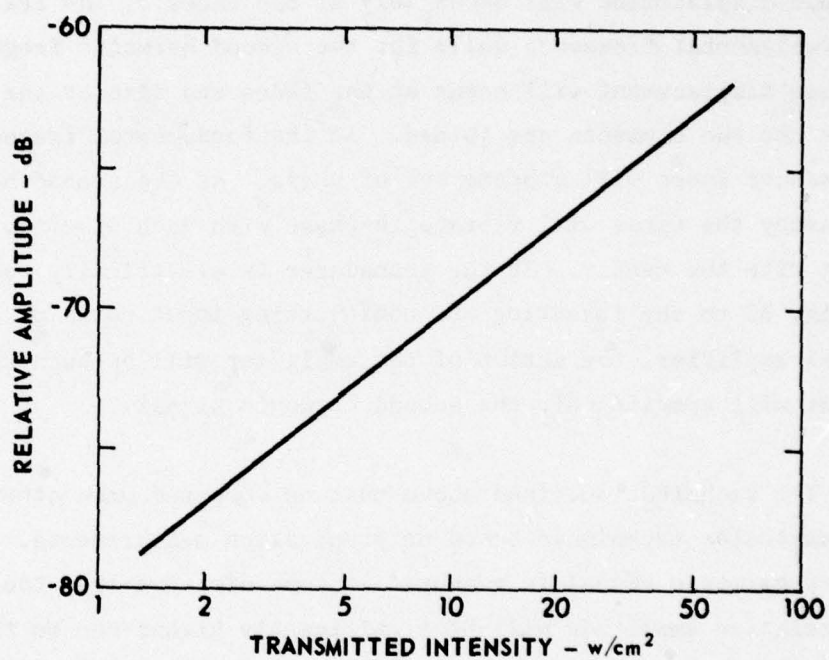


FIGURE 31
RELATIVE AMPLITUDE OF THE SECOND HARMONIC SIGNAL
AS A FUNCTION OF TRANSMITTED INTENSITY

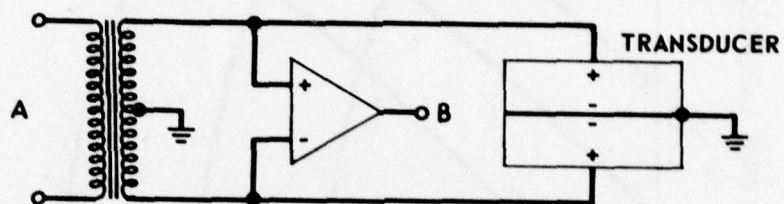
ARL:UT
AS-79-948
DJS - GA
5-11-79

harmonic frequency. This problem could be overcome by a double transducer as depicted in Fig. 32.

The transducer consists of two disks bonded together such that the direction of polarization of each disk is opposite to that of the other. Each disk has a thickness of one quarter-wavelength at the second harmonic frequency and the displacement amplitudes will be such that maximum displacement will occur only at the faces of the transducer for the fundamental frequency while for the second harmonic frequency maximum displacement will occur at the faces and also at the center where the two elements are joined. At the fundamental frequency, the transducer faces will vibrate out of phase. At the second harmonic frequency the faces will vibrate in phase with each other but out of phase with the center. If the transducer is electrically connected as in Fig. 32 to the inverting and noninverting input ports of an operational amplifier, the action of the amplifier will be such that its output will contain only the second harmonic signal.

The technique outlined above must be compared with other techniques, in particular techniques based on propagation measurements. If the second harmonic signal is measured at some distance from the projector, the relative amplitude will be significantly higher due to the cumulative effect of the distortion. Figure 33, from Ref. 38, shows the expected second harmonic level as a function of distance for a projected source intensity of 10 W/cm^2 and assuming plane waves in the whole interaction region. The maximum relative level in this case is more than 30 dB higher than the level at the source (Fig. 31). Propagation of spherical waves gives a lower second harmonic amplitude than plane waves but still the maximum relative level at some distance will be significantly higher than the level at the source.

Because the nonlinear impedance method and the arrangement of Fig. 32 have not yet been tried, the comparison cannot be conclusive at this point. Despite the fact that certain problems associated with the



TERMINAL A - TRANSMITTING FUNDAMENTAL SIGNAL
 TERMINAL B - RECEIVING SECOND HARMONIC SIGNAL

FIGURE 32
 TRANSDUCER ARRANGEMENT FOR NONLINEAR IMPEDANCE MEASUREMENT

ARL:UT
 AS-79-949
 DJS - GA
 5-11-79

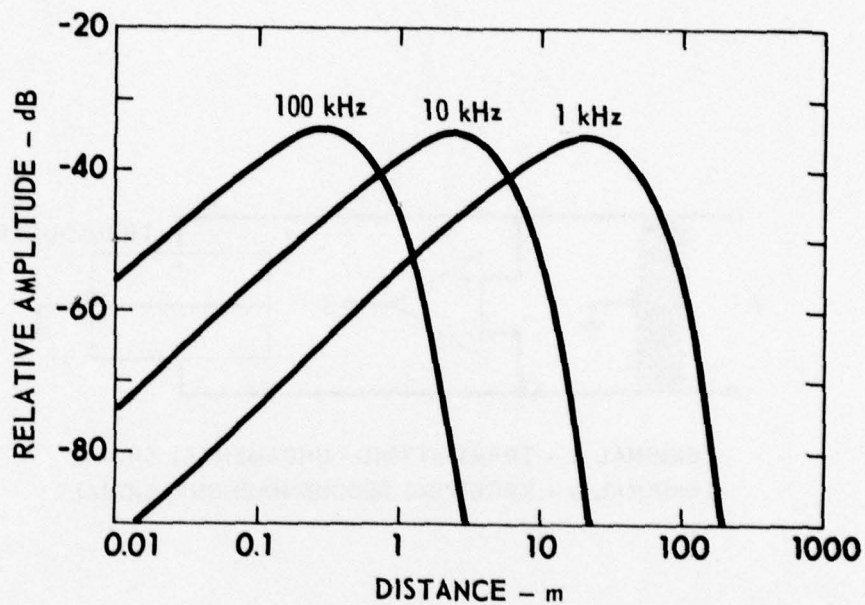


FIGURE 33
AMPLITUDE OF THE NONLINEARLY GENERATED
2nd-HARMONIC COMPONENT AS A FUNCTION
OF THE DISTANCE FROM THE TRANSDUCER
ASSUMING PLANE WAVES AND PROJECTED
INTENSITY OF 10 W/cm²

ARL:UT
 AS-79-140-P
 JMH - GA
 1- 22- 79

geometry of propagation can be avoided with the impedance method, it is believed that the propagation measurement of nonlinearly generated second harmonic signals will be the most accurate of the two methods considered here.

REFERENCES

1. "Status Report No. 1 under Texas A&M Research Foundation, P. O. No. RF-11743, and ONR Contract N00014-70-A-0166-0005," 1 January - 1 July 1971, (7 July 1971).
2. D. J. Shirley, A. L. Anderson and L. D. Hampton, "In Situ Measurement of Sediment Sound Speed During Coring," Applied Research Laboratories Technical Report No. 73-1 (ARL-TR-73-1), Applied Research Laboratories, The University of Texas at Austin, 14 March 1973.
3. D. J. Shirley and A. L. Anderson, "Compressional Wave Profilometer for Deep Water Measurements," Applied Research Laboratories Technical Report No. 74-51 (ARL-TR-74-51), Applied Research Laboratories, The University of Texas at Austin, 6 December 1974.
4. D. J. Shirley and A. L. Anderson, "Studies of Sediment Shear Waves, Acoustical Dependence, and Engineering Properties," Applied Research Laboratories Technical Report No. 75-23 (ARL-TR-75-23), Applied Research Laboratories, The University of Texas at Austin, 7 May 1975.
5. D. J. Shirley and D. W. Bell, "Acoustics of In Situ and Laboratory Sediments," Applied Research Laboratories Technical Report No. 78-36 (ARL-TR-78-36), Applied Research Laboratories, The University of Texas at Austin, 14 August 1979.
6. D. J. Shirley and L. D. Hampton, "Shear Wave Measurements in Laboratory Sediments," J. Acoust. Soc. Am. 63, 607 (1978).
7. D. J. Shirley, "Method for Measuring In Situ Acoustic Impedance of Marine Sediments," J. Acoust. Soc. Am. 62, 1028 (1977).
8. D. J. Shirley, "An Improved Shear Wave Transducer," J. Acoust. Soc. Am. 62, 1643 (1978).
9. R. D. Stoll, "A Dynamic Penetrometer for Investigating Sediment Properties," Proceedings of Civil Engineering in the Oceans-II, American Society of Civil Engineers, December 1969, pp. 209-220.
10. A. L. Inderbitzen, F. Simpson, and G. Gross, "A Comparison of In Situ and Laboratory Vane Shear Measurements," MTS Journal 5, 24-34 (1971).
11. T. J. Hirst, "Vertical Variability of Sediment Shear Strength," MTS Journal 7, 21-24 (1973).

12. A. L. Inderbitzen and F. Simpson, "A Study of the Strength Characteristics of Marine Sediments Utilizing a Submersible," Underwater Soil Sampling, Testing, and Construction Control, ASTM STP 501, American Society for Testing and Materials, 1972, pp. 204-215.
13. M. Perlow and A. F. Richards, "Geotechnical Variability Measured in Place from a Small Submersible," MTS Journal 7, 27-32 (1973).
14. A. F. Richards, V. J. McDonald, R. E. Olson, and G. H. Keller, "In Place Measurement of Deep Sea Soil Shear Strength," Underwater Soil Sampling, Testing, and Construction Control, ASTM STP 501, American Society for Testing and Materials, 1972, pp. 55-68.
15. R. F. Scott, "In-Place Measurement of the Strength of Ocean-Floor Soils by Accelerometer," Proceedings of Civil Engineering in the Oceans-I, American Society of Civil Engineers, December 1969, pp. 419-444.
16. P. C. Carman, Flow of Gases Through Porous Media (Academic Press, New York, 1956).
17. A. R. Gregory, "Some Aspects of Rock Physics from Laboratory and Log Data that are Important to Seismic Interpretations," Bureau of Economic Geology, The University of Texas at Austin, 1975 (unpublished paper).
18. A. W. Nolle, W. A. Hoyer, J. F. Mifsud, W. R. Runyan, and M. B. Ward, "Acoustical Properties of Water Filled Sands," J. Acoust. Soc. Am. 35, 1394-1408 (1963).
19. M. R. Wyllie, A. R. Gregory, and L. W. Gardner "Elastic Wave Velocity in Heterogeneous and Porous Media," Geophys. 21, 41-70 (1956).
20. D. J. Shirley, "Laboratory and In Situ Sediment Acoustics," Applied Research Laboratories Technical Report No. 77-46 (ARL-TR-77-46), Applied Research Laboratories, The University of Texas at Austin, Austin, 23 August 1977.
21. S. N. Domenico, "Elastic Properties of Unconsolidated Porous Sand Reservoirs," Geophys. 42, 1339-1368 (1977).
22. B. O. Hardin and F. E. Richart, Jr., "Elastic Wave Velocities in Granular Soils," J. Soil Mech. Found. Div. 39, SM1 (1963).
23. E. L. Hamilton, "Shear Wave Velocity versus Depth in Marine Sediments, A Review," Geophys. 41, 985-996 (1976).
24. E. L. Hamilton, "Compressional Wave Attenuation in Marine Sediments" Geophys. 37, 620-646 (1972).

25. G. Korvin, "Certain Problems of Seismic and Ultrasonic Wave Propagation in a Medium with Inhomogeneities of Random Distribution II. Wave Attenuation and Scattering on Random Inhomogeneities." Geophys. Trans. 24, S 2-Hungarian Geophys. Inst. Roland Eotvos, Budapest, 1977.
26. G. H. Gardner, M. R. Wyllie, and D. M. Droschak, "Effects of Pressure and Fluid Saturation on the Attenuation of Elastic Waves in Sands," J. Petrol. Tech. 16, 189-198 (1964).
27. E. L. Hamilton, "Attenuation of Shear Waves in Marine Sediments," J. Acoust. Soc. Am. 60, 334-338 (1976).
28. J. R. Hall and F. E. Richart, "Dissipation of Elastic Wave Energy in Granular Soils," J. Soil Mech. Found. Div. Proc. 895, M6 27-56, (1963).
29. F. Gassman, "Elastic Waves Through a Packing of Spheres," Geophys. 16, 673-685 (1951)
30. A. R. Gregory, "Fluid Saturation Effects on Dynamic Elastic Properties of Sedimentary Rocks," Geophys. 41, 895-921 (1976).
31. M. N. Toksoz, D. H. Johnston, and A. Timur, "Attenuation of Seismic Waves in Dry and Saturated Rocks, I and II," Geophys. 44, 681-688 (1979).
32. D. H. Johnston and M. N. Toksoz, "Ultrasonic P and S Wave Attenuation in Dry and Saturated Rocks Under Pressure, preprint.
33. W. S. Ament, "Sound Propagation in Gross Mixtures," J. Acoust. Soc. Am. 25, 638-641 (1953).
34. M. A. Biot, "Theory of Propagation of Elastic Waves in a Fluid Saturated Porous Solid, I and II," J. Acoust. Soc. Am. 28, 168-191 (1956).
35. J. M. Hovem and G. D. Ingram, "Viscous Attenuation of Sound in Saturated Sand," submitted for publication to The Journal of The Acoustical Society of America.
36. R. D. Stoll, "Acoustic Waves in Saturated Sediments" in Physics of Sound in Marine Sediments, edited by L. Hampton (Plenum Press, New York, 1974), pp. 19-39.
37. R. D. Stoll, "Acoustic Waves in Ocean Sediments" Geophys. 42, 715-725 (1977).
38. R. D. Stoll and G. M. Bryan, "Wave Attenuation in Saturated Sediments," J. Acoust. Soc. Am. 47, 1440-1447 (1970).

39. J. Geertsma and D. C. Smith, "Some Aspects of Elastic Wave Propagation in Fluid Saturated Porous Solids," *Geophys.* 26, 169-181 (1961).
40. C. Zwikker and C. W. Kosten, Sound Absorbing Materials (Elsevier Publishing Company, New York, 1949).
41. R. W. Morse, "Acoustic Propagation in Granular Media," *J. Acoust. Soc. Am.* 24, 696-700 (1952).
42. J. M. Hovem, "The Nonlinearity Parameter of Saturated Marine Sediments," submitted for publication to *The Journal of The Acoustical Society of America*.

APPENDIX A
BIBLIOGRAPHY
ONR CODE 480 PROGRAM DOCUMENTATION

Applied Research Laboratories, The University of Texas at Austin, "Status Report No. 1 under Texas A&M Research Foundation P. O. No. RF-11743 and ONR Contract N00014-70-A-0166-0005," 1 January -1 July 1971 (7 July 1971).

Applied Research Laboratories, The University of Texas at Austin, "Final Report under Contract N00014-70-A-0166-0005," Applied Research Laboratories Technical Report No. 72-6 (ARL-TR-72-6), Applied Research Laboratories, The University of Texas at Austin, 17 January 1972.

Anderson, A. L., and L. D. Hampton, "In Situ Measurement of Sediment Acoustic Properties During Coring," paper presented at the ONR Symposium on Physical and Engineering Properties of Deep-Sea Sediments, Airlie House, Airlie, Virginia, 24-27 April 1973.

Anderson, A. L., and L. D. Hampton, "Measurement of In Situ Acoustic Properties During Sediment Coring," paper presented at the ONR Symposium on the Physics of Sound in Marine Sediments, Lakeway Inn, Austin, Texas, 8-10 May 1973.

Anderson, A. L., "Acoustics of Gas-Bearing Sediments," Applied Research Laboratories Technical Report No. 74-19 (ARL-TR-74-19), Applied Research Laboratories, The University of Texas at Austin, May 1974.

Anderson, A. L., and L. D. Hampton, "A Method for Measuring In Situ Acoustic Properties During Sediment Coring," in Physics of Sound in Marine Sediments, edited by Loyd D. Hampton (Plenum Press, New York, 1974).

Anderson, A. L., and L. D. Hampton, "In Situ Measurements of Sediment Acoustic Properties During Coring," in Deep-Sea Sediments, Physical and Mechanical Properties, edited by A. L. Inderbitzen (Plenum Press, New York, 1974).

Anderson, A. L., and L. D. Hampton, "Use of Tubes for Measurement of Acoustical Properties of Materials," paper presented at the 89th Meeting of The Acoustical Society of America, Austin, Texas, 7-11 April 1975.

Hampton, L. D., "ARL Experience with Acoustics and Gas in Sediments," paper presented at Symposium on Natural Gases in Marine Sediments and Their Mode of Distribution, The University of California Lake Arrowhead Conference Center, Lake Arrowhead, California, 28-30 November 1972.

Hampton, L. D., and A. L. Anderson, "Acoustics and Gas in Sediments: Applied Research Laboratories (ARL) Experience," in Natural Gases in Marine Sediments, Marine Science Vol. III, edited by Isaac R. Kaplan (Plenum Press, New York, 1974).

- Shirley, D. J., and L. D. Hampton, "Acoustic Velocity Profilometer for Sediment Cores," Ocean '72, Record of the International Conference on Engineering in the Ocean Environment, Newport, Rhode Island, 13-15 September 1972.
- Shirley, D. J., and L. D. Hampton, "Determination of Sound Speed in Cored Sediments," Applied Research Laboratories Technical Report No. 72-44 (ARL-TR-72-44), Applied Research Laboratories, The University of Texas at Austin, 20 December 1972.
- Shirley, D. J., A. L. Anderson, and L. D. Hampton, "In Situ Measurement of Sediment Sound Speed During Coring," Applied Research Laboratories Technical Report No. 73-1 (ARL-TR-73-1), Applied Research Laboratories, The University of Texas at Austin, 14 March 1973.
- Shirley, D. J., A. L. Anderson, and L. D. Hampton, "Measurement of In Situ Sound Speed During Sediment Coring," Ocean '73, Record of the International Conference on Engineering in the Ocean Environment, Seattle, Washington, 25-28 September 1973.
- Shirley, D. J., and L. D. Hampton, "Acoustic Velocimeter for Ocean Bottom Coring Apparatus," Applied Research Laboratories Invention Disclosure, 9 November 1973.
- Shirley, D. J., "Interim Technical Description of the ARL Compressional Wave In Situ Profilometer," Applied Research Laboratories Technical Memorandum No. 74-9 (ARL-TM-74-9), Applied Research Laboratories, The University of Texas at Austin, 21 March 1974.
- Shirley, D. J., "Calibration Manual for ARL Profilometer," Informal Memorandum, July 1974.
- Shirley, D. J., and A. L. Anderson, "Compressional Wave Profilometer for Deep Water Measurements," Applied Research Laboratories Technical Report No. 74-51 (ARL-TR-74-51), Applied Research Laboratories, The University of Texas at Austin, 6 December 1974.
- Shirley, D. J., and A. L. Anderson, "Studies of Sediment Shear Waves, Acoustical Impedance, and Engineering Properties," Applied Research Laboratories Technical Report No. 75-23 (ARL-TR-75-23), Applied Research Laboratories, The University of Texas at Austin, 7 May 1975.
- Shirley, D. J., "Fine Structure of the Sound Speed Profile in Ocean Bottom Sediments," paper presented at the 89th Meeting of The Acoustical Society of America, Austin, Texas, 7-11 April 1975.
- Shirley, D. J., "Transducer for Generation and Detection of Shear Waves," Applied Research Laboratories Invention Disclosure, 18 August 1975.

- Shirley, D. J., and A. L. Anderson, "Acoustical and Engineering Properties of Sediments," Applied Research Laboratories Technical Report No. 75-58 (ARL-TR-75-58), Applied Research Laboratories, The University of Texas at Austin, 29 October 1975.
- Shirley, D. J., and A. L. Anderson, "In Situ Measurement of Marine Sediment Acoustical Properties During Coring in Deep Water," IEEE Trans. on Geoscience Electronics GE-13, No. 4, October 1975.
- Shirley, D. J., and A. L. Anderson, "Experimental Investigation of Shear Waves in Laboratory Sediments," paper presented at the 90th Meeting of The Acoustical Society of America, San Francisco, California, 3-7 November 1975.
- Shirley, D. J., "Determination of The Acoustic Properties of Deep Ocean Sediments from In Situ Profiles," paper presented at the 92nd Meeting of The Acoustical Society of America, San Diego, California, 15-19 November 1976.
- Shirley, D. J., and A. L. Anderson, "Shear Waves in Unconsolidated Sediments," paper presented at the 92nd Meeting of The Acoustical Society of America, San Diego, California, 15-19 November 1976.
- Shirley, D. J., "Acoustic Impedance Measuring Device for Marine Sediments," paper presented at the 93rd Meeting of The Acoustical Society of America, University Park, Pennsylvania, 6-10 June 1977.
- Shirley, D. J., "Method for Measuring In Situ Acoustic Impedance of Marine Sediments," J. Acoust. Soc. Am. 62, 1028-1032 (1977).
- Shirley, D. J., and L. D. Hampton, "Shear Wave Measurements in Laboratory Sediments," J. Acoust. Soc. Am. 63, 607-613 (1978).
- Shirley, D. J., "Laboratory and In Situ Sediment Acoustics," Applied Research Laboratories Technical Report No. 77-46 (ARL-TR-77-46), Applied Research Laboratories, The University of Texas at Austin, 23 August 1977.
- Shirley, D. J., "An Improved Shear Wave Transducer," J. Acoust. Soc. Am. 62, 1643-1645 (1978).
- Shirley, D. J., and D. W. Bell, "Acoustics of In Situ and Laboratory Sediments," Applied Research Laboratories Technical Report No. 78-36, (ARL-TR-78-36), Applied Research Laboratories, The University of Texas at Austin, 14 August 1978.
- Tucholke, B. E., and D. J. Shirley, "Comparison of Laboratory and In Situ Compressional-Wave Velocity Measurements on Sediment Cores from the Western North Atlantic," J. Geophys. Res. 84, 687-695 (1979).

APPENDIX B
DESCRIPTION OF NEW DESIGN FOR RECORDER

PRECEDING PAGE BLANK

The new design for the tape recorder is illustrated in Fig. 34, which is an enlarged drawing of the recorder mechanism. The mechanism is designed around the Scotch DC100A digital data cartridge from 3M Company. The cartridge contains 45 m (150 ft) of 4 mm (5/32 in.) wide magnetic tape. It is designed for single point drive, either forward or reverse at up to 230 cm/sec (90 ips). This single point drive feature was the reason that this more expensive tape was selected over the Phillips cassette tape used in the previous profilometer design. The three primary requirements for the tape recorder in the profilometer system are ruggedness, low cost, and the ability to fit inside the 11.5 cm i.d. pressure case.

Previous profilometer designs had used a Sony model TC-40 cassette recorder modified for 4-track FM operation with good results; this recorder was of requisite size and had the advantage of low cost. However, it was not very rugged and could not easily be modified to operate at the higher tape speeds that the new design requires.

With the DC100A tape cartridge, all the tape handling mechanism is incorporated inside the cartridge. The only moving part on the external transport is the drive motor. Thus the transport could easily be constructed by ARL:UT at low cost. Not having the many pulleys and belts that cassette recorders have, the new transport is extremely rugged by comparison. Finally, the small size of the data cartridge (6 cm x 8 cm x 1 cm) allows a compact design that easily fits inside the pressure case and is readily shock isolated from the container.

The tape transport is 10.5 cm diam and 2.5 cm thick, exclusive of the motor, which is a 3.8 cm diam x 3.2 cm high permanent magnetic dc motor. A small rubber bushing is mounted on the motor shaft to provide compliant contact with the drive wheel in the cartridge. Tape speed and direction are controlled by the voltage applied to the motor.

The tape head is rigidly mounted to the bottom plate of the transport, as is the optical end-of-tape sensor. The latter consists of an LED

AD-A075 833

TEXAS UNIV AT AUSTIN APPLIED RESEARCH LABS
LABORATORY AND FIELD STUDIES OF SEDIMENT ACOUSTICS.(U)
JUN 79 D J SHIRLEY , D W BELL , J M HOVEN

F/G 20/1

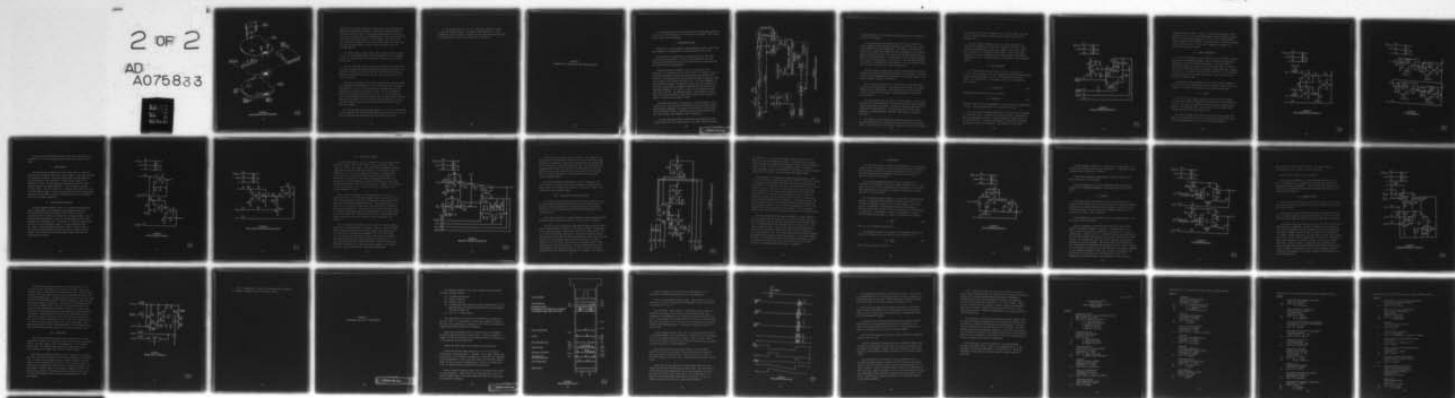
N00014-76-C-0117

UNCLASSIFIED ARL-TR-79-26

NL

2 OF 2

AD
A075833



END

DATE
FILMED

11-79

DDC

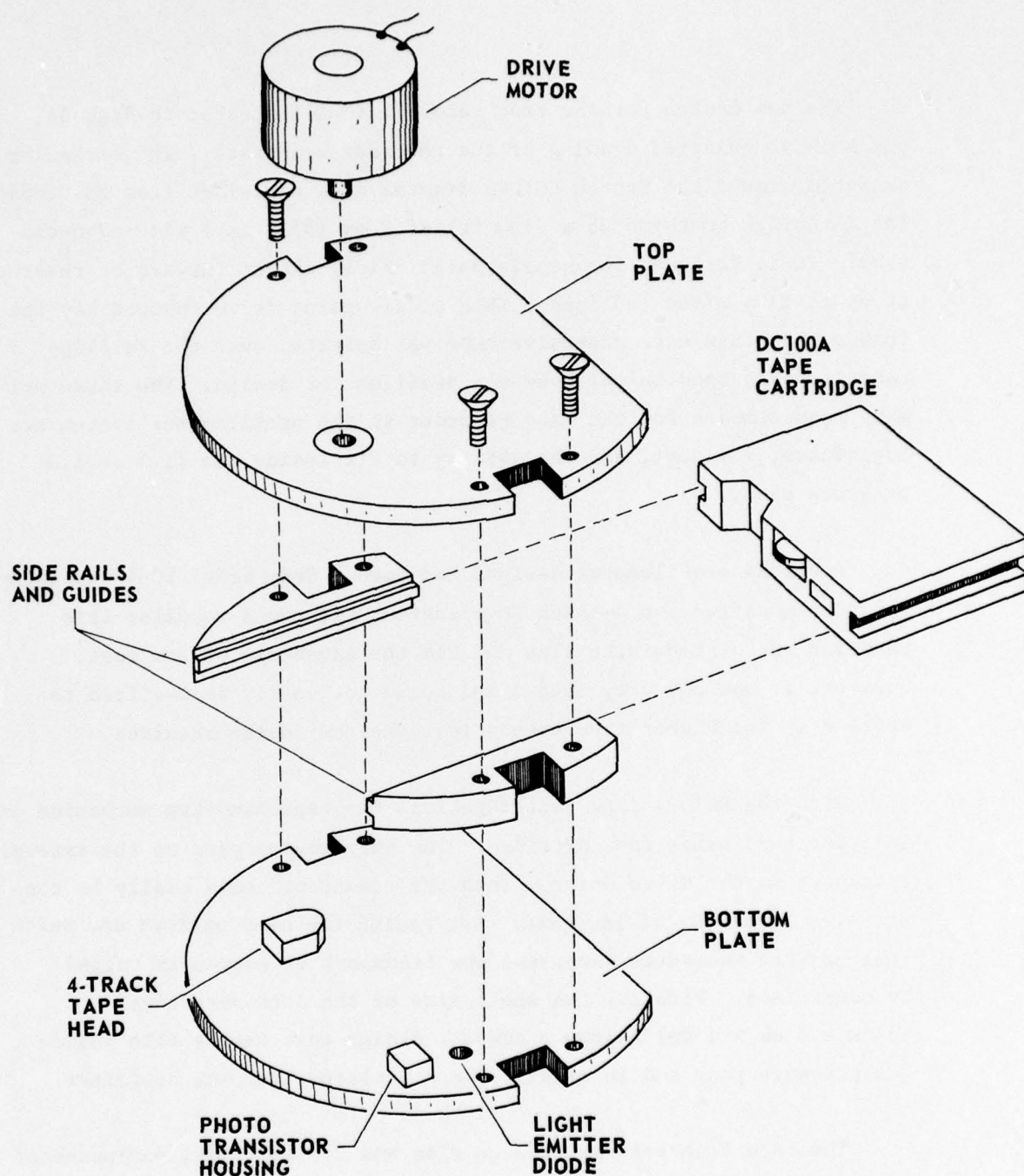


FIGURE 34
PROFILOMETER TAPE TRANSPORT

ARL:UT
AS-79-938
DJS - GA
5-11-79

lamp mounted vertically through the bottom plate and a phototransistor mounted horizontally near the LED. A small mirror mounted inside the cartridge directs the vertical light beam through the path of the tape and into the sensing area of the phototransistor. The dark tape does not allow light to reach the sensor. A clear leader at each end of the tape (provided by rubbing off the oxide from the tape) causes the light to reach the sensors which, in turn, drive electronic circuits to stop tape motion.

The square cutouts on each side of the transport provide clearance for the card cage mounting bars of the profilometer as well as passage of wires to the motor and to the waterproof connectors on the pressure case end cap.

The tape cartridge slides into the space between the top and bottom plate and is guided into proper position by the grooved side rails. The cartridge is held in contact with the tape head and drive motor by an elastic loop stretched across the back of the cartridge from one side rail to the other.

One result of changing to the new recording system using the DC100A tape cartridge is that only about 1 min of recording time is available. Approximately 4 to 5 sec of data recording are needed since the corer penetrates the bottom in this amount of time. The old profilometer system with the Phillips cassette recorder had 1 h of recording time with a C-120 cassette; thus, the procedure was to turn both the electronic power and the recorder on at the surface during deployment of the corer and then attempt to reach the ocean bottom with the corer before the tape was expended.

The procedure with the new system design is to turn the circuit power on at the surface with a water-sensing switch circuit so that the circuits will be stabilized and ready when the corer reaches the bottom.

At the bottom, where the corer is triggered, a switch is tripped to operate the tape recorder. An elapse of approximately 1 to 2 sec between the time the corer is triggered and the time it enters the bottom provides sufficient time for the recorder to reach speed.

APPENDIX C
EXPLANATION OF FUNCTION OF PROFILOMETER CIRCUITS

In the following, each circuit function will be explained separately in the order of its appearance in the system block diagram. Total system function will also be explained.

I. PROFILOMETER SYSTEM

Figure 35 is a block diagram of the profilometer system. Each block of the system is incorporated on a separate printed circuit card.

The purposes of the system are to measure and record the sound velocity in the sea bottom, to record the deceleration of the corer during bottom penetration, and to measure and record the insertion loss of the bottom on sound propagation.

The pulse generator supplies a 10 V, 1.5 μ sec pulse to the projector (at a repetition rate of about 750/sec) to generate a pulse of sound which propagates through the medium between the projector and receiver. The transducers are mounted pointing inward on opposite sides of the cutter at the bottom end of the corer. As bottom sediments are penetrated by the corer, the sediments flow between the transducers so that the sound propagates through the sediment and is detected by the receiving transducer. The signal is input to the preamplifier which has a gain of 40 dB. The amplified signal is then bandpass filtered with a low cutoff frequency of 120 kHz and a high cutoff frequency of 250 kHz. The filter has a gain of 20 dB.

The phase shifter has two functions: to shift the phase of the signal by 90°, and to provide variable gain for both the phase shifted and unshifted components. The gain for each output is set such that the two signals are equal in amplitude and just below clipping level with water between the transducers (zero attenuation).

The pulse amplitude detector measures the peak amplitude of the received signal at the 0° phase output of the phase shifter and inputs

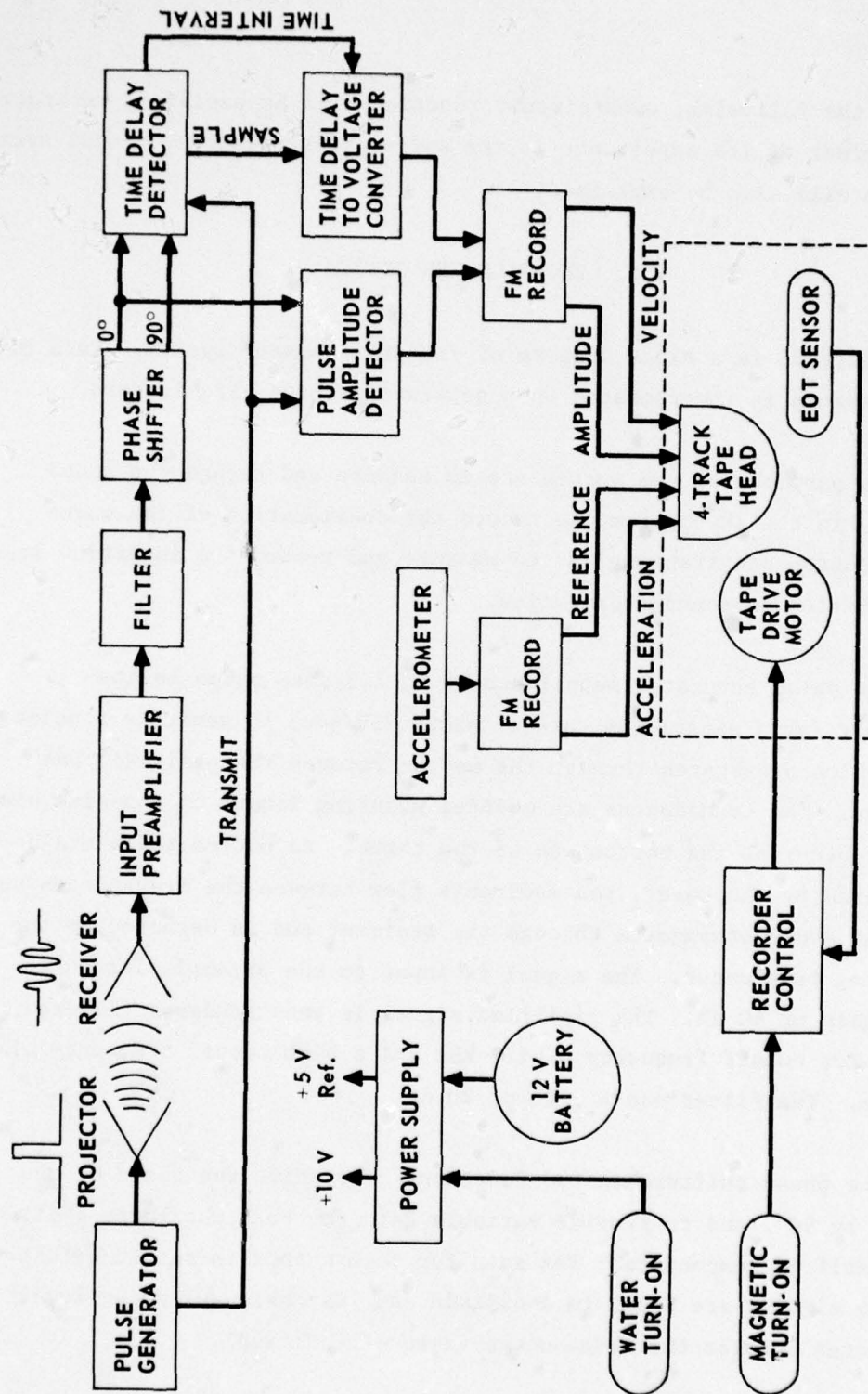


FIGURE 35
PROFILOMETER SYSTEM BLOCK DIAGRAM

ARL:UT
AS-79-950
DJS - GA
5-11-79

an analog voltage to the recording system proportional to the amplitude of the received signal.

The time delay detector measures the time interval between the pulse transmission and reception, dependent upon the velocity of sound in the medium between the transducers. The output of the time delay detector is a square pulse which starts at the beginning of the transmit pulse and ends at the first cycle peak of the received signal which is above a set threshold level. The threshold is used to avoid triggering on low level noise generated by the circuitry. The time delay detector also provides a sampling pulse, approximately 20 μ sec in duration, which starts at the end of the time interval output pulse.

The time interval output pulse is used by the time delay-to-voltage converter to generate an analog voltage which is proportional to the time interval between transmission and reception of the acoustic pulse. This analog voltage is input to the recorder.

The accelerometer consists of a piezoelectric acceleration sensor coupled to a charge amplifier. The output of this circuit is an analog voltage which is proportional to the acceleration experienced by the corer as it penetrates the bottom. The analog output is also input to the recorder.

There are two FM record circuits in the profilometer, each of which contains two recording channels. The FM record circuits take the slowly varying analog input and generate a frequency modulated signal which is applied to the recording head. One channel has no input but rather generates a constant frequency reference signal which is recorded on one track.

The recorder control contains the necessary circuitry to drive the tape drive motor and to start and stop the tape drive at the proper times. The tape drive is started when a magnetic reed switch is energized

at the instant the corer is triggered near the ocean bottom. The tape drive is turned off when an optical sensor detects the end of the magnetic tape.

The power supply contains circuits to control application of appropriate voltages to the rest of the electronic circuitry. There are two voltage regulators in the power supply: one for main power at 10 V, and one for 5 V reference at low current. Input to the power supply is 12 V from a rechargeable nickel-cadmium battery pack capable of supplying 1.8 Ah. The power supply is energized by a water activated switch.

II. PULSE GENERATOR

The pulse generator circuit, shown in Fig. 36, consists of a NE 555 IC timer configured as a free running astable multivibrator driving a power switching circuit. R1, R2, and C1 determine the on and off times of the multivibrator. The output at pin 3 of Q1 is high for a time t_1 , where

$$t_1 = 0.693(R1+R2)C2 \quad . \quad (40)$$

Then the output goes low for a time t_2 , where

$$t_2 = 0.693(R2)C1 \quad . \quad (41)$$

Thus the output is low for approximately 2 μ sec and high for approximately 1.3 msec. The pulse repetition rate is thus about 750 pps.

The output of Q1 is applied through R3 to the base of Q2 and through R6 to the base of Q5. Q5 inverts the pulse to provide a positive trigger to the measuring circuits; a negative trigger is supplied directly by the output of Q1. Q2 inverts the negative trigger pulse and drives the gate of Q3 which is a power FET. The output of Q3 drives the

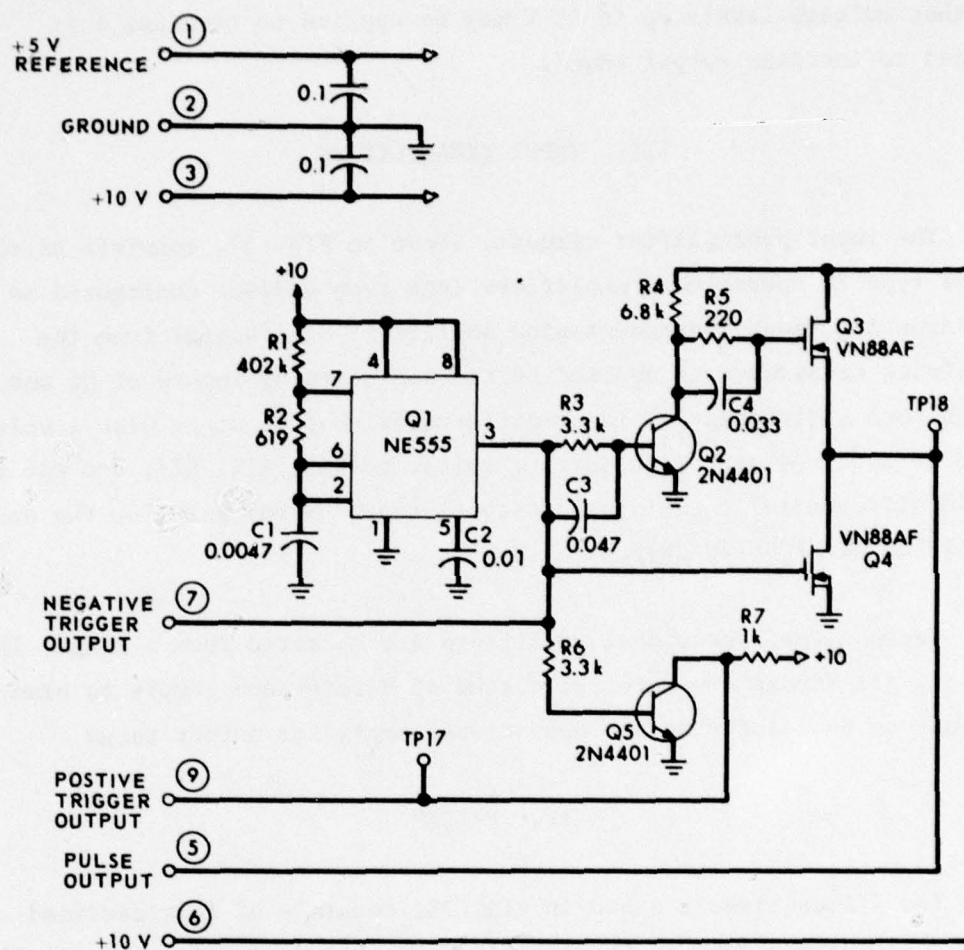


FIGURE 36
PULSE GENERATOR SCHEMATIC

ARL:UT
AS-79-951
DJS - GA
5-11-79

transducer through a cable. C3 and C4 decrease switching times in the driving circuit. Q4 is a power FET arranged so that its gate is driven 180° out of phase with the driver FET, Q3, so that its low impedance reduces ringing in the transducer. The output driver circuit is arranged so that voltage levels up to 40 V may be applied to terminal 6 if needed to increase output power.

III. INPUT PREAMPLIFIER

The input preamplifier circuit, shown in Fig. 37, consists of three BIFET type IC operational amplifiers (RCA type CA3140) configured as a differential input instrumentation amplifier. The signal from the receiving transducer is applied to the noninverting inputs of Q6 and Q7 which form a differential input-differential output stage with a voltage gain of X10. Q8 with gain setting resistors R13, R14, R15, and R16 form a X10 differential input/single output stage. Total gain for the preamplifier is X100 (40 dB).

Because the operational amplifiers are operated from a single 10 V supply, all inputs are referred to the +5 V reference supply to bias the outputs to the center of the operational amplifier output range.

IV. FILTER

The filter circuit shown in Fig. 38, consists of four cascaded 2-pole active sections to provide bandpass action with 4-pole rolloff at each end. The first two sections are 2-pole multiple feedback active filters in the high pass mode. The 3 dB point of each section is at 120 kHz and the gain of each section is X2.

The last two stages are 2-pole active low pass filters with 3 dB points at 280 kHz and gain of X2. The total gain of the filter is thus X16 in the passband and is down 6 dB at 120 kHz and 280 kHz.

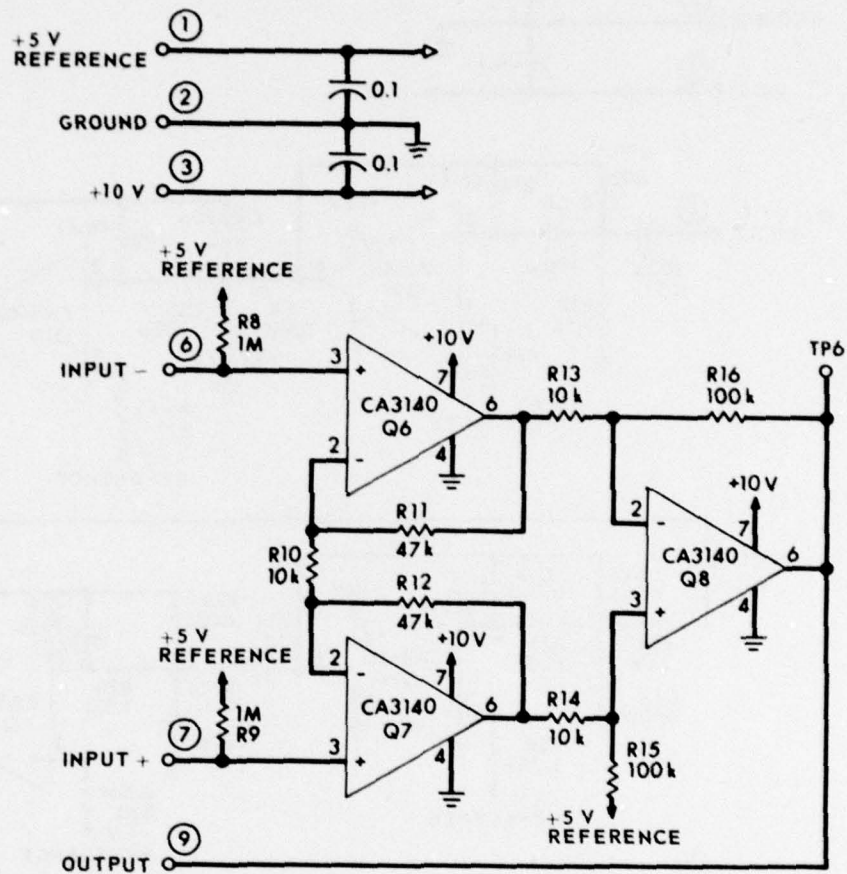


FIGURE 37
INPUT PREAMPLIFIER SCHEMATIC

ARL:UT
AS-79.952
DJS- GA
5-11-79

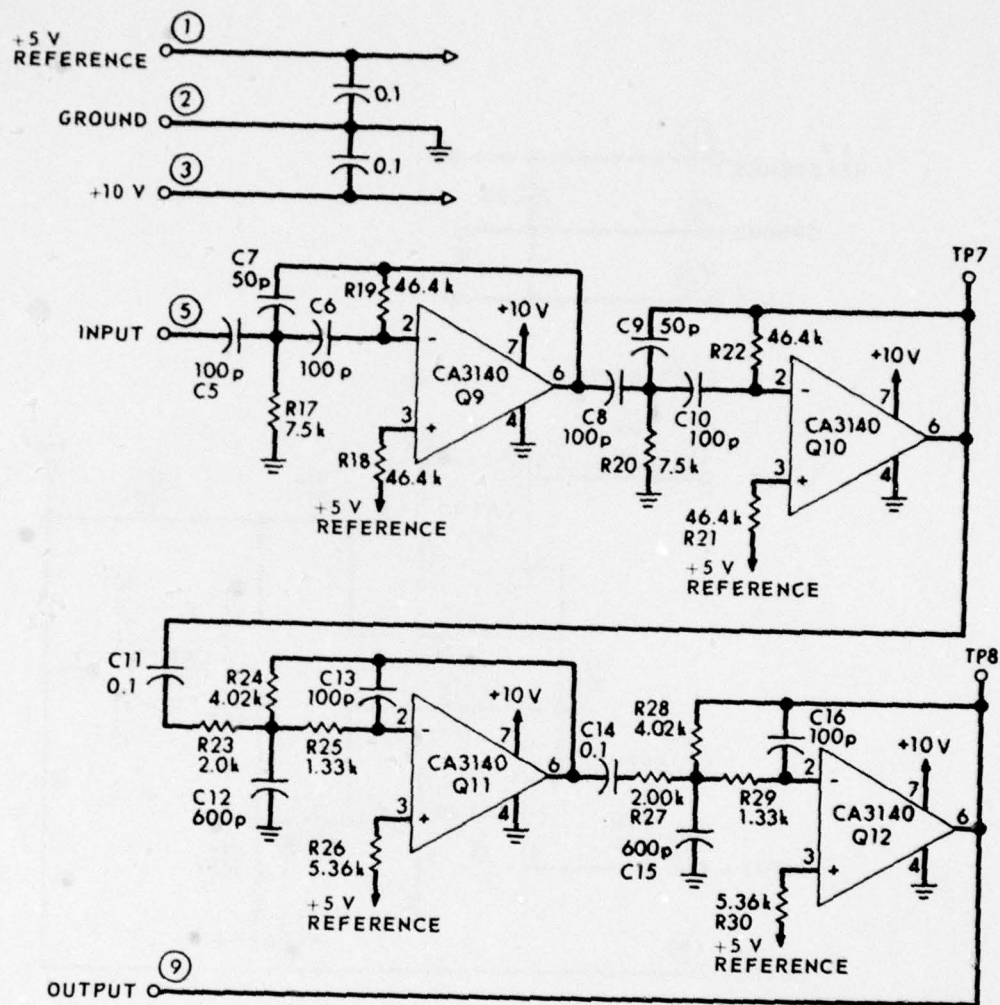


FIGURE 38
FILTER SCHEMATIC

ARL:UT
AS-79-953
DJS- GA
5-11-79

C11 and C14 are dc blocking capacitors that allow all inputs to be referred to +5 V to set the output of each stage in the center of its range.

V. PHASE SHIFTER

The function of the phase shift circuit (Fig. 39) is to take the filtered input signal and provide two output signals of the same amplitude but shifted 90° in phase. Q13, R31, and R32 form a variable gain non-inverting amplifier that provides a 0° phase shifted signal to the following circuits. Q14 and associated resistors and capacitor form a constant gain/variable phase amplifier. R33 is adjusted to provide 90° phase shift. Q15, R36, and R37 are a variable gain amplifier for the 90° phase shifted signal. R32 and R37 are adjusted so that the respective signals at TP9 and TP10 are equal in amplitude and just below clipping level with no signal attenuation.

VI. PULSE AMPLITUDE DETECTOR

The pulse amplitude detector (Fig. 40) provides an analog voltage output proportional to the amplitude of the received signal pulse. Q16 along with R38, R39, R40, and R41, and D1 forms a precision rectifier circuit to detect the envelope of the received pulse. R42, D2, and C18 form a peak detector circuit to hold the maximum level of the envelope of the received pulse. Q18 resets the circuit at each transmit pulse so that each measurement begins at the zero amplitude level. Q17 forms a $\times 1$ gain noninverting isolation stage to keep the load on the output from discharging C18 during the interval between received pulses. Q18 is driven by the positive going trigger pulse from the pulse generator circuit.

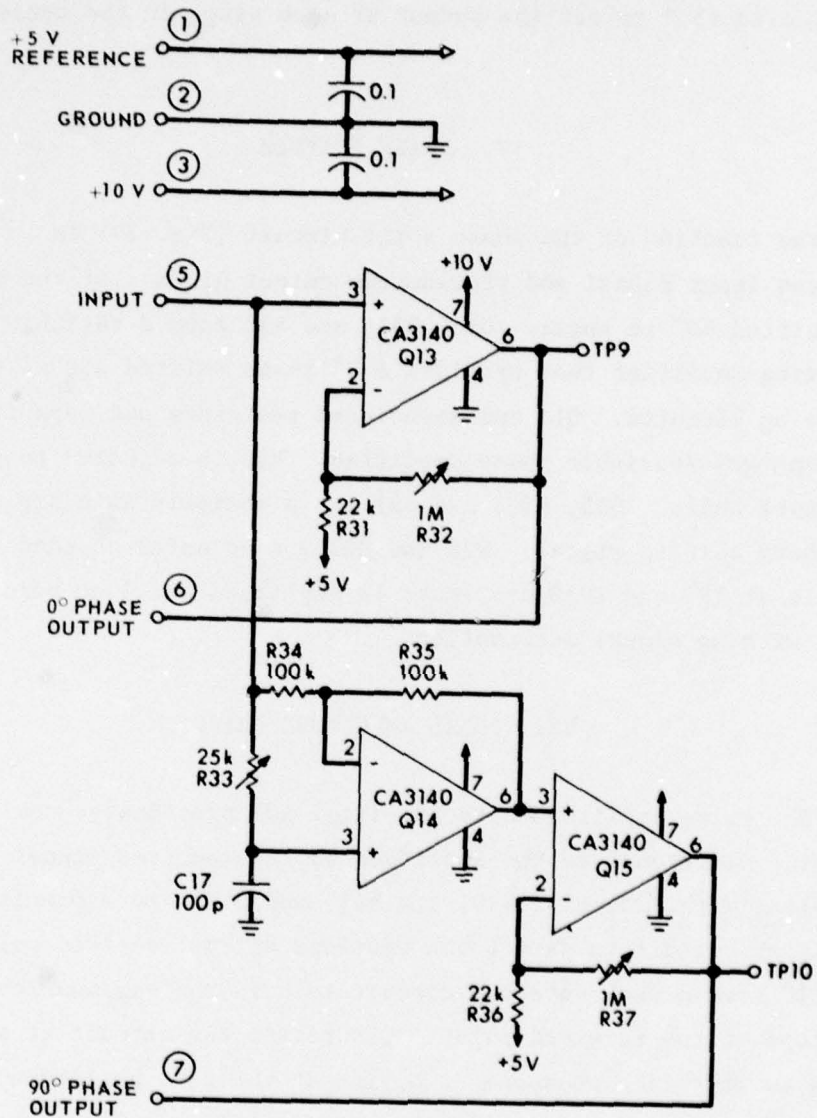


FIGURE 39
PHASE SHIFTER SCHEMATIC

ARL:UT
AS-79-954
DJS - GA
5-11-79

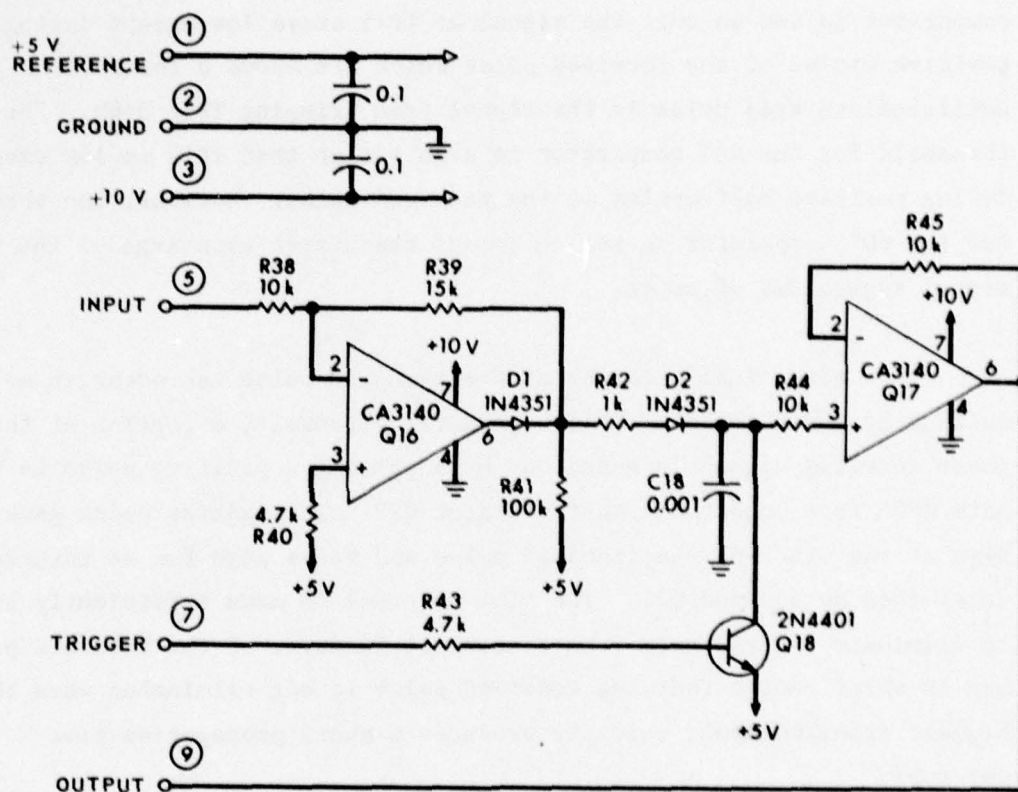


FIGURE 40
PULSE AMPLITUDE DETECTOR SCHEMATIC

ARL:UT
AS-79-955
DJS - GA
5-11-79

VII. TIME DELAY DETECTOR

The time delay detector (Fig. 41) operates to provide a square pulse which has a length equal to the transit time of the acoustic pulse across the sediment core sample. Q19A and Q19B form adjustable threshold comparators for the 0° and 90° phase signals. The threshold for the 0° comparator is set so that the signal at TP11 stays low except during positive cycles of the received pulse which are above a threshold sufficient to keep noise in the signal from bringing TP11 high. The threshold for the 90° comparator is also set so that TP12 is low except during positive half-cycles of the received pulse. However, the threshold for the 90° comparator is set to detect exact zero crossings of the signal regardless of noise.

Since electrical feedover of the transmit pulse can occur at a sufficient level to bring TP11 high during transmit, a portion of the 0° phase received signal is gated out by supplying a positive pulse to NOR gate Q20A from monostable multivibrator Q22. This gating pulse goes high at the start of the transmit pulse and stays high for an interval determined by R56 and C21. The time interval is made sufficiently long to eliminate interference from electrical feedover of the transmit pulse but is short enough that the received pulse is not eliminated when the highest expected sound velocity produces a short propagation time interval.

The two digital-level signals from the outputs of Q20A and Q20B are applied to the NAND gate Q21A. The output of Q21A is a burst of square pulses during the interval of the received pulse. The leading edge of the first pulse in the series corresponds to the peak of the first cycle of the received pulse which is larger than the noise threshold. This leading edge will thus maintain the same time relative to the received pulse regardless of pulse amplitude as long as the pulse has sufficient amplitude to rise above the noise threshold. The timing is critical to the accuracy of the sound velocity measurement.

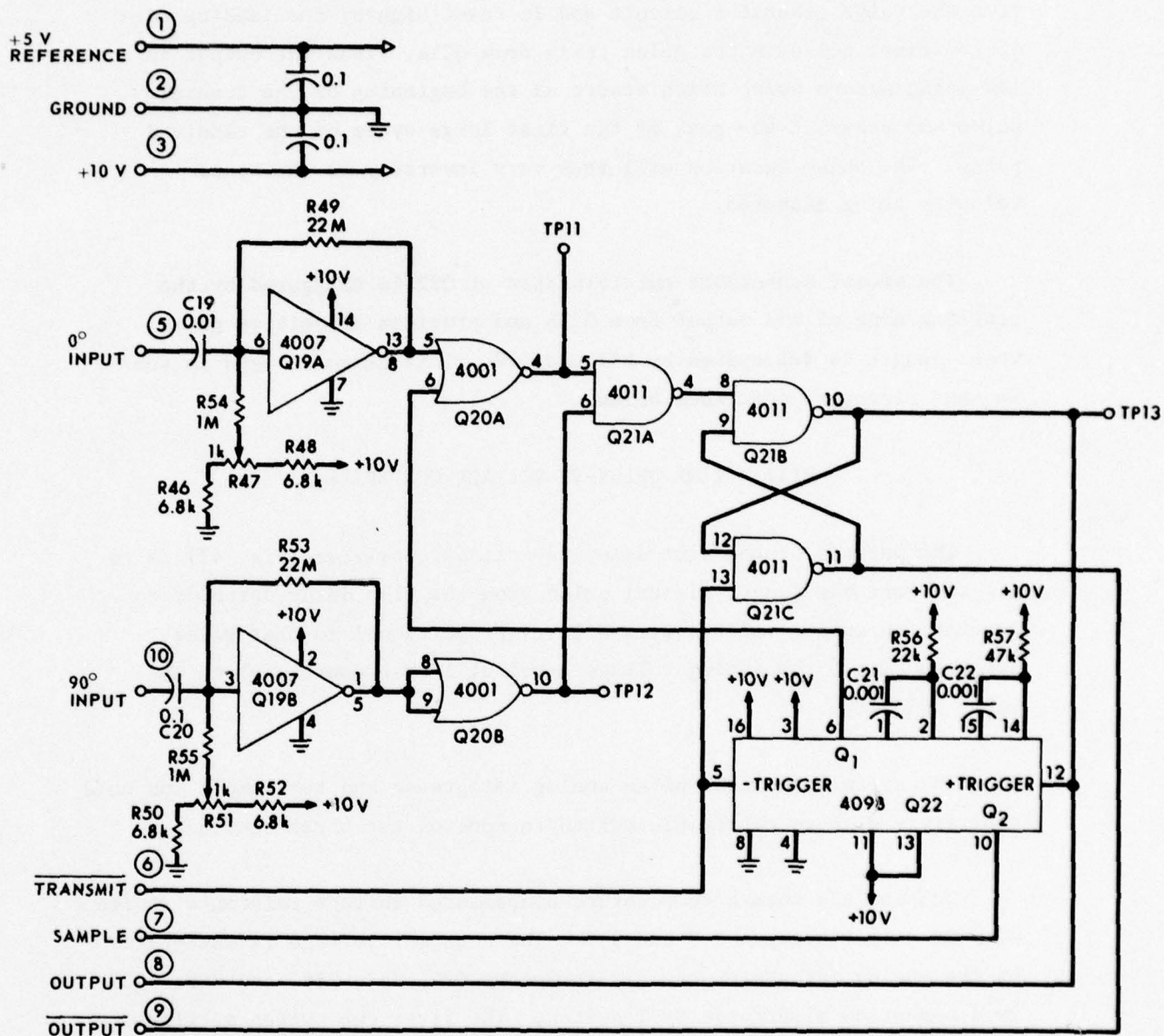


FIGURE 41
TIME DELAY DETECTOR SCHEMATIC

ARL:UT
AS-79-956
DJS - GA
5-11-79

Q21B and Q21C are wired as an R-S flip-flop. The output of the flip-flop, pin 10 (available at TP13), is set low by the trigger pulse from the pulse generator circuit and is reset high by the leading edge of the first pulse in the pulse train from Q21A. Thus the output is a low going square pulse which starts at the beginning of the transmit pulse and stops at the peak of the first large cycle of the received pulse. The pulse duration will thus vary inversely to the sound velocity being measured.

The second monostable multivibrator of Q22 is triggered by the trailing edge of the output from Q21B and provides a positive pulse whose length is determined by R57 and C22. This pulse is used in subsequent circuitry described below.

VIII. TIME DELAY-TO-VOLTAGE CONVERTER

The purpose of the time delay-to-voltage converter (Fig. 42) is to use the variable length digital pulse from the time delay detector to generate an analog voltage with a level proportional to that pulse duration (i.e., the analog voltage level will be proportional to the sound velocity).

The circuit consists of an analog integrator and two sample and hold amplifiers with an electronic switch to control the three sections.

Q23 and R56 form a temperature compensated voltage reference source with an output between 8 V and 9 V. The constant voltage is integrated by the analog integrator circuit formed by Q24, R57, R58, and C23. Q27 is a 4-section electronic SPST switch. The first two switch sections are connected in parallel (to reduce ON resistance) across C23 so that the capacitor is shorted except when the control signal to that switch section is at a low level. The control is the variable length output pulse from the time delay detector. As the control pulse goes low at the beginning of the transmit pulse, the switch across the integrator capacitor is opened allowing the integrator to function. The output of

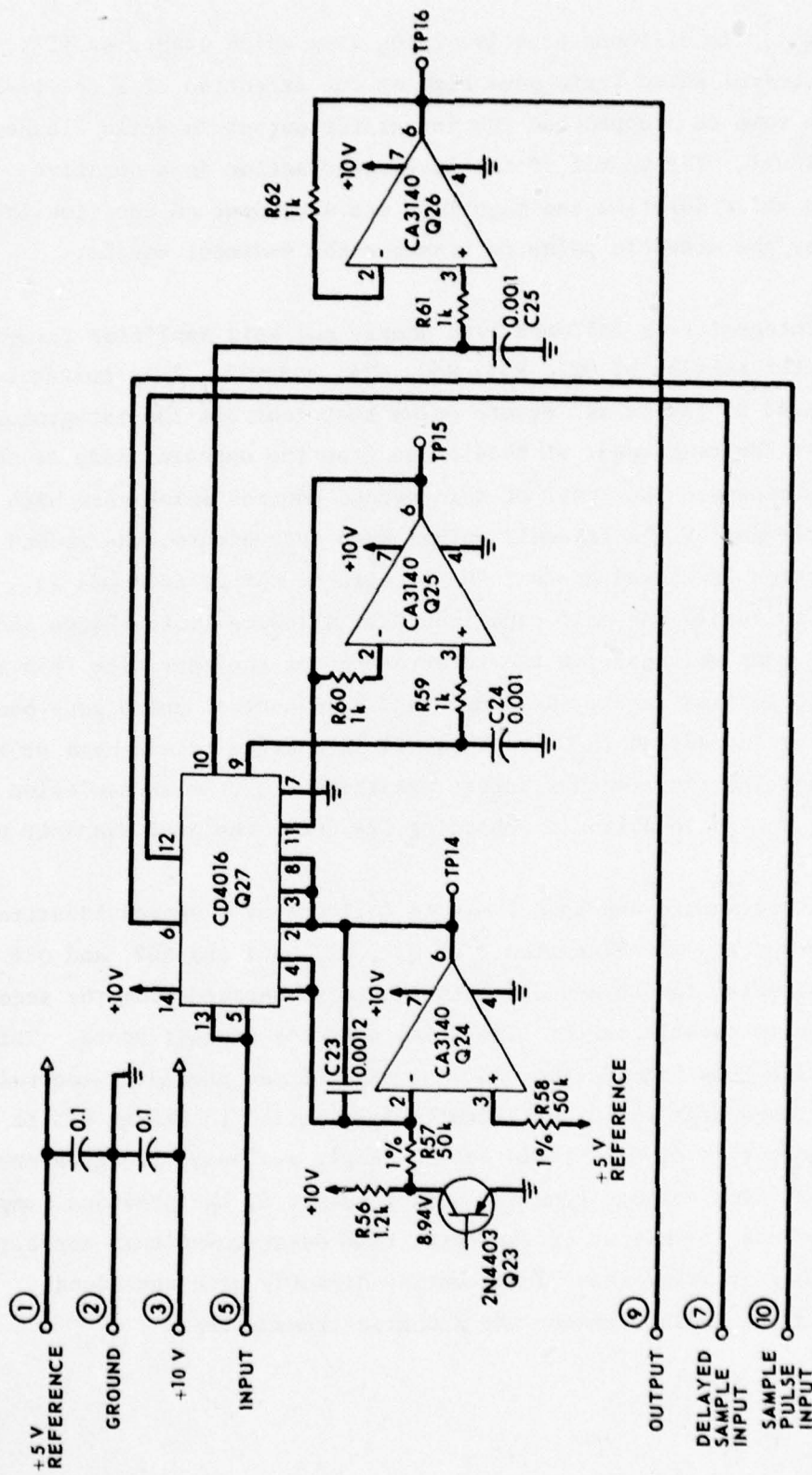


FIGURE 42
TIME DELAY-TO-VOLTAGE CONVERTER SCHEMATIC

ARL:UT
AS-79-957
DJS - GA
5-11-79

the integrator is a linear negative-going ramp which starts at +5 V. When the control pulse again goes high at the detection of a received pulse, the ramp is stopped and the integrator output is again clamped to the +5 V level. The result of the integrator action is a negative going ramp whose duration and magnitude are dependent on the time interval required by the acoustic pulse to traverse the sediment sample.

The integrator is followed by a sample and hold amplifier formed by one switch section of Q27, R59, R60, C24, and Q25. This switch section is controlled by the "same" square pulse that controls the integrator except that the complement of this pulse from the opposite side of the R-S flip-flop is used. The level of this second control pulse goes high at the beginning of the transmit pulse; when this occurs, the second switch section is closed so that the integrator output from Q24 is connected to sample and hold capacitor C24, allowing it to charge and follow the ramp voltage from the integrator. At the same time that the ramp is stopped and reset, the sample and hold control pulse goes back low, opening the switch to C24. Thus C24 is charged to and held at the voltage that the ramp reaches before resetting. Q25 is an isolation stage to keep the load from discharging C24 until the next transmit pulse.

The first sample and hold stage is followed by a second identical section formed by switch section 4 of Q27, C25, R61 and R62, and Q26. The control pulse for this section is the pulse derived from the second half of the monostable on the time delay detector circuit board. This control pulse goes high on the trailing edge of the preceding control pulse and stays high for a sufficiently long period to charge C25 to the voltage output of Q25. This second sample and hold operation removes the terminal ramp voltage from the analog output of the previous sample and hold. Thus the output of the total time delay-to-voltage converter is a smooth dc voltage whose level varies directly with the sound velocity in the medium between the acoustic transducers.

IX. ACCELEROMETER

The third data channel recorded by the profilometer is a deceleration profile of the corer system. The deceleration profile can be integrated during playback to provide a depth-of-penetration history of the core. Thus the sound velocity and amplitude profiles can be plotted as a function of depth in the bottom.

The acceleration measuring circuits (Fig. 43) consist of a piezoelectric accelerometer coupled to a charge amplifier circuit. The output of the circuit is an analog voltage proportional to the acceleration experienced by the sensor on a single axis parallel to the long dimension of the profilometer.

The acceleration sensor consists of a piezoelectric bender element mounted in a cantilever beam arrangement inside a small metal case; the case is filled with silicone oil to provide damping. The accelerometer is connected to a charge amplifier circuit consisting of Q27, R63, R64 and R65, and C26. The circuit provides an output voltage E_o proportional to the change in charge Δq experienced by the piezoelectric benders in response to a change in acceleration as follows:

$$E_o = \frac{-\Delta q}{C_f} \quad , \quad (42)$$

where C_f is the feedback capacitor C26.

Low frequency response is controlled by the feedback capacitor and resistor, C26 and R64, such that the low cutoff frequency f_o is

$$2\pi f_o = \frac{1}{C_f R_f} \quad , \quad (43)$$

and in this case f_o is 8×10^{-3} Hz.

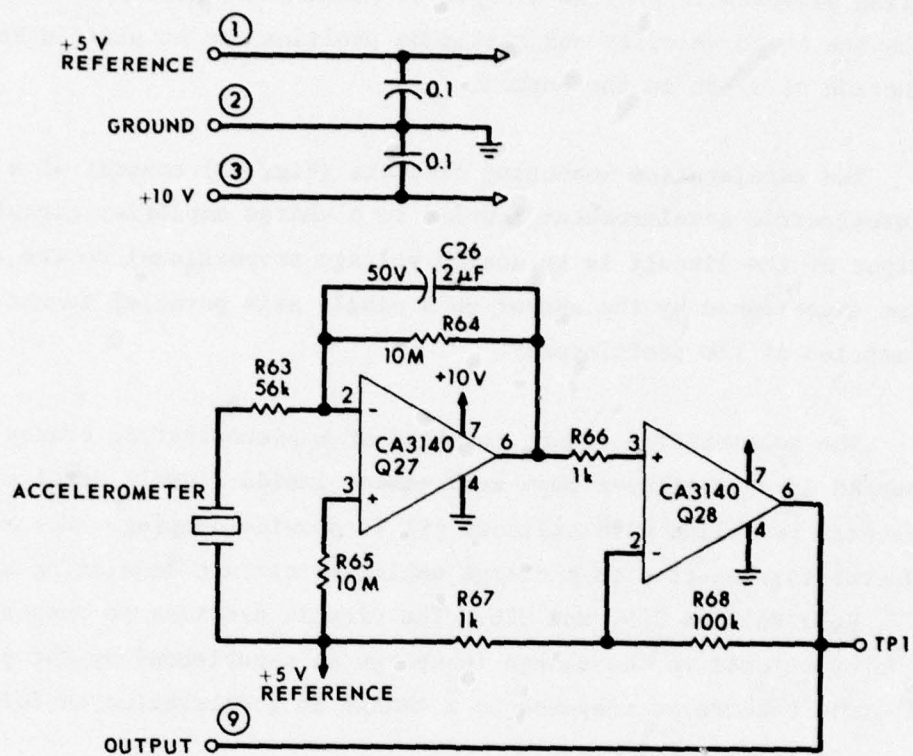


FIGURE 43
ACCELEROMETER SCHEMATIC

ARL:UT
AS-79-958
DJS- GA
5-11-79

The high frequency response is controlled by the capacitance of the piezoelectric elements and the input resistor R63. In this case the high frequency limit has been set to 100 Hz.

R65 provides temperature compensation to minimize thermal drift due to input bias current changes.

The second stage of the circuit consisting of Q28 and associated resistors is a noninverting amplifier with 40 dB gain to boost signal level.

X. FM RECORD

The purpose of the two FM record circuit boards (Fig. 44) is to accept the three analog data inputs and provide three frequency modulated signals plus a constant frequency reference signal to drive the 4-track recorder tape head. All four circuits are identical except that the reference track has no input connection.

Each FM generator is constructed around a Datel Model VFQ-1C. Only one channel will be described.

Q30 with capacitors C27 and C28 and resistors R72, R73, and R74 comprise a voltage-to-frequency converter. A current input of 0 to 10/ μ A to pin 3 will generate a square wave of frequency 0 to 10 kHz and amplitude 10 V, output at pin 10. R69 and R70 sum the input data voltage and the offset voltage from constant voltage source Q29 so that the input current to the VFQ provides the proper center frequency and frequency deviation for each data channel. R69 and R70 must be selected for each data channel and each individual VFQ integrated circuit. Center frequency for all channels is usually set to 4.000 kHz with a deviation of ± 1.000 kHz for the expected deviations of data input voltages. For example, the sound velocity data voltage will vary between 0.00 V and 2.00 V depending upon the sound velocity being measured. So for the sound

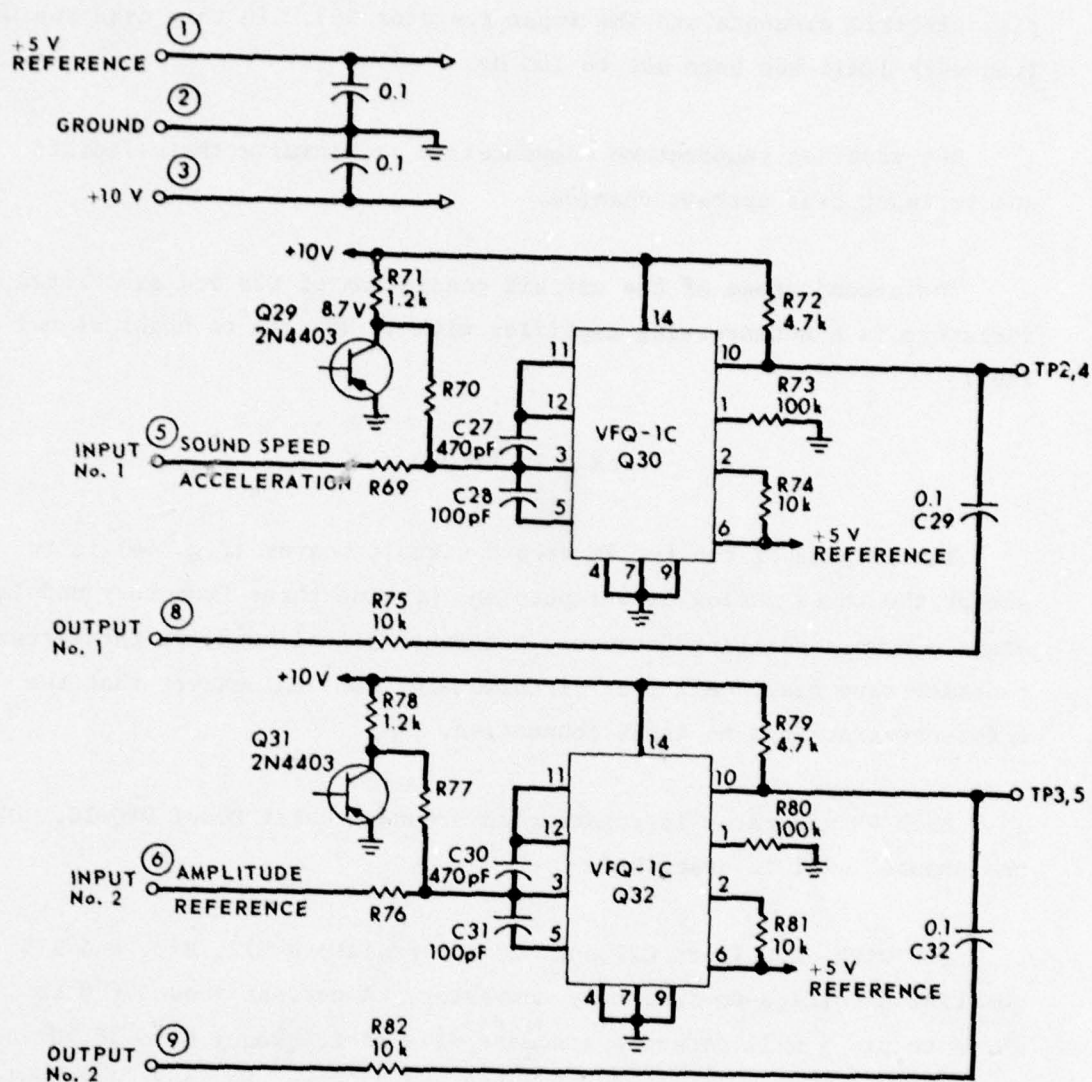


FIGURE 44
FM RECORD SCHEMATIC

ARL:UT
AS-79-959
DJS-GA
5-11-79

speed channel, 0.000 V input will result in an output frequency of 3.000 kHz and 2.00 V input will output 5.000 kHz.

The reference channel is set to 4.000 kHz.

The output from the VFQ is a square wave which goes from 0 V to 10 V. C29 removes the dc component from the square wave so that the tape head will not be magnetized. R75 provides current limiting to the record head to minimize self-erasure of the signal which would occur if the head were overdriven.

XI. RECORDER CONTROL

The function of the recorder control circuit (Fig. 45) is to start and stop the tape drive at the proper times and to keep the tape running at a constant speed.

Current drive to the recorder drive motor is provided by Q36 which forms a voltage regulator circuit with an output of 5 Vdc. R92 and R93 set the output voltage; C33 and C34 prevent oscillations in the circuit.

Q35 and R89, R90, and R91 form the circuit that turns the recorder on when the corer is triggered. The base of transistor Q35 is connected by a cable to a magnetic reed switch external to the profilometer case; this switch normally connects the base to ground due to the proximity of a magnet. Without base drive, the transistor is turned off, allowing pin 2 of Q36 to go to supply voltage level. With pin 2 at a high level, the voltage regulator is turned off and does not drive the recorder drive motor. When the corer is tripped near the ocean bottom, the magnet is pulled away from the reed switch (which opens and allows base drive from R89) to saturate Q34. Pin 2 of Q36 is brought to ground potential, thus turning on the voltage regulator and allowing the tape to be driven forward.

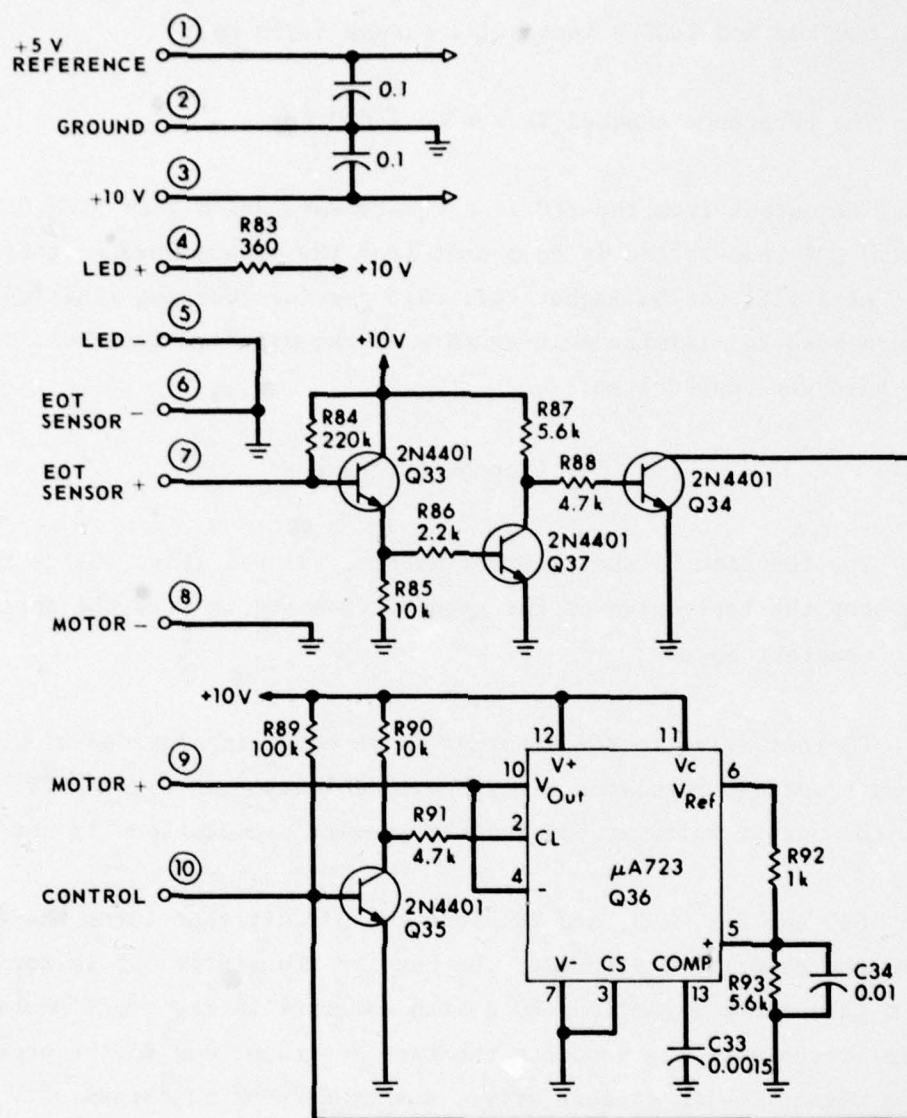


FIGURE 45
RECORDER CONTROL SCHEMATIC

ARL:UT
AS-79-960
DJS - GA
5-11-79

Q33, Q34, and Q37 with associated resistors form the circuit to turn off the tape drive when the end of tape is reached. On the tape transport there is positioned an LED light emitter and a phototransistor arranged so that the light from the LED shines through the magnetic tape onto the phototransistor. As long as there is tape on the reel, the light is blocked from the phototransistor which then exhibits a high impedance between its collector and emitter. The collector of the phototransistor is connected through a cable to the base of transistor Q33 with the emitter of the phototransistor connected to ground. As long as light is blocked from the phototransistor, the base of Q33 stays high as does its emitter. The base of Q37 is thus held high which turns on Q37 to produce a low level at the base of Q34. Q34 stays off, allowing the base of Q35 to remain high which, in turn, leaves the voltage regulator on. When a section of clear leader on the end of the magnetic tape appears between the LED and the phototransistor, all the voltage levels are reversed and the voltage regulator turns off, stopping the tape.

XII. POWER SUPPLY

The function of the power supply circuit (Fig. 46) is to control application of power to the other electronic circuits in the profilometer. Input to the power supply is from a rechargeable 12 V nickel-cadmium battery pack. An external sensor outside the profilometer package senses immersion in seawater and turns on the power supply.

Q40 and Q41 with R99 and R100 form a +10 V regulated power supply. The gate of FET Q38 is connected to an electrode external to the pressure case. As long as the instrument is dry, the gate of Q38 is held high which, in turn, holds the base of Q39 low. Pin 2 of Q40 is thus at a high level, the regulator is turned off, and no power is applied to the profilometer circuits. When the instrument is immersed in water, the gate of Q38 is shorted to ground, reversing the voltage level at pin 2 of Q40 and thus turning on the regulator and supplying power to the profilometer.

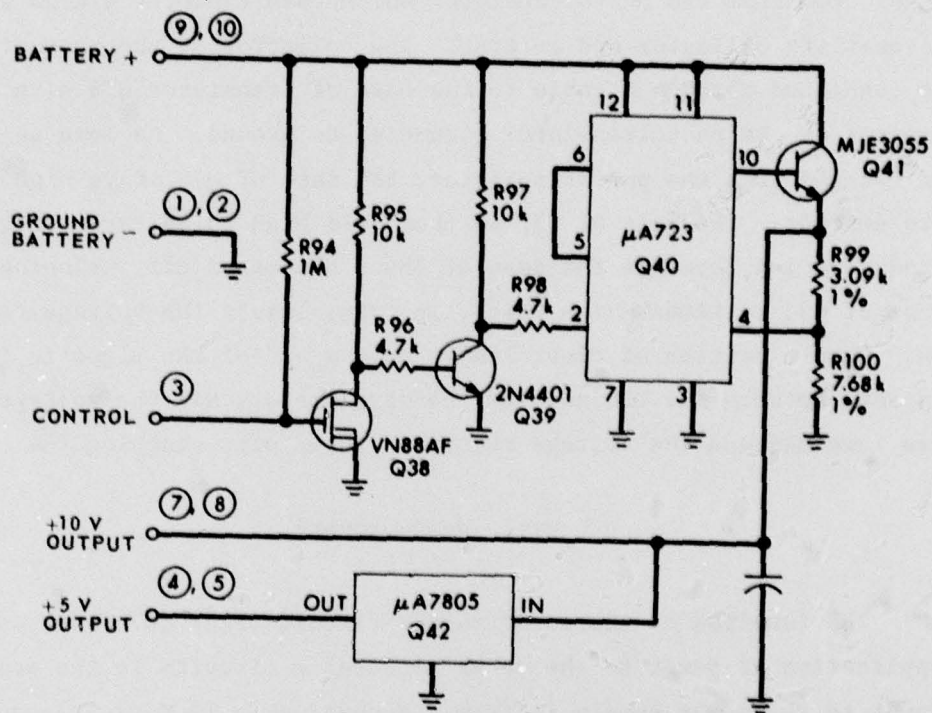


FIGURE 46
POWER SUPPLY SCHEMATIC

ARL:UT
AS-79-961
DJS- GA
5-11-79

Q42 is a monolithic 5 V regulator operating from the regulated +10 V supply to generate the +5 V reference supply.

APPENDIX D
CALIBRATION AND SETUP OF PROFILOMETER

PRECEDING PAGE BLANK

The equipment required to set up and calibrate the profilometer recording equipment include

- (1) 2-channel oscilloscope,
- (2) digital voltmeter,
- (3) frequency counter,
- (4) at least three test solutions of known sound velocity such as distilled water, 5% sodium chloride solution, and 10% sodium chloride solution, and
- (5) one 12 V, 1 A power supply.

The transducers to be used with the profilometer are mounted on the core cutter. It is desirable to leave the transducers attached to the cutter once calibration is completed so that there is no chance for changing the spacing between the transducers.

Remove the profilometer from its case and attach the transducer electrical plugs and the power control cable. Be sure the magnet is clamped in place on the magnetic reed switch and attach a shorting wire to the immersion turn-on electrodes.

Immerse the cutter head in a container of distilled water.

Connect the variable power supply set at 12 V to the correct battery pins on the profilometer. (CAUTION: If the power supply leads are reversed, it is possible to damage most of the electronic components in the profilometer.) Turn on the power supply and check that approximately 150 MA of current is being supplied. Allow the circuits about 15 min to stabilize before proceeding with calibration.

Figure 47 shows a schematic layout of the test points and controls on the profilometer. Connect TP17 on the pulse generator card to the external trigger input of the oscilloscope and adjust the oscilloscope for consistent triggering.

TAPE RECORDER

ACCELEROMETER

RECORDER CONTROL

FM RECORDER ACCELEROMETER, REFERENCE

FM RECORDER SOUND SPEED, AMPLITUDE

INPUT PREAMPLIFIER

FILTER

AMPLITUDE DETECTOR

PHASE SHIFTER

TIME DELAY DETECTOR

TIME DELAY TO
VOLTAGE CONVERTER

PULSE GENERATOR

POWER SUPPLY

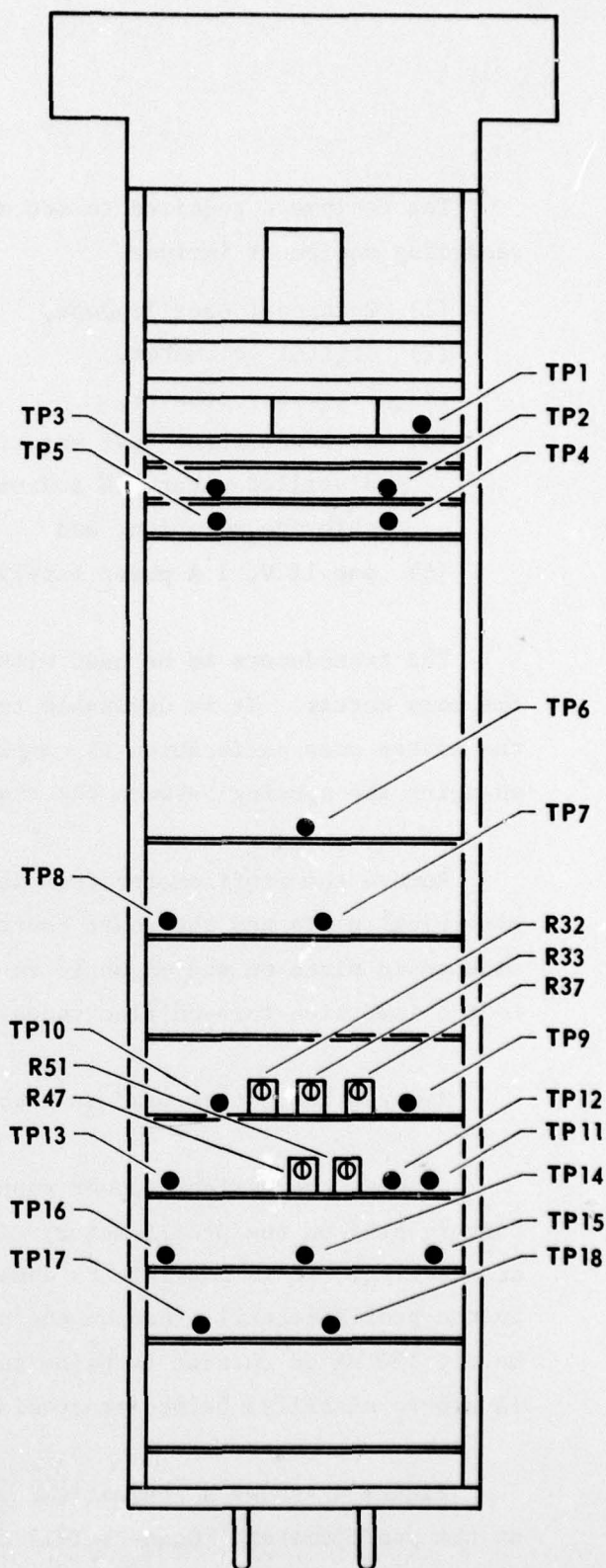


FIGURE 47
PROFILOMETER LAYOUT

ARL:UT
AS-79-962
DJS - GA
5-11-79

Figure 48 shows the time relation of various signals in the profilometer with their expected wave shapes and amplitudes.

Insert an oscilloscope probe into TP18. There should be a positive pulse about 1.5 μ sec in duration at the beginning of the trace and with an amplitude of 8 to 10 V.

Next check TP6. There should be a small pulse several cycles in length occurring about 50 to 100 μ sec after the start of the trace depending on the dimensions of the cutter and the sound velocity of the water. The amplitude of the pulse should be at least 0.2 V peak to peak. The same pulse should occur at TP7 and TP8 with progressively increasing amplitude and decreasing noise. Amplitude at TP8 should be about 4 V peak to peak.

For the adjustment of R32, R33, and R37, connect TP9 and TP10 each to a separate channel of the oscilloscope. Adjust R37 so that the signal at TP9 is just below clipping level (about 4 V peak to peak). Adjust R33 so that there is exactly 90° phase difference between the two signals, and then adjust R32, for equal amplitudes.

Next connect the two oscilloscope channels to TP11 and TP12. Adjust R47 so that the comparator output at TP11 does not trigger on noise preceding the received pulse. Then adjust R51 so the output at TP12 does trigger on low level noise (random pulses appear before receive pulse).

Check TP14 with one channel of the oscilloscope while the other channel monitors the received signal at TP8 or TP9. TP14 should show a linear negative-going ramp which starts at the beginning of the trace and stops at the first large cycle peak of the received pulse. The length of the ramp should be stable and not jittering. Any jitter indicates that R47 is not set at a high enough threshold.

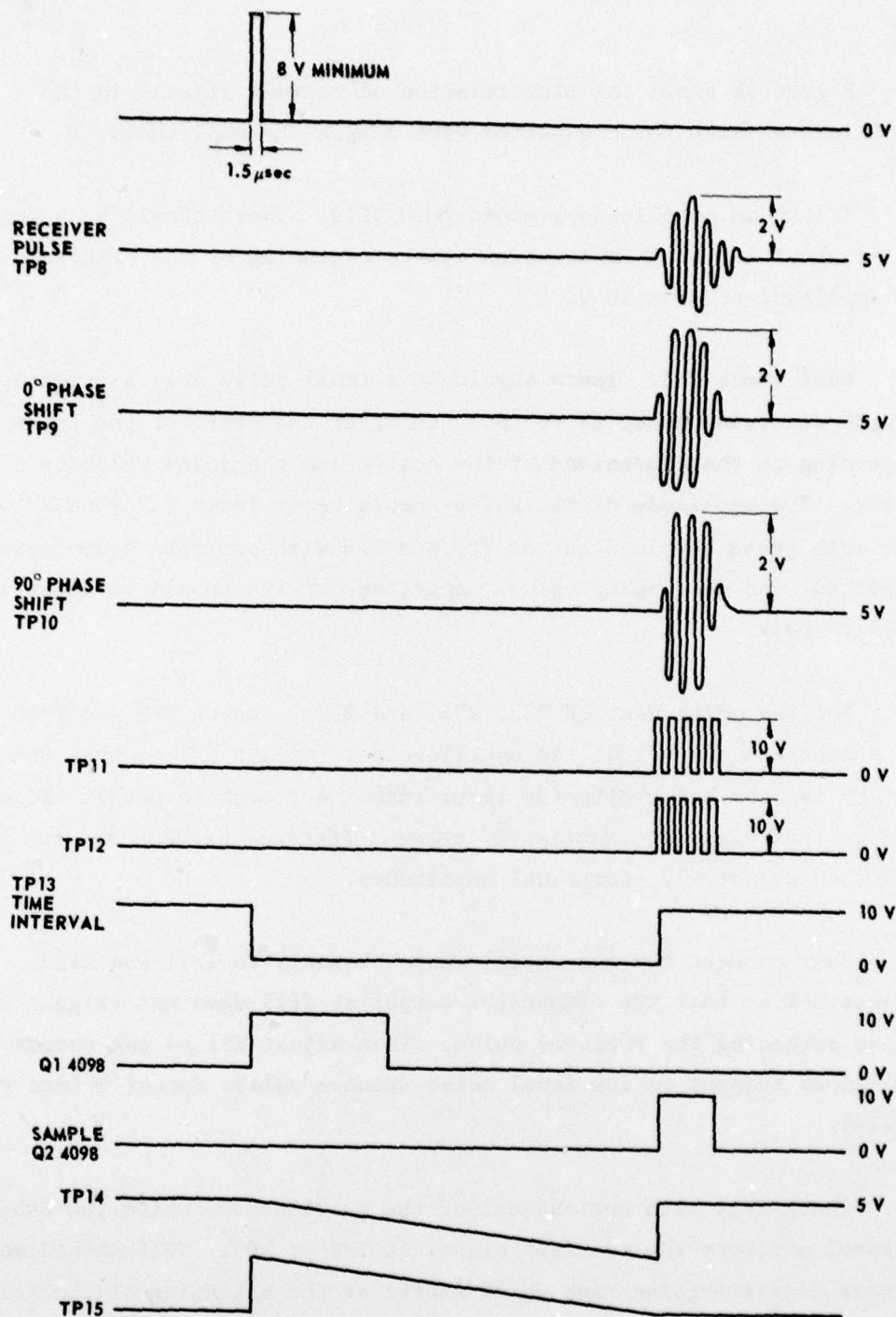


FIGURE 48
PROFILOMETER TIMING DIAGRAM

ARL:UT
AS-79-963
DJS - GA
5-11-79

TP15 should show a constant dc voltage with a ramp. There should be no appreciable drop in the constant voltage between the ending of one ramp and the start of the next. TP16 should show a constant dc voltage at the same level as the constant part of the signal at TP15.

Next, the accelerometer board should be attached to the extender cable to allow free movement of the accelerometer. The oscilloscope should be used to monitor TP1, which should show a voltage that varies as the accelerometer is moved.

Next monitor TP2 with the oscilloscope and the frequency counter. With the axis of the accelerometer vertical there should be a 10 V square wave with a frequency of about 4 kHz. As the accelerometer is moved, the frequency of the signal at TP2 should change.

TP3, TP4, and TP5 should show similar square waves with frequencies between 3 kHz and 5 kHz.

With the profilometer operating properly, calibration signals can be recorded at the beginning of a data tape. The three data channels are calibrated in succession. Insert a data tape cartridge in the recorder transport. Make certain the magnet is attached to the recorder turn-on switch.

The accelerometer is calibrated in the gravitational field of the earth and thus requires a stable platform not usually found aboard ship; for accuracy this must be done in the laboratory instead of in the field. However, a rough calibration should be made at the beginning of each data tape. Remove the magnet to turn on the tape recorder and orient the accelerometer both horizontally and vertically with respect to the earth. Record several changes in orientation. Turn off the recorder by replacing the magnet.

Next, calibrate the amplitude channel by observing the received pulse at TP9. Measure the peak to peak level of the pulse on the oscilloscope; this level was recorded during accelerometer calibration. Decrease the level with R37 and measure the peak to peak amplitude. Turn on the tape motor drive and record 3 to 4 sec of signal. Repeat for two or three such level changes. Finally, remove the preamplifier card from its socket to produce a zero level and record this. Turn off the tape recorder, replace the preamplifier card, and readjust R37 to initial conditions.

For calibration of the sound velocity data channels, prepare 5% and 10% saline solutions and measure their sound velocities as well as that of the water in which the transducers are already immersed. The sound velocity calibration for the distilled water was recorded on the tape during acceleration and amplitude calibration. Place the cutter head in the 5% saline solution and record several seconds with its sound velocity. Repeat for the 10% solution. Care should be taken that less than 30 sec of tape recording time is used for calibration.

The profilometer can now be readied for use by removing the transducer and control cables. Mount a fully charged battery on the instrument and place the instrument in the pressure case. Mount the instrument on the corer and attach all cables to their respective connectors.

12 June 1979

DISTRIBUTION LIST FOR
ARL-TR-79-26
UNDER CONTRACT N00014-76-C-0117
UNCLASSIFIED

Copy No.

Commanding Officer
Naval Ocean Research and Development Activity
NSTL Station, MS 39529
1 Attn: R. R. Goodman (Code 110)
2 R. D. Gaul (Code 600)
3 A. L. Anderson (Code 320)
4 S. Marshall (Code 340)
5 J. Paquin (Code 500)
6 J. Matthews (Code 362)

Commanding Officer
Office of Naval Research
Arlington, VA 22217
7 Attn: A. Sykes
8 T. Pyle (Code 48B)
9 H. Bezdek (Code 460)
10 M. Odegard (Code 48D)

Commanding Officer
Naval Electronic Systems Command
Department of the Navy
Washington, DC 20360
11 Attn: J. Sinsky (Code 320)
12 J. Reeves (Code PME 124-34)

Commander
Naval Sea Systems Command
Department of the Navy
Washington, DC 20362
13 Attn: A. P. Franceschetti

Chief of Naval Material
Department of the Navy
Washington, DC 20360
14 Attn: CAPT E. Young (Code 08724)

Commanding Officer
Naval Oceanographic Office
NSTL Station, MS 39529
15 Attn: W. Geddes

Distribution List for ARL-TR-76-26 under Contract N00014-76-C-0117

Copy No.

Commander
Naval Ocean Systems Center
Department of the Navy
San Diego, CA 92132
16 Attn: M. A. Pedersen (Code 307)
17 R. R. Gardner (Code 40)
18 E. L. Hamilton
19 H. P. Bucker (Code 409)

Director
Naval Research Laboratory
Department of the Navy
Washington, DC 20375
20 Attn: Code 2627
21 O. Diachok

Chief of Naval Operations
Department of the Navy
Washington, DC 20350
22 Attn: CNO R. S. Winokur (OP-95E1)

Commander
Naval Air Development Center
Department of the Navy
Warminster, PA 18974
23 Attn: C. L. Bartberger

Commander
New London Laboratory
Naval Underwater Systems Center
Department of the Navy
New London, CT 06320
24 Attn: P. Herstein

Commanding Officer
Naval Coastal Systems Center
Panama City, FL 32401
25 Attn: E. G. McLeroy, Jr.
26 B. Tolbert

Superintendent
Naval Postgraduate School
Monterey, CA 93940
27 Attn: H. Medwin
28 Library

Distribution List for ARL-TR-76-26 under Contract N00014-76-C-0117

Copy No.

	Woods Hole Oceanographic Institution
	Woods Hole, MA 02543
29	Attn: C. Hollister
30	Dr. B. Tucholke
	Hawaii Institute of Geophysics
	The University of Hawaii
	2525 Correa Road
	Honolulu, HI 96822
31	Attn: Dr. G. Sutton
32	Dr. M. Manghnani
	The Scripps Institution of Oceanography
	The University of California/San Diego
	San Diego, CA 92152
33	Attn: P. Lonsdale
	Department of Geological Oceanography
	Texas A&M University
	College Station, TX 77840
34	Attn: Dr. W. R. Bryant
	Underwater Systems, Inc.
	3121 Georgia Avenue
	Silver Spring, MD 20910
35	Attn: M. S. Weinstein
	Geophysics Laboratory
	Marine Science Institute
	The University of Texas
	700 The Strand
	Galveston, TX 77550
36	Attn: Dr. G. Latham
37	Dr. E. W. Beherns
	Tracor, Inc.
	1601 Research Boulevard
	Rockville, MD 20850
38	Attn: R. J. Urick
	The Catholic University of America
	6220 Michigan Avenue, NE
	Washington, DC 20017
39	Attn: H. M. Überall
	Lamont-Doherty Geological Observatory
	Palisades, NY 10964
40	Attn: G. Bryan
41	W. J. Ludwig
42	R. D. Stoll

Distribution List for ARL-TR-76-26 under Contract N00014-76-C-0117

Copy No.

	Department of Civil and Ocean Engineering The University of Rhode Island Kinston, RI 02881
43	Attn: Dr. A. J. Silva
	University College of North Wales Marine Science Laboratories Menai Bridge Anglesey, NORTH WALES
44	Attn: D. Taylor Smith
45	P. Schultheiss
	Director SACLANT ASW Research Centre La Spezia, ITALY
46	Attn: T. Akal
	The University of Auckland Auckland, NEW ZEALAND
47	Attn: A. Kibblewhite, Department of Physics
	Defence Research Establishment Pacific CF Dockyard Victoria, B. C., CANADA B2Y 3Z7
48	Attn: Library
	Defence Research Establishment Atlantic 9 Grove Street Dartmouth, N.S., CANADA
49	Attn: Library
	Department of Civil Engineering The University of Texas at Austin Austin, TX 78712
50	Attn: K. Stokoe
51 - 60	Commanding Officer and Director Defense Documentation Center Defense Services Administration Cameron Station, Building 5 5010 Duke Street Alexandria, VA 22314
	Conoco, Inc. Exploration Research Drawer 1267 Ponca City, OK 74601
61	Attn: Dr. D. Bell
62	Dr. G. Brown

Distribution List for ARL-TR-76-26 under Contract N00014-76-C-0117

Copy No.

63	Southwest Research Institute P. O. Drawer 28510 San Antonio, TX 78284 Attn: Dr. T. Owen
64	Electronics Research Laboratory The University of Trondheim The Norwegian Institute of Technology O. S. Bragstad Plass 6 N-7034 Trondheim - NTH, NORWAY Attn: Dr. J. Hovem
65	Office of Naval Research Resident Representative Room 582, Federal Building Austin, TX 78701
66	Environmental Sciences Division, ARL:UT
67	David T. Blackstock, ARL:UT
68	Harlan G. Frey, ARL:UT
69	Loyd D. Hampton, ARL:UT
70	Kenneth E. Hawker, ARL:UT
71	Thomas G. Muir, ARL:UT
72	Donald J. Shirley, ARL:UT
73	Reuben H. Wallace, ARL:UT
74	Library, ARL:UT
75 - 86	Reserve, ARL:UT